NTNU – Trondheim
Norwegian University of
Science and Technology

Advanced Micro Photoluminescence Spectroscopy of Single GaAs/AlGaAs Core-Shell Nanowires

Stian Gulla

Nanotechnology
Submission date: July 2013
Supervisor: Helge Weman, IET
Co-supervisor: Lyubomir Ahtapodov, IET

Norwegian University of Science and Technology
Department of Electronics and Telecommunications

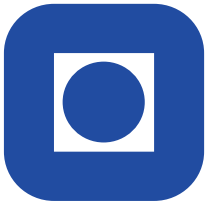

NTNU – Trondheim
Norwegian University of
Science and Technology

Master thesis

Advanced Micro Photoluminescence Spectroscopy of Single GaAs/AlGaAs Core-Shell Nanowires

Author:
Stian Gulla

Supervisor:
Prof. Helge Weman
Co-supervisor:
Ph.D. student Lyubomir
Ahtapodov

July 1, 2013

Declaration of independent work

I hereby declare that the work in this master thesis has been performed independently and in accordance with the regulations of the Norwegian University of Science and Technology (NTNU).

Stian Gulla

Abstract

Self-catalyzed (SC) growth is a relatively new approach to growing GaAs nanowires (NWs). It has several advantages to Au-catalyzed growth, such as integration on Si platforms. Many of the growth parameters, including growth rate and V/III ratio, and their influence on the growth process, are not fully understood. Three samples of SC GaAs/AlGaAs core-shell NWs were grown with different V/III ratios (17.4, 23.8 and 30.1), in order to study how this parameter influences the optoelectronic properties of the NWs. The molecular beam epitaxy vapor-liquid-solid approach was used to grow the samples. In this work they were investigated with excitation power-, temperature-, polarization- and time-resolved micro photoluminescence (μ-PL) spectroscopy.

Only the sample of highest V/III ratio, sample σ, exhibited free exciton emission coming from zinc blende (ZB) GaAs in the core of the NWs. The other two samples were dominated by type-II transitions, likely originating from the tip regions with interchanging ZB-wurtzite (WZ) layers. σ-NWs appear to have defects, however, as shown by its low emission intensity at room temperature. A reference sample, sample α, was also studied with the same methods. This sample, which was grown with a medium V/III ratio (20.0), but a lower growth rate, also showed signs of free exciton emission, possibly originating from WZ regions in the tip.

It is concluded that a higher V/III ratio is beneficial to optoelectronic applications, and that the number of defects are lowered, most likely due to fewer Ga antisites in the core. It is proposed that samples σ and α are studied by high-resolution transmission electron microscopy (HR-TEM) to further determine their structure. Also, new samples should be grown with higher V/III ratios, some of which should have a lower growth rate. Efforts to passivate the defect-rich tip from the core, such as axial AlGaAs inserts, are proposed.

Sammendrag

Selv-katalysert groing er en relativt ny måte å gro GaAs nanotråder. Metoden har flere fordeler i forhold til Au-katalysert groing, f.eks. kan nanotrådene integreres med Si-teknologi. Mange av vekst-parameterene, slik som vekst-hastighet og V/III forhold, og deres innflytelse på vekst-prosessen er ikke kartlagt. Tre prøver med selvkatalyserte GaAs/AlGaAs kjerne-skall nanotråder ble grodd med forskjellig V/III forhold (17.4, 23.8 og 30.1), for å bedre forstå hvordan denne parameteren påvirker de optiske egenskapene til nanotrådene. Prøvene ble grodd ved molecular beam epitaxy, vapor-liquid-solid metoden. For denne rapporten ble de karakterisert ved eksitasjonsintensitet-, temperatur-, polarisasjons- og tids-oppløst mikro-fotoluminisens spektroskopi.

Kun prøven med høyest V/III forhold, prøve σ, viste fri eksiton emisjon fra sinkblende GaAs i kjernen til nanotråden. De to andre prøvene viste type-II emisjon, som mest sannsynlig kom fra ende-segmentet med vekslende sinkblende-wurtsitt lag i krystallstrukturen. Emisjonsintensiteten til σ-nanotråder er lav ved romtemperatur, noe som indikerer defekter også i disse nanotrådene. En referanseprøve, prøve α, ble også karakterisert på samme måte. Prøven hadde V/III forhold på 20.0, men ble grodd med en lavere vekst-hastighet enn de andre prøvene. Den viste også tegn på fri eksiton emisjon, som kan ha oppstått i wurtsitt områder i endesegmentet.

Det konkluderes med at et høyere V/III forhold er ønsket for å oppnå gode optiske egenskaper, og at antall defekter blir lavere, mest sannsynlig på grunn av færre Ga antisites i kjernen. Det anbefales å utføre høy-oppløst transmisjons-elektronmikroskopi på prøve σ og α, for å undersøke strukturen i nanotrådene. Nye prøver bør bli grodd med høyere V/III forhold, og noen med lavere vekst-hastighet. Ende-segmentet bør passiveres bedre fra kjernen, noe som kan oppnås med aksielle AlGaAs segmenter.

Acknowledgments

This master thesis work has been conducted at the Norwegian University of Science of Technology (NTNU), with the Department of Electronics and Telecommunications (IET). It was a continuation of a project thesis from the autumn of 2012. The works were done in Prof. Helge Weman and Prof. Bjørn Ove Fimland's group at IET, a research group working with growth and characterization of GaAs nanowires for optoelectronic applications, such as solar cells. This work has been on optical characterization of nanowires in the group's nanophotonics laboratory.

First of all, I thank my supervisor Prof. Helge Weman for giving me the opportunity to work in his group and participate in the cutting edge work that they do. His experience and expertise proved a great help in understanding the results obtained, and guiding the work in the right direction. I would also like to thank him for showing understanding when I had to undergo surgical treatment in the last weeks of the thesis work.

I want to thank members of the group Dr. Dheeraj Dasa Lakshmi Narayana, PhD candidate Abdul Mazid Munshi and Prof. Fimland, who grew the nanowires studied in this thesis. A special thanks to Mazid Munshi, who helped me understand and describe the growth process section in this work.

And most importantly, I am very thankful to my co-supervisor, PhD candidate Lyubomir Aleksandrov Ahtapodov, for his continuous feedback and invaluable guidance throughout this past year. He has had the patience to lead me through the learning process and taught me what I needed to know when working in the nanophotonics lab. He has sacrificed both weekends and vacations, and without his help this work would not be possible.

Contents

List of Abbreviations

NW nanowire

VLS vapor-liquid-solid

MBE molecular beam expitaxy

WZ wurtzite

ZB zinc blende

SC self-catalyzed

PL photoluminescence

PRPL polarization-resolved photoluminescence

TRPL time-resolved photoluminescence

SEM scanning electron microscope

HR-TEM high resolution transmission electron microscope

CVD chemical vapor deposition

fcc face-centered cubic

hcp hexagonal close-packed

E_g bandgap energy

DOS density of states

IR infrared

PCSA polarizer-compensator-sample-analyzer

CCD charge coupled device

LP laser excitation power

FWHM full width at half maximum

List of Figures

List of Tables

1 Introduction

Semiconductors are deeply embedded in modern life. Semiconductors are indispensable for diodes, solar cells [1], transistors [2] and integrated circuits, to mention a few. Although new materials are emerging, silicon (Si) is the most commonly used semiconductor today [3] [4]. Si has some restrictions, however, perhaps most notably is its indirect bandgap, which makes it unsuitable as a light emitter in optoelectronic applications. III-V materials, many of which have direct bandgaps, are therefore used in many devices. Gallium arsenide (GaAs) is a widely used III-V compound, along with GaP, InAs, InP, AlAs and GaSb. Some important characteristics of GaAs are its direct bandgap and high electron mobility [5]. The material also has high resistivity in its undoped form [6], which enables tuning of conductance over a wide range, through doping. This makes GaAs an interesting material for many device applications, such as transistors [7], high-speed or high-frequency devices [7] [8], photo-voltaic cells [9], lasers [10] and solar cells [11] [12]. There are, however, several problems related to the integration of III-V semiconductors on Si, where lattice mismatch is perhaps the most notable [13].

Nano scale systems (sub $100nm$ [14]) have properties that differ from those in the bulk form. These novel properties are due to the small size of the systems, resulting in a larger relative surface area and quantum effects [15]. Nano scale systems are therefore expected to play a large role in future improvements in device performance. If growth is limited in all but one dimension (1D), structures known as nanowires (NW) are grown, which is an extensively researched topic [16]. Semiconductor NWs have promising outlooks for applications in transistors [17], photovoltaic cells [18] and lasers [19]. Despite the lattice mismatch, III-V NWs can be epitaxially grown on Si subtstrates because the effective strain relaxation at their free borders [20]. NWs, together with quantumm wells (2D structures), have many desired quantum effects, but NWs can accommodate lattice mismatch better than quantum wells [21]. Thus, the growth of III-V NWs enables integration of optoelectronic devices on Si [22].

The vapor-liquid-solid (VLS) approach [23] [24] is an established way of growing

GaAs NWs. Using a liquid metal particle, often gold (Au), is common for the VLS method. Depending on the method used, different crystal structures may arise in the NWs. Using molecular beam expitaxy (MBE) by the VLS approach [25] [26], with Au as a catalyst, was the first method to yield GaAs NWs with wurtzite (WZ) crystal phase [21] [27] [28]. Other methods, like Au-catalyzed metalorganic chemical vapor deposition (MOCVD) [29], can yield GaAs NWs with zinc blende (ZB) crystal phase. Access to both WZ and ZB GaAs NWs is of much interest, due to for example different optical properties [30]. Many growth parameters influence the crystal phase, including temperature, V/III ratio and growth rate [31] [32].

Using a Ga droplet as catalyst instead of Au is known as self-catalyzed (SC), or Ga-assisted growth, and was introduced by Fontcuberta et. al in 2008 [33] [34]. Whereas Au-catalyzed growth in general yields WZ crystal structure, SC GaAs NWs usually exhibit ZB crystal structure [35] [36]. A mixed structure is also possible [37]. Growing SC NWs is useful because bulk GaAs has ZB structure, making it better understood than WZ GaAs.

SC growth also removes the issue of using a foreign catalyst. A major disadvantage of using Au is that it diffuses easily in Si [38], and due to the nature of VLS growth the Au droplets are placed directly on the Si. Au particles are left as impurities in the Si, introducing midgap defects. This can lead to non-radiative recombination and alters carrier lifetimes, detrimental to optoelectronic applications [39] [40] [41]. The successful integration of defect-free GaAs NWs on the high performance, cost-effective Si platform, will enable new optical devices of large solar spectrum coverage and high carrier mobility.

The possibility of integrating GaAs NWs on Si-substrates drives much of the research into SC growth of GaAs NWs. Since the SC MBE VLS method is relatively new, however, many growth parameters and their influence on NW properties are not fully understood. In a previous project thesis on the same subject, the effect of growth rate on emission intensity was done [42]. Three samples grown under the same conditions, except for growth rate, were studied by power- and temperature dependent micro-photoluminescence (μ-PL). The most promising of the samples, named α, was also studied in this master thesis. More advanced characterization

techniques were used, such as polarization-resolved PL (PRPL) and time-resolved PL (TRPL).

In addition to α, three more samples were studied, named δ, ψ and σ. These samples were grown under similar growth parameters, but varying the V/III ratio. Power dependent-, temperature dependent-, polarization-resolved and time-resolved photoluminescence (PL) was performed on these samples. This was done to find information on the crystal structure and defect density of the samples, important characteristics affecting the optical quality. This data can be used to help optimize the V/III growth ratio for GaAs NWs for optoelectronic applications.

To ensure only single wire measurements, the NWs were studied beforehand by scanning electron microscopy (SEM). Further work might include high resolution transmission electron microscopy (HR-TEM) characterization on the same single NWs.

2 Theory

The theory presented here is meant to give a clear understanding of the results and discussion parts later in the report.

2.1 Growth of nanowires

The focus of this thesis is not on growth, however, here follows an introduction of the growth mechanisms used to create the gallium arsenide (GaAs) *nanowires* (NW) that were characterized.

2.1.1 Molecular beam epitaxy

Molecular beam epitaxy (MBE), is a method used to deposit single crystals with atomic resolution thickness, and is the technique known to yield the highest purity materials today [43]. The method requires a high to ultra-high vacuum of 10^{-10} to 10^{-11} torr or higher [4]. The instrument consists of three vacuum chambers, several heating cells and a reflection high-energy electron diffraction (RHEED) [44] observation device.

The three chambers are the load lock, the buffer chamber and the growth chamber. The sample is inserted in the load lock, which brings it in and out of the system. The buffer chamber is used for storing and preparation of the samples. The highest vacuum is in the growth chamber, which is where the sample is exposed to the atom beams.

The heating cells contain the substance that is to be grown, in its ultra-pure element form. The elements are heated until sublimation, most often through an electromagnetically focused electron beam source. A beam of atoms is let into the growth chamber, and hits the substrate. Due to the high vacuum, the mean free path of the atoms is long, so they will not undergo reaction before reaching the substrate. The slow growth allows the films and structures to grow epitaxially.

2.1.2 GaAs/AlGaAs nanowires

GaAs is a III-V semiconductor and has a promising outlook for future applications [45]. A high electron mobility enables use in high frequency devices in excess of 250 GHz [46], and a direct bandgap [30] [47] allows for optoelectronic applications, such as lasers [10] and solar cells [11] [12]. Being resistive in its undoped state, it provides natural isolation between circuits and devices when used as an electrical substrate [6] [48].

In this work we will study MBE grown SC NWs, with a GaAs core and an $Al_xGa_{1-x}As$ shell. A very thin GaAs cap is grown to cover the shell in order to prevent the formation of aluminum oxides. The AlGaAs bandgap is larger than that of GaAs (GaAs: $1.43eV$; AlAs: $2.16eV$ at $300K$ [49]), and this results in a confinement of the electrons and holes in the GaAs core (more on band theory in section 2.4). Thus, when performing photoluminescence, the observed emission will mostly be from the core. The GaAs core will consist of two polytypes, *zinc blende* (ZB) and *wurtzite* (WZ) crystal structure (more on crystal structure in section 2.2).

2.1.3 Au-catalyzed and self-catalyzed GaAs nanowires

The NWs being characterized in this work are grown by the *vapor-liquid-solid* (VLS) method [23] [24], a form of *chemical vapor deposition* (CVD). In traditional CVD a gas is slowly absorbed on a solid surface, while in VLS the gas is absorbed by a catalytic liquid alloy. The liquid becomes supersaturated by atoms from the gas, the atoms then nucleate at the VLS interface, which is where the growth occurs. By controlling the size of the liquid droplet, one can also control the size of the structure, i.e. the diameter of the NWs.

Growing GaAs NWs with gold (Au) as a catalyst is an established method [26]. NWs grown with Au as a catalyst, will commonly exhibit WZ crystal structure [21] [28]. Au-catalyzed growth can also yield NWs of ZB crystal structure when grown by metalorganic chemical vapor deposition (MOCVD) [29].

Fontcuberta et. al discovered in 2008 that by replacing the foreign metal droplet with gallium (Ga), self-catalyzed (SC), or Ga-assisted, NWs can be grown [33] [34].

This growth method is becoming even more popular than Au-catalyzed growth, and can be controlled to yield ZB as well as WZ GaAs NWs [35] [36] [37] [50]. Bulk GaAs is in the ZB phase, so the properties of ZB GaAs are well known, while there is still controversy around the properties of WZ GaAs [51]. One of the advantages of SC NW growth, is that the material properties of ZB GaAs are well understood, and there are indications that ZB GaAs NWs have similar properties. The NWs being characterized in this project are all SC (Sec. 3.1).

In addition to growing ZB GaAs, the SC growth mechanisms eliminates the problem of Au atoms diffusing into silicon (Si), the most common growth substrate used in semiconductor device applications. The Au atoms introduce detrimental midgap defects [39] [40] [41], making Au-catalyzed GaAs NWs unsuitable for integration on Si-devices. SC growth thus enables use of GaAs NWs on the Si platform.

The possibility of growing a perfect core-shell structure in the case of SC NW is an added advantage compared to the Au-catalyzed case. SC NW growth can be stopped by closing the Ga shutter and continue supplying the As flux in the MBE chamber, causing the process to consume the Ga droplet. The absence of the Ga droplet ensures only a radial growth during the subsequent $Al_xGa_{x-1}As$ shell growth. This results in a homogeneous near-perfect core-shell structure. There are problems related to this technique, however, possibly related to different crystal structures in the end segments grown during the Ga droplet consumption process, and future work is needed to solve this [50] [52]. On the other hand, one significant problem with Au-catalyzed growth is that the Au catalyst cannot be removed in-situ. Thus, when initiating radial growth of the AlGaAs shell, axial VLS growth catalyzed by the Au droplet will also occur, causing an AlGaAs end segment. Combined with radial shell growth, the result is a tapered end segment [51] [53]. Also, the shorter diffusion length of Al compared with Ga [54], enhances this effect.

2.2 Crystal structure

The *crystal structure* of a material describes the arrangement of atoms or molecules in that material [55] [56]. A *Bravais lattice* is a set of points, and the crystal looks

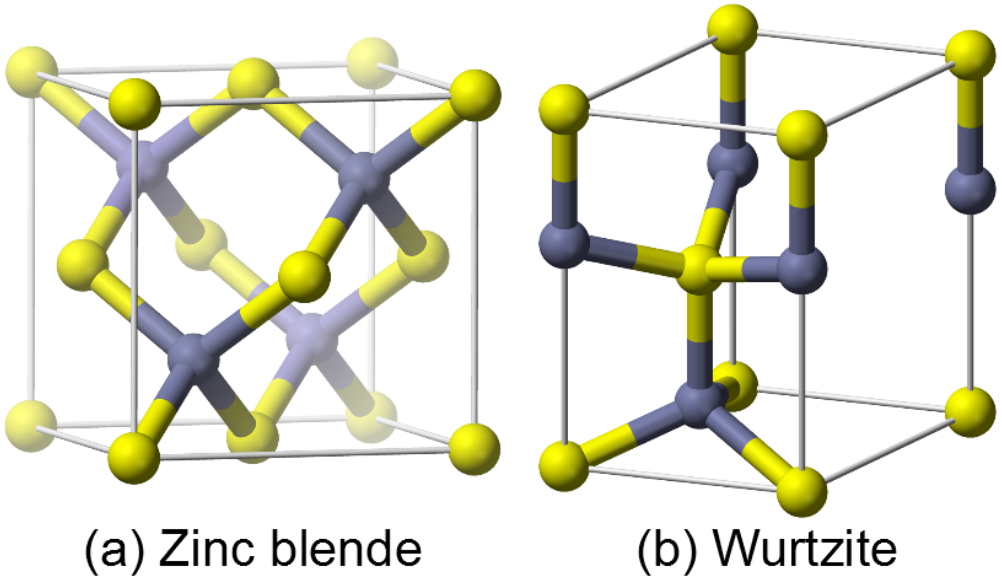

Figure 2.1: Unit cells of ZB (a) and WZ (b), where the yellow and blue atoms represent atom A and B respectively [57].

the same when viewed in any direction, from any of the lattice points. The *unit cell* describes the arrangement of atoms between each lattice point. The unit cell is described by a set of atomic positions, (x, y, z), measured from a lattice point. The values of x, y and z all lie between 0 and 1, where 1 means the atom is shared with the next unit cell.

In bulk phase, GaAs has ZB crystal structure. The ZB structure consists of two inter-penetrating *face-centered cubic* (fcc) Bravais lattices, where the two fcc lattices consists of different atom types, named A and B. This is simply viewed as an fcc lattice with two atoms in the basis: atom A at $(0, 0, 0)$ and atom B at $(\frac{1}{2}, \frac{1}{2}, \frac{1}{2})$. This means that each atom is tetrahedrally coordinated, with four atoms of the other species as its nearest neighbors. By structure, this is the same as a diamond cubic lattice, but with alternating types of atoms at the different lattice sites (Fig. 2.1(a)).

When grown as NWs, GaAs can also exhibit WZ crystal structure [28]. WZ is a hexagonal crystal system, consisting of two different atom types, A and B. Each forms its own *hexagonal close-packed* (hcp) sublattice, but is tetrahedrally coordinated like the ZB structure. The basis for WZ is two atoms of type A at

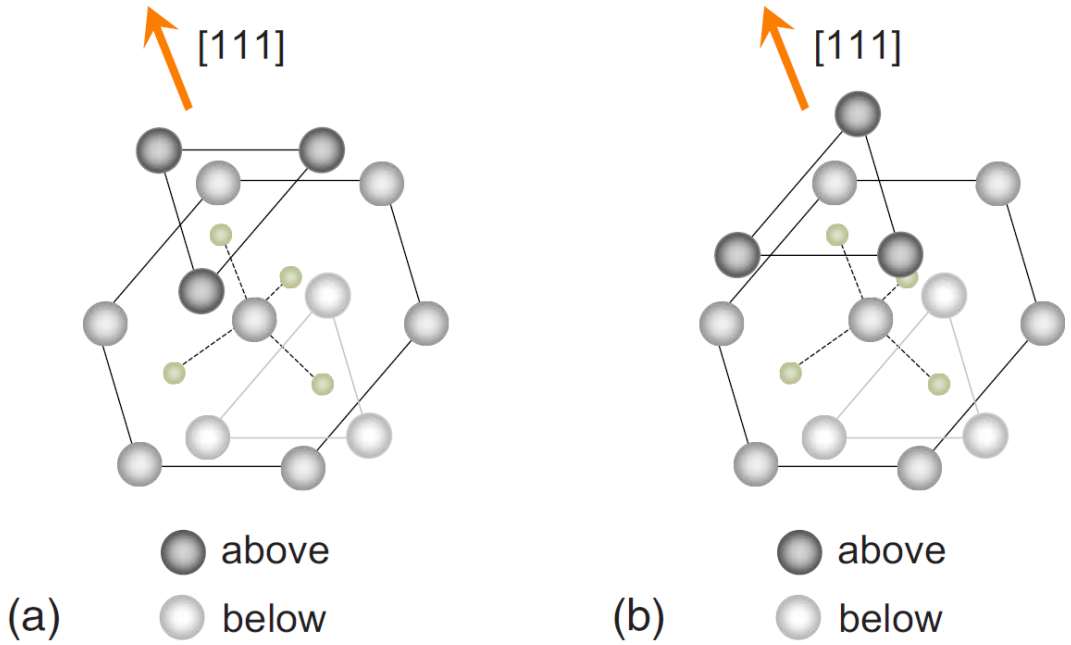

Figure 2.2: ZB (a) and WZ (b) viewed along the [111]. Nine out of the 12 second nearest neighbors are in the same position for the two structures, the top three are rotated by $\frac{\pi}{3}$ [30].

$(\frac{2}{3}, \frac{1}{3}, 0); (\frac{1}{3}, \frac{2}{3}, \frac{1}{2})$ and two type B at $(\frac{2}{3}, \frac{1}{3}, u); (\frac{1}{3}, \frac{2}{3}, \frac{1}{3} + u)$, as illustrated in figure 2.1(b). For binary semiconductors that are metastable in the WZ phase, the value of u tends to be slightly larger than the "ideal" value of $u = \frac{3}{8}$ [58]. The precise value of u is unknown for WZ GaAs.

The difference between ZB and WZ is best illustrated along the [111] direction. It is noted that the top layer of atoms of ZB is rotated by $\frac{\pi}{3}$ with respect to the bottom, whereas the top and bottom layers are symmetrical for WZ (Fig. 2.2).

Both polytypes form stacked hexagonal layers, with alternating layers of atom A and B. The WZ structure features ABAB stacking, whereas ZB has ABCABC stacking (Fig. 2.3). This enables enables formation of twin planes, i.e. one or more layers of WZ in a ZB structure, or vice-versa [59]. The stacking formation of one bilayer of WZ in a ZB structure would be ABCA<u>B</u>|<u>A</u>BC. The underlined BA is the WZ bilayer with the fault line between B and C [60].

Whereas the ZB GaAs crystal phase is understood and fully characterized, there is still controversy surrounding WZ GaAs and its properties. Table 2.1 con-

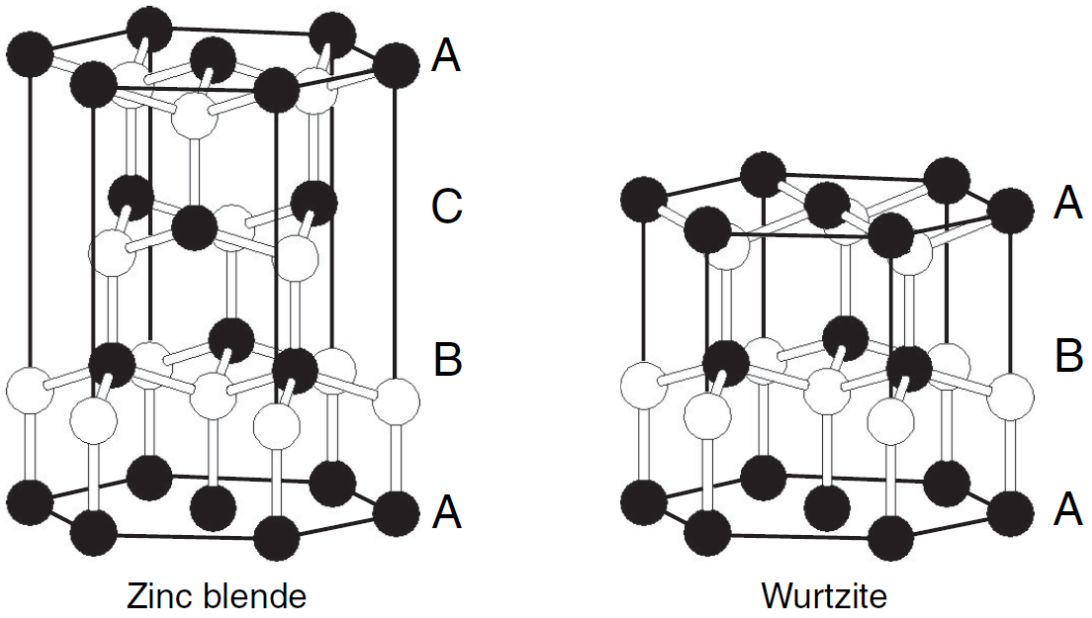

Figure 2.3: ABC stacking of ZB (left) and AB stacking of WZ (right) [58].

Crystal Phase	Zinc Blende (ZB)	Wurtzite (WZ)
Bandgap (at $0K$)	1.519 eV	$E_g(\text{WZ}) \geq E_g(\text{ZB})$ [61]
Free exciton emission ($0K$)	1.515 eV	1.516 eV [61]
Effective electron mass, m_e	$0.067m_0$	$0.25m_0$ [30]
Effective hole mass, m_h	$0.45m_0$	$0.26m_0$ [30]

Table 2.1: ZB and WZ GaAs properties (m_0 = free electron mass). The properties of ZB GaAs are well studied [51], whereas there is controversy around the properties of WZ GaAs.

tains data on both crystal phases, but with some uncertainty for WZ. Descriptions of bandgap, excitons and effective mass follows in section 2.4.

2.2.1 Defects

Any deviation from the infinite, perfect crystal structure is called a *defect* [55] [56]. From this definition, it is clear that every material structure contains several types of defects. There are four main classifications of defects, depending on their dimensionality. These are *point defects*, *line defects*, *planar defects* and *bulk defects*, for 0D, 1D, 2D and 3D respectively. Defects can give rise to discrete energy levels within the bandgap, which makes defects especially harmful for optical devices. See section 2.4.1 and 2.7 for a discussion on how these energy levels affect emitting devices.

Point defects (0D) are defects occurring at a single lattice point, like vacancies, interstitials or impurities. A vacancy is an empty lattice point, that should be occupied by an atom. An interstitial defect is an atom that occupy a site in the crystal that is not a lattice point (i.e. there should not be an atom there). An impurity defect, also called a substitutional defect, is a lattice point that is occupied by an atom that is not supposed to be present in the crystal (Sec. 2.2.2).

Line defects are linear defects (1D), where entire rows of atoms are misaligned. They are discriminated between edge- and screw dislocations. Planar defects (2D) are entire planes where the crystal does not follow its periodic structure. This can be the surface of the crystal, stacking faults, or grain boundaries, where the lattice changes crystallographic direction. Bulk defects (3D) occur when considerable portions of the crystal have significant change in crystal structure. This can be voids, small regions of no atoms, or impurities that have clustered together.

2.2.2 Doping

In many semiconductor devices, impurity defects are intentionally introduced through a process called *doping* [4] [49] [55]. This is done to alter the electrical properties of the semiconductor material. When the atoms introduced have energy levels close to the energy bands of the pure semiconductor, they significantly change the

availability of charge carriers (except at high temperatures). If the impurity atom introduce an energy level close to the valence band, it will increase the number of *positive charge carriers* (holes) in the material, this is called *acceptor* doping. If the impurity introduce an energy level close to the conduction band, the number of *negative charge carriers* (electrons) increase, and this is called *donor* doping. See section 2.4 for more information on energy bands and levels.

Dopant atoms affects excitons, and absorption, as discussed in sections 2.4.5 and 2.7.2.1, respectively.

2.3 Phonons

Atoms in a lattice will vibrate about their equilibrium sites, and these excited states are quantized modes of vibrations [55] [56]. One quantum of energy is called a *phonon*, and these vibrations exhibit wave-particle duality, like the *photons* of electromagnetic waves. The elastic modes can be shown to be harmonic oscillators, with energy given by

$$E = \left(n + \frac{1}{2}\right)\hbar\omega, \tag{2.1}$$

where n is the number of phonons occupying one mode, called the quantum number, and ω is the angular frequency. As seen from the equation, the lowest possible vibrational energy of mode is $\frac{1}{2}\hbar\omega$, the zero point energy.

For a one dimensional monoatomic chain, the angular frequency, ω, as a function of wave number, k, is shown to be

$$\omega(k) = 2\sqrt{\frac{K}{M}}sin\left(\frac{ka}{2}\right), \tag{2.2}$$

where K is the force constant in the harmonic oscillation, M is the mass of the atom/ion and a is the primitive cell size [62]. ω behaves periodically with period $\frac{2\pi}{a}$, so all possible vibrations are given by values of k in the range

$$-\frac{\pi}{a} < k \leq \frac{\pi}{a}. \tag{2.3}$$

If the model is expanded to a one dimensional diatomic chain, with atoms of different masses or bonding strengths, the angular frequencies separate into two

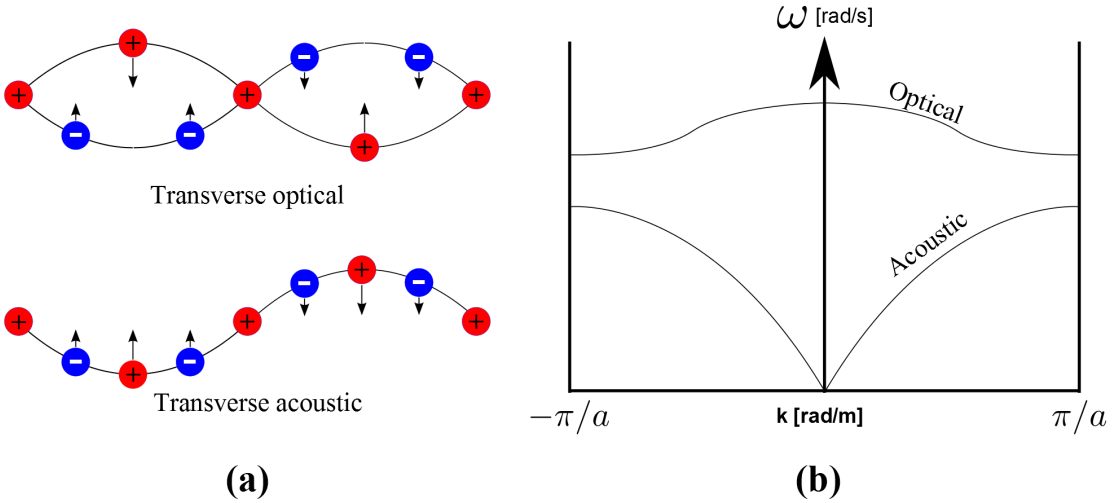

Figure 2.4: (a) Transverse optical and transverse acoustic waves in a diatomic linear lattice, of positive (red) and negative (blue) ions. It is clear that the optical mode also has an electric dipole moment. (b) The acoustic and optical phonon branches, shown as a function of the wave vector, for a diatomic linear chain. The x-axis represents the wave number, k, while the y-axis is the angular frequency, ω.

different modes. This gives rise to two types of phonons, namely *acoustic*- and *optical phonons*, as illustrated in figure 2.4. For acoustic phonons, neighboring atoms oscillate in phase, but unlike acoustic waves, they are not purely transverse nor purely longitudinal. In spite of this, they are called transverse acoustic (TA) and longitudinal acoustic (LA), because they have a predominant polarization. When neighboring atoms oscillate out of phase, they are called optical phonons. They are also labeled transverse optical (TO) or longitudinal optical (LO). Optical phonons can be induced by, and therefore also absorb, electromagnetic waves, hence the name optical. This is because of the electric field created by the oscillating electric dipole. For a material with N atoms in the primitive cell, and $N \geq 2$, there are $3N - 3$ optical modes. There are always 3 acoustical modes, for any N.

In three dimensions, the wave number, k, is instead a wave vector, $\mathbf{k}$. When phonons of wave vector $\mathbf{k}$ propagate through solids, they can interact with photons, neutrons, nuclei and electrons, as if they had momentum $\hbar\mathbf{k}$. The phonon wave vector is a reciprocal lattice vector, and therefore a quasi wave vector. The phonon impulse is therefore a quasi-impulse. This momentum is important in the transition

of electrons between different energy levels, especially in indirect semiconductors. More on energy levels and transitions in sections 2.4, 2.4.1 and 2.4.2

2.4 Energy band theory

All atoms have discrete energy levels that electrons can occupy. When atoms are brought closer together, and the electron orbitals begin to overlap, these energy levels split due to the *Pauli exclusion principle* [55]. In solids, because of the large amount of atoms in close proximity, the energy levels form continuous *energy bands*, which are collections of allowed states that electrons can occupy. Similarly, there are bands that the electrons are not allowed to occupy, called the energy gaps. All solids have their own characteristic energy band structure, which has major implications for the electronic properties of materials.

If electrons are to move in an applied electric field, they need to move from one energy state to another. For this to happen, there has to be allowed unoccupied energy states that the electrons can move to. This implies that in a completely full energy band, there can be no current, because all energy states are occupied by electrons.

Materials fall into four different categories, according to the electron population of the higher energy bands. The categories are metals, semi-metals, insulators and semiconductors. The *valence band* of insulators and semiconductors is the energy band of highest energy that, at $0K$, is completely populated with electrons. The *conduction band* is the band of higher energy than the valence band, with an energy gap between them. The *bandgap energy* (E_g) is the energy difference between the bottom of the conduction band and the top of the valence band.

A metal will have a partially filled conduction band, even at $T = 0K$, thus enabling current to flow. Insulators and semiconductors, however, have a completely full valence band, and empty conduction band at $0K$. This means that there can be no charge transport, and the resistivity is large [49]. The difference between semiconductors and insulators is the width of the bandgap, which is much larger for insulators than for semiconductors [55]. For semi-metals the valence band is filled at $0K$, and the conduction band is empty, but the bands overlap. The four

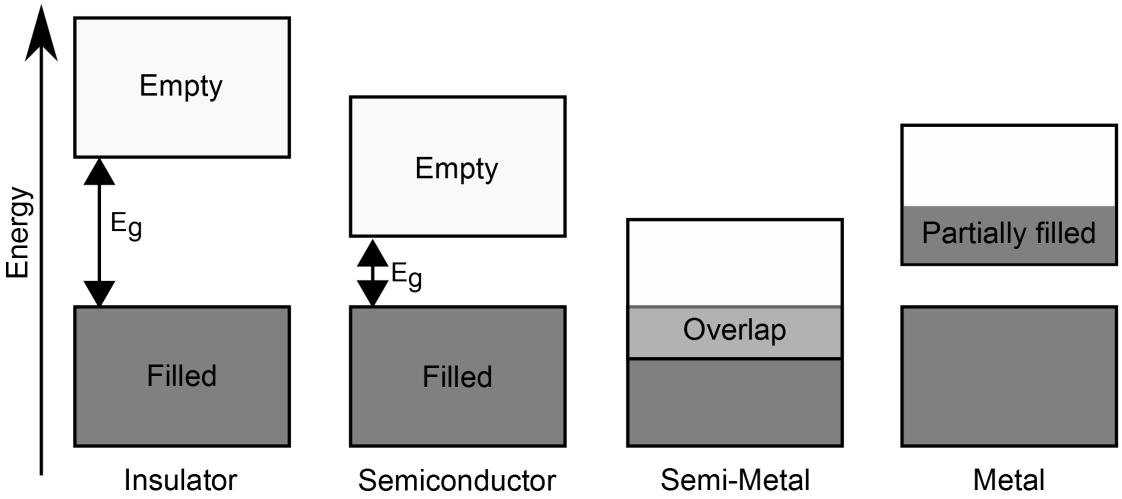

Figure 2.5: Band structure of insulator, semiconductor, semi-metal and metal, at $0K$.

types are illustrated in figure 2.5.

The bandgap of semiconductors is sufficiently small that, with reasonable amounts of optical energy, the electrons can be excited from the valence band into the conduction band. Thus the conductivity of a semiconductor is a property that can be greatly increased by optical excitation.

2.4.1 Band symmetry

In calculations of the energy bands, the electrons are assumed to be traveling in a perfectly periodic lattice. The movement of the electrons is modeled as a plane wave with propagation constant $\mathbf{k}$, called the *wave vector*. $U(\mathbf{k}, \mathbf{r})$ is a periodic function with the same periodicity as the crystal lattice, and the wave function for an electron in such a lattice becomes

$$\psi_{\mathbf{k}}(\mathbf{r}) = U(\mathbf{k}, \mathbf{r})e^{i\mathbf{kr}}. \tag{2.4}$$

Because the periodicity changes in different directions, the wave function is three dimensional. The energy levels can therefore be plotted as a function of $\mathbf{k}$.

For a semiconductor, if the maximum of the valence band and the minimum of the conduction band are both centered around $\mathbf{k} = 0$, it is called a *direct*

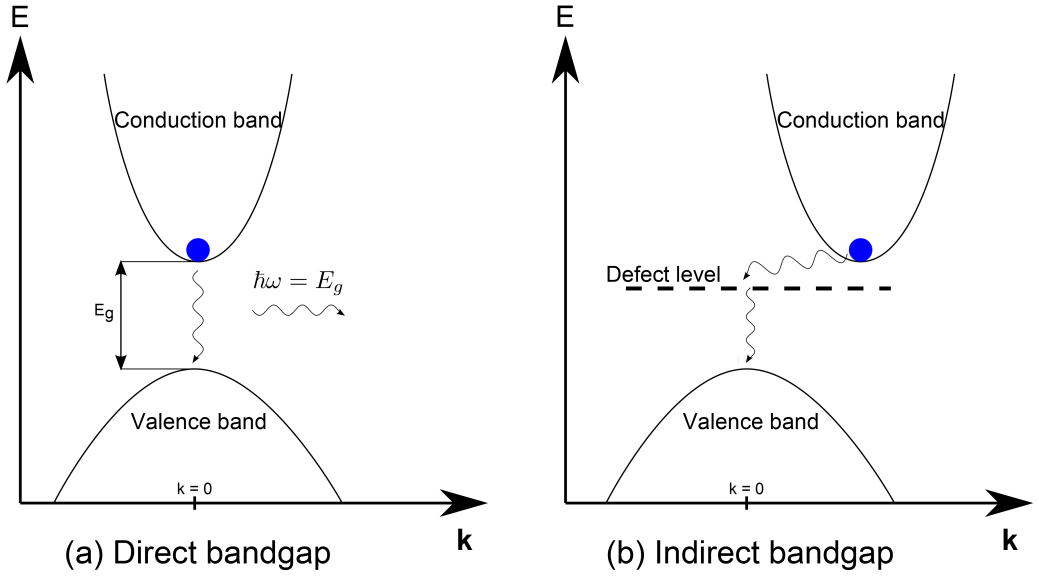

Figure 2.6: Electron transitions in semiconductors. (a) direct transmission, where a photon is emitted. (b) indirect transition via a defect level, no photon emission.

semiconductor. The smallest energy transition the electrons can make is without a change in $\mathbf{k}$, i.e. without a change in momentum. If the maximum and minimum of the bands are not at the same value of $\mathbf{k}$, it is an *indirect semiconductor*. For this case, a change in momentum is required for the transition between states. This change of momentum often comes from interaction with phonons, which will be discussed in section 2.4.2. These interactions drastically reduce the rate of transitions, making indirect transitions detrimental for optical devices. Direct- and indirect transitions are illustrated in figure 2.6 a) and b), respectively.

2.4.2 Electron-phonon interactions

When conducting photoluminescence measurements, the apparent momentum of phonons is important (Sec. 2.3). For electrons excited well into the conduction band, with energy $E > E_c$, the electrons interact with phonons in the lattice, instead of deexciting into the valence band. This process is called *thermalization*. Thermalization happens on the order of hundreds of *femtoseconds* [63], whereas de-excitation of electrons from the conduction band to the valence band takes *nanoseconds*. Because thermalization is in the order of 10^6 times faster than deexcitation,

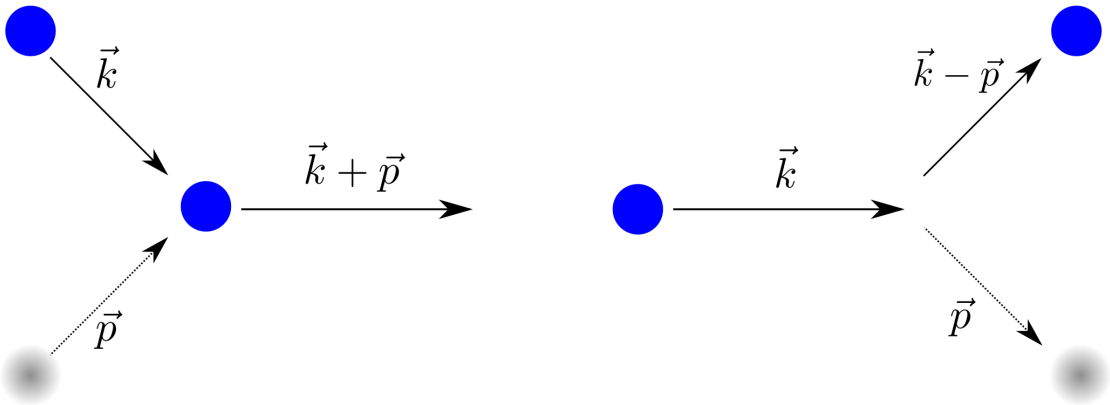

(a) Phonon absorption **(b) Phonon emission**

Figure 2.7: Scattering process: (a) an electron (blue) absorbs a phonon (grey); (b) an electron emits a phonon. Both interactions results in a change in the momentum of the electron.

emission of photons with energy $\hbar\omega > E_g$ is uncommon. This phenomenon is observed when comparing absorption and emission spectra from photoluminescence measurements (Sec. 2.7.2).

For indirect semiconductors, where the electrons need to change their momentum to move between the conduction band and the valence band, electron-phonon interactions are necessary. Electron-phonon interactions are illustrated in figure 2.7.

2.4.3 Band alignment

The electronic properties of ZB and WZ are similar. The room temperature ($294K$) bandgap of ZB is $1.424eV$, while the bandgap of WZ GaAs is proposed to be $20meV$ higher, $1.444eV$, by Ahtapodov et al. [61]. This is attributed to the fact that only three of the 12 nearest neighbors differs (Fig. 2.2), so the crystal potentials are almost identical, apart from a small difference in offset relative to the vacuum level.

The different transitions that can happen in a GaAs solid of WZ and ZB is illustrated in figure 2.8. When an excited electron in the conduction band relaxes to the valence band, it emits a photon with the same energy as the bandgap. When

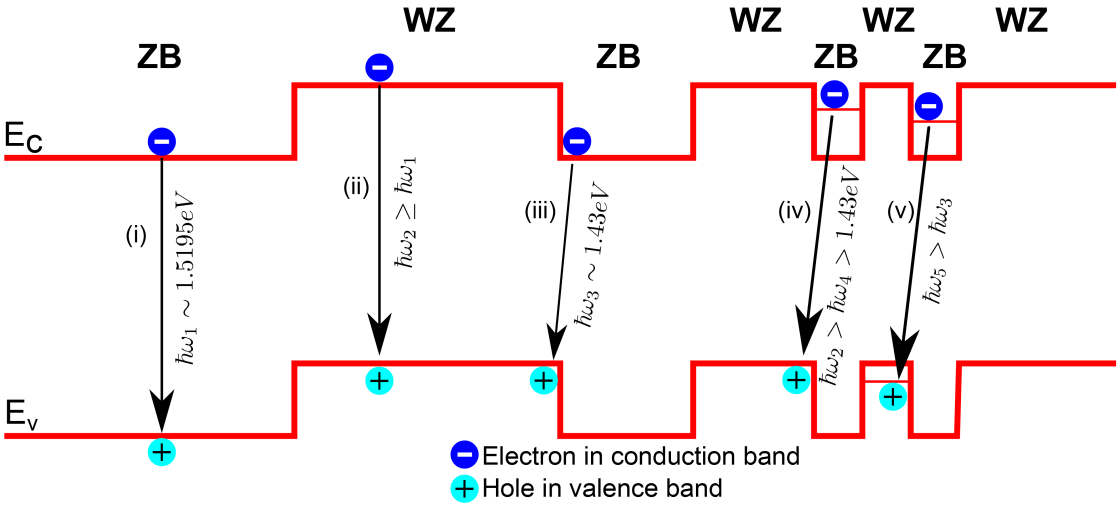

Figure 2.8: Band alignment of ZB and WZ GaAs. Type-I transitions occur when the electron goes from ZB→ZB (i) or WZ→WZ (ii) [51] [61]. Type-II transitions happen from the conduction band of WZ to the valence band of ZB: $WZ_c \rightarrow ZB_v$ (iii) [37]. Quantum wells can arise from stacking faults (Sec. 2.2) of WZ in ZB or vice-versa (iv-v) [64].

the transition happens within an area of no band alignment difference, it is called a type-I transition (Fig. 2.8(i-ii)). This is known as a *straddling gap*. Type-I transitions releases photons of energy $\hbar\omega_1 \sim 1.5195eV$ (ZB) [51] or $\hbar\omega_2 \geq \hbar\omega_1$ (WZ) [61].

The GaAs NWs consist of both ZB and WZ, with many heterointerfaces. It is possible for electrons to recombine from the conduction band of ZB into the valence band of WZ, in what is known as a type-II transition (Fig. 2.8(iii)). This is known as a *staggered gap*. The emission energy will then be smaller than E_g, due to the difference in offset energy for ZB and WZ. For a transition from bulk ZB to bulk WZ the emission energy is $\sim 1.43eV$ [37].

With many interchanging layers of ZB and WZ, the band energies will be subject to quantum confinement effects, thus raising the ZB conduction band energy while lowering the WZ valence band energy (Fig. 2.8(iv-v)). These quantum wells give rise to emission of energies above $1.43eV$ [64], as is illustrated.

Calculated diagrams of the band structures of WZ and ZB GaAs can be seen in figures 2.9 and 2.10 respectively.

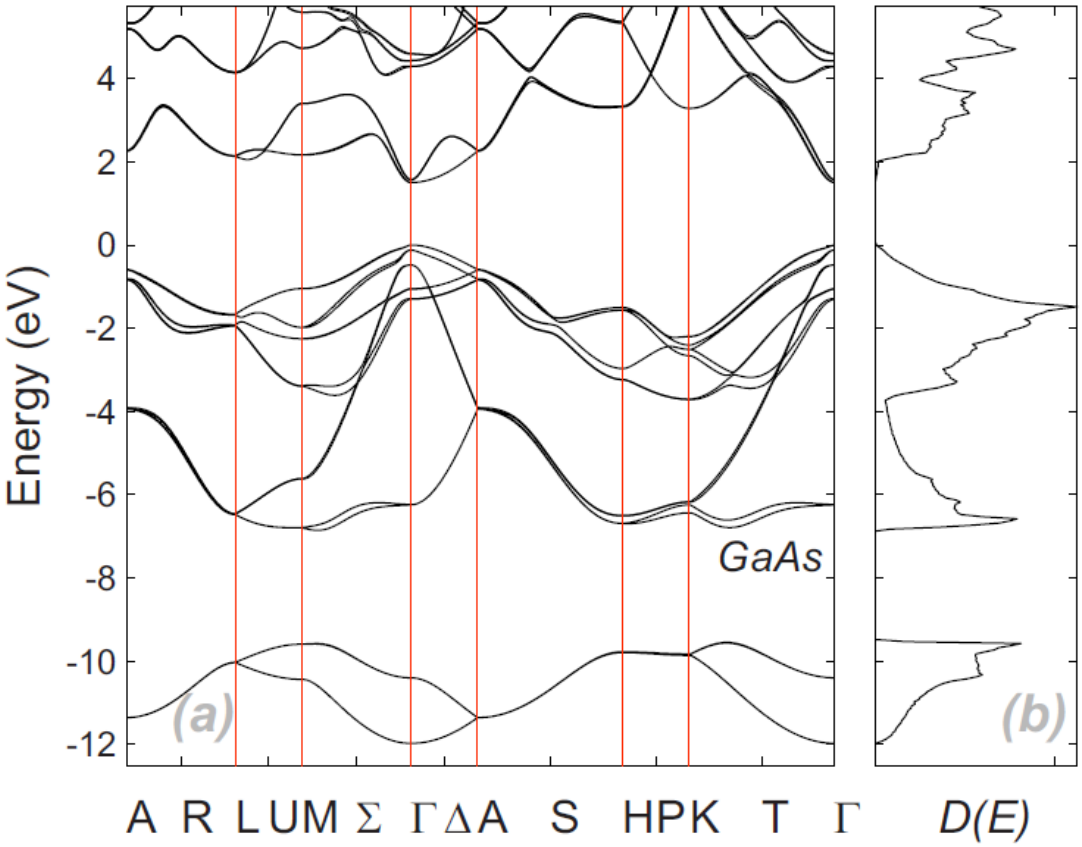

Figure 2.9: Band structure of WZ GaAs (a), calculated using pseudopotentials. The Γ point indicates the direct bandgap, and E_g is determined to $1.503eV$ (from Γ_9 to Γ_8). The density of states (Sec 2.5) is also plotted (b) [30].

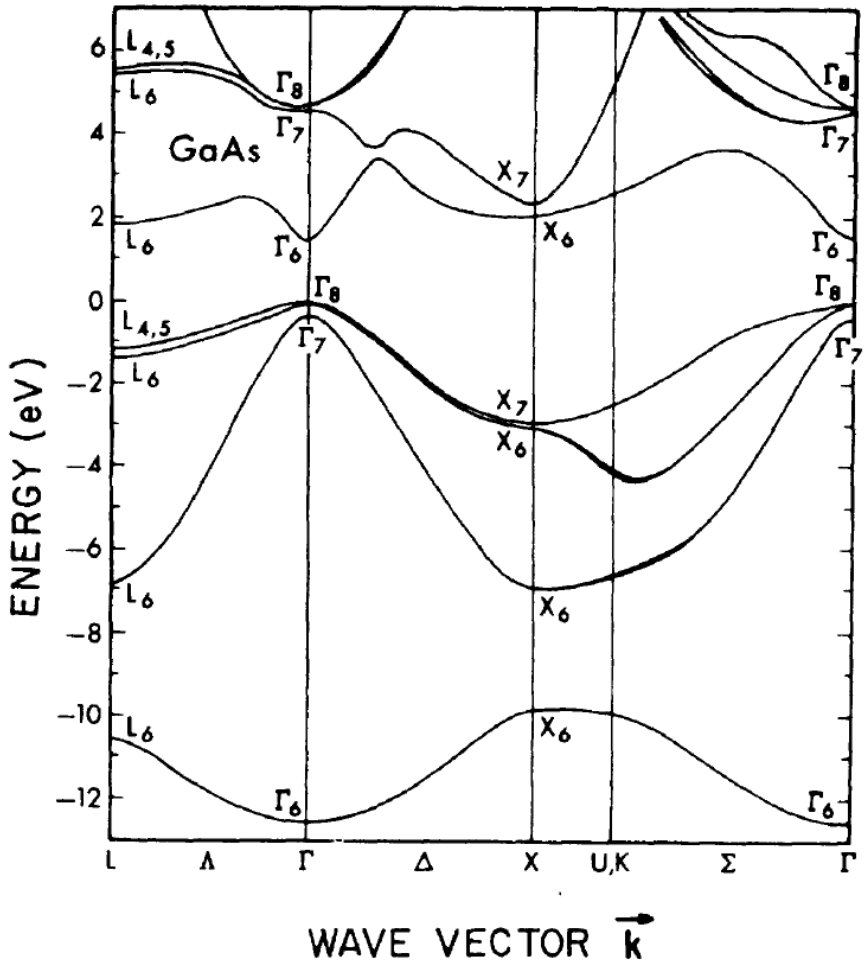

Figure 2.10: Band structure of ZB GaAs, calculated using pseudopotentials. The Γ point indicates the direct bandgap, and E_g is determined to $1.51eV$ (from Γ_8 to Γ_6) [47].

2.4.4 Effective mass

The mass of an electron (m_e) is clearly defined when the electron is moving freely. In a solid crystal, however, the electrons are subjected to a periodic potential (Sec. 2.4.1), thus they do not move freely. By defining the *effective mass*, m^*, (a property that depends on the direction of motion) and using this instead of m_e, the usual equations of electrodynamics can still be used to explain the movements of charge carriers in the solid.

The E($\mathbf{k}$) relationship can be found from the definition of kinetic energy, using $p = mv = \hbar\mathbf{k}$, giving

$$E = \frac{1}{2}mv^2 = \frac{1}{2}\frac{p^2}{m} = \frac{\hbar^2}{2m}\mathbf{k}^2. \tag{2.5}$$

So the energy is parabolic with $\mathbf{k}$. The electrons in a solid are not free, but when approaching a band extrema the dispersion is close to parabolic, and can be Taylor expanded. Neglecting the linear term (which is equal to 0 at extrema) the expansion becomes [55]

$$E(\mathbf{k}) = E_0 + \frac{1}{2}\sum_{i,j=x,y,z}\frac{d^2E}{d^2\mathbf{k}_{ij}}(\mathbf{k}-\mathbf{k}_0)_i(\mathbf{k}-\mathbf{k}_0)_j. \tag{2.6}$$

From this, the effective mass is defined. With the constant term ignored (only interested in relative energy), we get

$$\frac{1}{m^*_{ij}} = \hbar^2\sum_{i,j=x,y,z}\frac{d^2E}{d^2\mathbf{k}_{ij}}. \tag{2.7}$$

Thus the effective mass depends on the direction of motion, which is to be expected with a 3D potential. From the definition, it is clear that the effective mass is positive when the energy band considered is at a minima. When the energy band has a maxima, however, the effective mass has a negative value. Reviewing the curvature in figure 2.6, we see that a positive effective mass occurs at conduction band minima, while the effective mass is negative at valence band maxima.

The physical interpretation of this is understood by regarding the current density, $\mathbf{j} = \frac{q_e n \mathbf{p}}{m^*}$, especially the sign of $\frac{q_e}{m^*}$. For electrons ($q_e < 0$) moving in the

conduction band minima ($m^* > 0$), $\frac{q_e}{m^*} < 0$, and thus the current $\mathbf{j}$ moves in the opposite direction of the electrons, $\mathbf{p}$, as is convention. For electrons in the valence band maxima ($m^* < 0$), the negative values cancel ($\frac{q_e}{m^*} > 0$) and $\mathbf{j}$ is in the same direction as $\mathbf{p}$. I.e. we can view this phenomena as a positively charged particle moving in the direction of the electric field. Since this particle can only exist inside the solid, it is a quasiparticle, and is called a *hole* (h^+). The concepts of holes and effective mass are only valid close to band extrema.

Since a moving hole is essentially the movement of several electrons, the mobility of a hole is lower than that of a free electron. It follows that the effective mass must be larger. The following section will discuss the joint movement of holes and electrons

2.4.5 Excitons

When the material absorbs a photon, an electron is excited from the valence to the conduction band. It leaves behind a vacant orbital in the otherwise filled valence band (which other electrons can move into), along with a now positively charged lattice atom. This open state is called a hole, a positively charged quasiparticle (see section 2.4.4). The electron and hole are free to move in their respective bands, thus generating current.

Being of opposite charge, the electron in the conduction band will be bound to the hole in the valence band, by electrostatic Coulomb force. This bound state is called an *exciton* [65], and behaves much like a hydrogen atom [55]. The energy structure of hydrogen-like particles depends largely on the distance between them, and the dielectric constant in which they are located. For hydrogen, the distance is small and the dielectric constant is unity (vacuum). For an exciton in a semiconductor material these values are both much larger.

Two kinds of excitons are relevant; Frenkel excitons [66], with a small separation between hole and electron, and Mott-Wannier [67] excitons with large separation. This discussion is regarding semiconductor crystals, and will therefore focus on Mott-Wannier excitons. They experience significant screening of the Coulomb force, resulting in a small binding energy on the order of $0.01eV$, and a

radius larger than the lattice spacing.

This quasiparticle is electrically neutral, and the attraction provides a stabilizing energy, meaning the exciton has lower energy than the unbound electron and hole. This enables an electron in the valence band to absorb a photon of energy slightly less than the bandgap, $\hbar\omega < E_g$

The conduction band has an abundance of free orbitals, whereas the valence band is almost filled. This results in many overlapping wave functions in the valence band, and Pauli repulsion between the electrons. As proposed by Scholes et al. [68], the formation of excitons may also be interpreted as less Pauli repulsion due to lower population in the conduction band.

There are several types of excitons. Excitons in a perfect lattice are free particles, called *free excitons*. Because free excitons only need an electron and a hole to exist, the number of free excitons is not limited. In a real lattice, however, some excitons will bind to defects and impurities in the lattice, where it is energetically favorable. These excitons are called *bound excitons*, and the defects can be dopant atoms, impurities etc. The exciton energy is thus further reduced, enabling absorption and emission of photons of lower energy than those of free excitons. Bound exciton energy depends on the type of impurity it is bound to. From donor and acceptor atoms, three types of excitons can arise [69], namely excitons bound to neutral acceptor (A^0, X), neutral donor (D^0, X) and ionized donor atoms (D^-, X), with decreasing binding energy. Thus three different emission lines can occur from dopant atoms, due to bound exciton levels.

The number of bound excitons in a lattice is limited by the number of defects available for binding. Therefore, in a photoluminescence experiment, the observed emission intensity will have a sublinear dependence on *laser excitation power*. This happens because, as the laser power increases, the number of bound exciton states will saturate. For free excitons, however, the emission intensity will have linear dependence on laser power, since the population of free excitons can be increased for pure materials.

Another type of excitons, *biexcitons*, are excitonic molecules consisting of two free excitons in bonding [70]. The energy of a biexciton is lower than that of an

exciton, resulting in emission of photons slightly below the free exciton emission. This energy peak grows faster than that of free excitons, resulting in a superlinear dependence on laser power.

2.4.6 Temperature dependence

The bandgap energy, E_g, of semiconductors will change depending on temperature [71]. This was found empirically by Y.P. Varshni in 1967 [72]. At low temperature E_g reaches saturation, and thus changes non-linearly with temperature. This can be explained by dilation of the lattice, which moves the conduction band relative to the valence band. This mechanism is due to changes in the crystal potential which is affected by core-core, core-electron and electron-electron interactions [55], all of which change with temperature and influence E_g. This dilation is non-linear at low temperature and linear at high temperatures [72].

At high temperatures, however, this effect accounts for only $\sim 25\%$ of the observed change in E_g. Due to the significant increase in the number of phonons, electron-phonon interactions will become more dominant as the temperature increases. At high temperatures E_g changes linearly with temperature. This shift happens approximately at the *Debye temperature* [73].

Two models are used to describe the temperature dependence of E_g, the Varshni model [72] and the modified Varshni model [74], as displayed in equation (2.8) and (2.9) respectively

$$E_g(T) = E_g(0) - \alpha T^2(T - \beta), \tag{2.8}$$

$$E_g(T) = E_g(0) - \frac{\alpha_{mod} T^4}{\beta_{mod} + T^3}, \tag{2.9}$$

where α and β are material constants with units eV/K^3 and K respectively, for α_{mod} and β_{mod} the units are eV/K and K^3 respectively. A typical plot of $E_g(T)$ can be seen in 2.11.

When temperature dependent photoluminescence measurements are done on the SC GaAs NWs, the Varshni and modified Varshni models are used to explain the results.

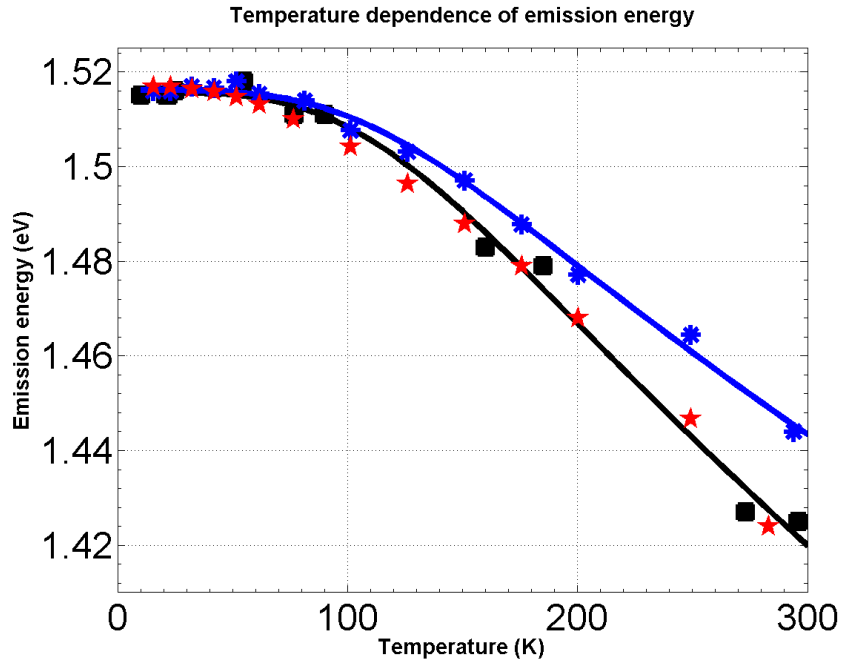

Figure 2.11: Plot showing the temperature dependence of the energy gap of GaAs. Included is **WZ GaAs** [61], **bulk ZB GaAs** [75] and a **ZB GaAs epilayer** [61].

2.5 Density of states

The *density of states* (DOS) is an important concept in solid state physics that describes the number of energy states allowed for electrons, per interval of energy. When the DOS is 0, it means that there are no allowed states, while a high DOS means that there are many states available. The density of states over a given energy interval $[E(\mathbf{k}), E(\mathbf{k}) + dE]$ is given by [55]

$$D(E) = \left(\frac{L}{2\pi}\right)^3 \int_{shell} \frac{d^3\mathbf{k}}{dE}, \tag{2.10}$$

where $D(E)$ denotes the DOS at energy E. The integral is extended over $\left(\frac{L}{2\pi}\right)^3$, i.e. the volume of the shell in $\mathbf{k}$ space bounded by the two constant energy surfaces of energy $E(\mathbf{k})$ and $E(\mathbf{k} + d\mathbf{k})$ respectively.

The volume of this shell then has to be evaluated. For a constant energy, dS_E denotes an element of area. The volume between the surface of energy $E(\mathbf{k})$ and

$E(\mathbf{k}) + dE$ is then a cylinder of height $dK_\perp$ and base area dS_E

$$\int_{shell} d^3\mathbf{k} = \int dS_E dK_\perp. \tag{2.11}$$

The gradient of E, $\nabla_\mathbf{k} E$, is also perpendicular to $dK_\perp$, and we get

$$dE = |\nabla_\mathbf{k} E| dK_\perp, \tag{2.12}$$

thus the volume becomes

$$dS_E dK_\perp = \frac{dS_E}{|\nabla_\mathbf{k} E|} dE. \tag{2.13}$$

Equation (2.10) then equates to

$$D(E) = \left(\frac{L}{2\pi}\right)^3 \int \frac{dS_E}{|\nabla_\mathbf{k} E|}. \tag{2.14}$$

Finally, by inserting values for free electrons in a Fermi gas (with $E = \frac{\hbar^2 k^2}{2m^*}$), we get expressions for the DOS in one, two and three dimensions respectively:

$$1D : D(E) = \frac{V_1}{\pi} \left(\frac{2m^*}{\hbar^2}\right)^{1/2} \frac{1}{\sqrt{E}}, \tag{2.15}$$

$$2D : D(E) = \frac{V_2}{2\pi} \left(\frac{2m^*}{\hbar^2}\right), \tag{2.16}$$

$$3D : D(E) = \frac{V_3}{2\pi^2} \left(\frac{2m^*}{\hbar^2}\right)^{3/2} \sqrt{E}. \tag{2.17}$$

These equations represents the DOS for sub-bands.

Figure 2.12 illustrates how the DOS changes with energy according to equations (2.15)-(2.17). The plots in the figure are clearly non-differentiable for 1D and 2D. This is attributed to the "particle-in-a-box" levels that occur for lower dimensionalities [49]. Because of the restricted number of atoms in 1D and 2D systems, the number of available states for the electrons is also restricted. This in turn limits the DOS. As the energy of the system increases above certain limits, electrons can enter newly available bands, causing sudden changes in the DOS.

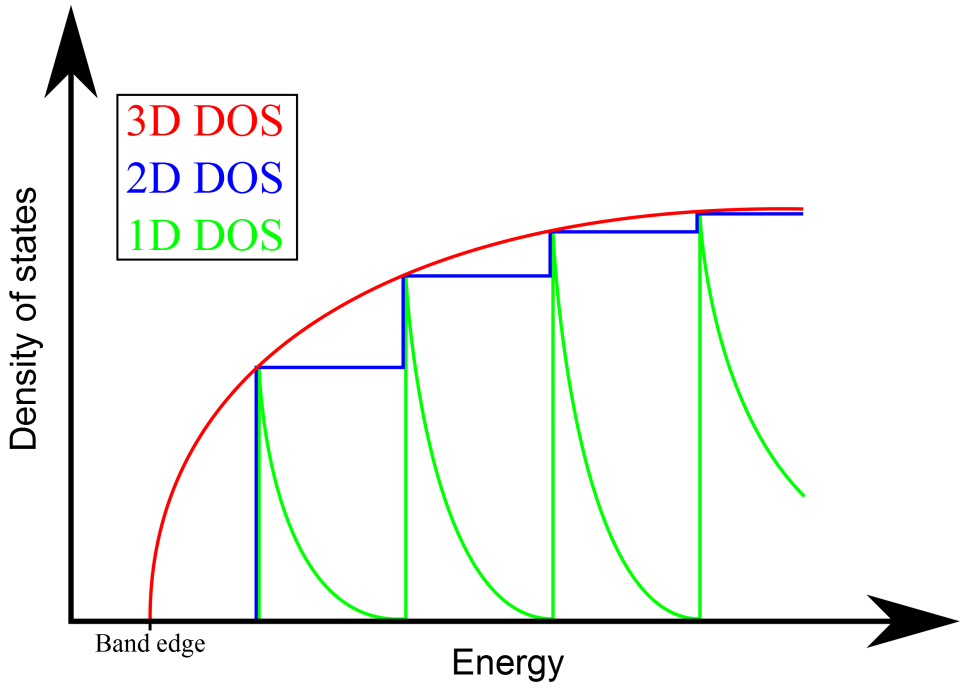

Figure 2.12: The DOS for one-, two- and three dimensions, from equations (2.15)-(2.17) respectively. "Particle-in-a-box" levels cause non-continuous plots for one- and two dimensions, and higher DOS at the lowest available energy. This is utilized in light-emitting devices.

For a 2D system, when a new band is added, the previous bands are still allowed. For 1D systems, however, the DOS in a sub-band is proportional to $(1/\sqrt{E})$, leading to confinement of electrons. It is evident that by lowering the dimensionality of the volume to 1D, the DOS becomes higher at the lowest available energy. It is at this energy, closest to the band edge, that light emission is most efficient [51], which is an important principle utilized in light-emitting devices. When analyzing the optical absorption spectra it is noticed that some irregularities occur. This phenomenon happens when the DOS is not differentiable, and is known as van't Hove singularities [76].

2.5.1 Joint density of states

The joint DOS is the density of states, separated by a certain amount of energy close to the bandgap energy E_g. This is introduced because in an emission process,

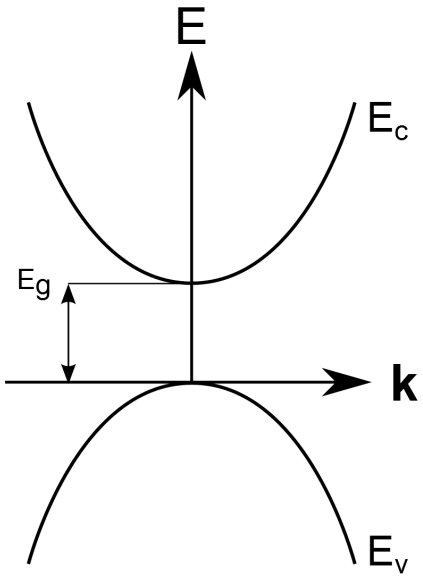

Figure 2.13: Quadratic approximation plot of energy and wave vector, for the valence- and conduction band, close to extrema. $E_c(k)$ and $E_v(k)$ are expressed by equations (2.18) and (2.19), respectively.

the electrons move from one energy state in the conduction band, to another energy state in the valence band. The energy that separates these states is equal or close to E_g. Close to extrema the band curves are estimated as quadratic expressions, as shown in figure 2.13. The expressions are

$$E_c(k) = E_g + \frac{\hbar^2 k^2}{2m_e^*}, \tag{2.18}$$

$$E_v(k) = -\frac{\hbar^2 k^2}{2m_h^*}. \tag{2.19}$$

During the emission or absorption of a photon of energy $\hbar\omega$, the equation becomes

$$\hbar\omega = E_c(k) - E_v(k) = E_g + \frac{\hbar^2 k^2}{2}\left[\frac{1}{m_e^*} + \frac{1}{m_h^*}\right] = E_g + \frac{\hbar^2 k^2}{2\mu}, \tag{2.20}$$

where μ is the reduced mass $\left(\frac{1}{\mu} = \frac{1}{m_e^*} + \frac{1}{m_h^*}\right)$. Solving for k gives

$$k = \frac{1}{k}\sqrt{2\mu(\hbar\omega - E_g)}, \tag{2.21}$$

and the joint DOS equates to

$$1D : D(\hbar\omega) = \frac{1}{\pi}\left(\frac{2\mu}{\hbar^2}\right)^{1/2}\frac{1}{\sqrt{\hbar\omega - E_g}}, \tag{2.22}$$

$$2D : D(\hbar\omega) = \frac{1}{2\pi}\left(\frac{2\mu}{\hbar^2}\right), \tag{2.23}$$

$$3D : D(\hbar\omega) = \frac{1}{2\pi^2}\left(\frac{2\mu}{\hbar^2}\right)^{3/2}\sqrt{\hbar\omega - E_g}. \tag{2.24}$$

Because photons emitted in photoluminescence experiments usually has energy $\hbar\omega$ very close to E_g, equations (2.22)-(2.24) are the relevant equations for this discussion, instead of (2.15)-(2.17).

2.6 Carrier statistics

Carrier statistics is used in statistical mechanics to describe the probability distribution of material particles (or quasiparticles) over various energy states in thermal equilibrium. From quantum mechanics, particles belong to one of two classes of elementary particles. They are classified according to their spin, which can have integer or half-odd-integer values [77].

Integer spin particles are called *bosons*, and any number of bosons can have the same quantum state. That is, they are not limited to single particle occupancy of one state. Non-integer spin particles, called *fermions*, are not allowed to occupy the same quantum state. That is, fermions follow the restrictions set by the Pauli exclusion principle [55], whereas bosons do not.

When working with indistinguishable particles, Bose-Einstein and Fermi-Dirac statistics describes the distribution of bosons and fermions, respectively. These are expressed by equations (2.25) and (2.26).

$$f_{BE}(E) = \frac{1}{exp\left(\frac{E-\mu}{k_B T}\right) - 1}, \tag{2.25}$$

$$f_{FD}(E) = \frac{1}{exp\left(\frac{E-\mu}{k_B T}\right) + 1}. \tag{2.26}$$

The chemical potential, μ, is chosen for the particular problem so that the total number of particles in the system comes out correctly. For a system of electrons,

μ is known as the *Fermi level*, and can be defined as the energy level with 50% probability of being occupied, or the topmost filled level in the ground state [55]. The Fermi level is a function of temperature, $\mu(T)$, but also depend on other factors that can induce changes in carrier concentration, such as doping concentration. At absolute zero temperature, the Fermi level is equal to the *Fermi energy*

Examples of bosons following the f_{BE}-distribution are photons, phonons and excitons. Fermions following f_{FD}-distribution can be electrons, holes, protons and neutrons.

If the temperature is high enough, and the density low enough, however, quantum effects become negligible as the particle wave functions do not overlap appreciably [77]. This happens when $E - \mu \gg k_B T$, and under these conditions the probability distribution of both bosons and fermions are expressed by Maxwell-Boltzmann statistics, equation (2.27). This equation also applies to classical distinguishable particles.

$$f_{MB}(E) = exp\left(-\frac{E-\mu}{k_B T}\right) \tag{2.27}$$

Figure 2.14 illustrates the three different distribution functions.

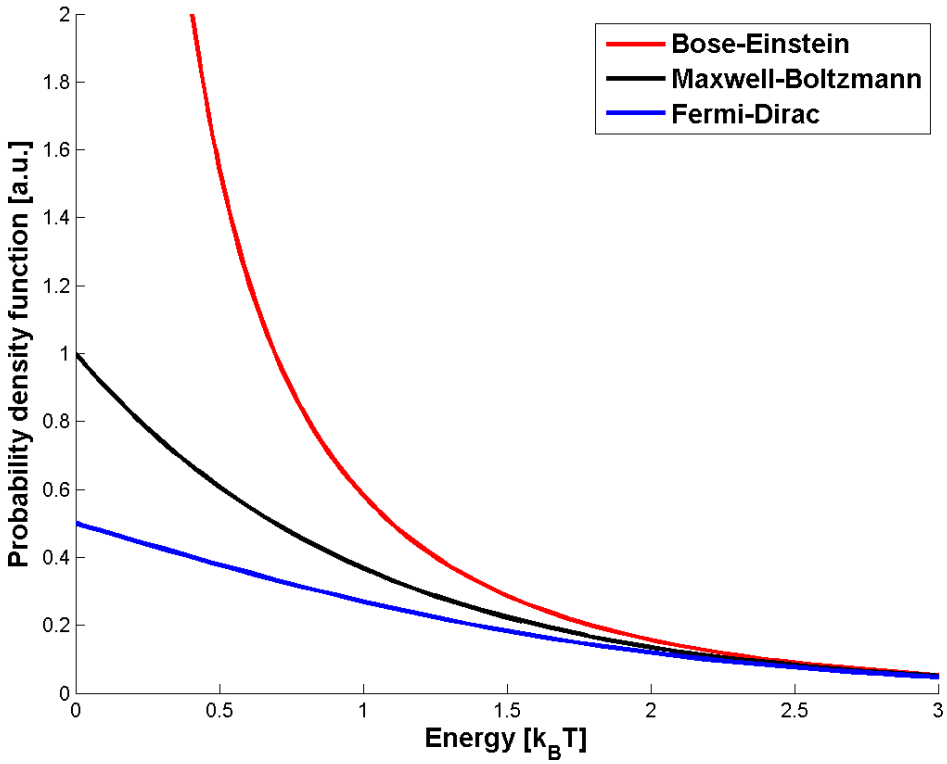

Figure 2.14: A plot of the Bose-Einstein-, Fermi-Dirac- and Maxwell-Boltzmann distribution, equations (2.25), (2.26) and (2.27) respectively. The plot shows that the Fermi-Dirac and Bose-Einstein functions reduce to Maxwell-Boltzmann for $E - \mu \gg k_B T$.

2.7 Photoluminescence

Photoluminescence (PL) is a process where a material absorb incoming photons, then re-radiate photons. The method is used to investigate many properties of a sample, including bandgap, selection rules, purity, strain, carrier lifetimes, mobility etc [78]. It has high sensitivity, and can be completely non-destructive, making it useful for characterization of both organic and inorganic materials, including semiconductors. The process is explained in this section, with references to figure 2.15.

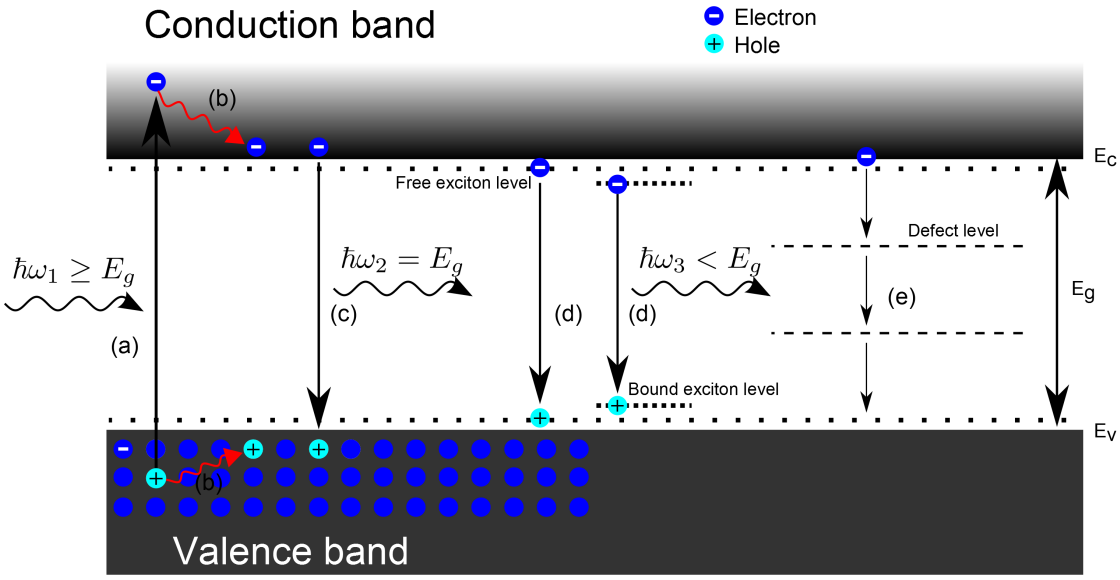

Figure 2.15: Step by step description of the absorption and emission of photons in photoluminescence. Blue circles represent electrons, white circles represent holes. Straight arrows are energy transitions, curved arrows are photons, and dashed lines are exciton/defect levels.

a. Electrons in the valence band, $E \leq E_v$, can absorb photons of energy $\hbar\omega_1 \geq E_g$, and thus be excited into a higher energy state, in the conduction band, $E \geq E_c$.

b. If $\hbar\omega_1 > E_g$, the electrons will be excited well into the conduction band, but will subsequently relax to the bottom of the band, E_c. This happens through collisions and interactions with phonons, in a process called thermalization

(Sec. 2.4.2). A hole generated below the valence band edge E_v, will undergo a similar process until it reaches the band edge. Thermalization in GaAs happens within hundreds of femtoseconds [63].

c. When the electron and hole has reached the edge of their respective bands, they will eventually recombine. This occurs when the electron jumps from the conduction band to the valence band, eliminating the hole. A photon is released with energy equal to the difference between the two states, $\hbar\omega_2 = E_c - E_v = E_g$. The duration of this process is in the order of *nanoseconds* [49].

d. Recombination also happens with emitted photons of energy $\hbar\omega_3 < E_g$. This is illustrated here by excitonic levels (Sec. 2.4.5). The excitons can be *free excitons* or *bound excitons*, where the latter has lower emission energy, as illustrated. At low temperatures, emission of photons above the free exciton levels will not occur. Emission of $\hbar\omega_3 < E_g$ can also occur due to impurity/defect states within the bandgap, for example those introduced by acceptor and donor atoms (Sec. 2.2.2).

e. With enough available states within the bandgap, non-radiative recombination can occur [79] [80]. If the material has a significant number of impurities and defects the probability increases drastically, which is detrimental to PL experiments.

It is process (c) and (d) that make up the observed signal in PL experiments. The relative intensity of (c) indicates the rate of direct recombination, while other intensity peaks originate from (d).

An incoming photon can also stimulate emission of a photon of the exact same energy and phase. This gives two photons, and the process can grow exponentially as long as there are available conduction band electrons [81]. Emission will be more probable than absorption as long as there are more electrons in the conduction band than the valence band, known as population inversion. This process is utilized in semiconductor lasers.

2.7.1 Fermi's Golden Rule

Fermi's Golden Rule enables us to better understand the optical properties of solids, i.e. the interaction between light and matter [82] [83] [84]. It is important to find expressions describing the electronic transitions in solids, together with the process of light absorption and emission. When the rate of transitions between different bands is constant in time, it is expressed by Fermi's Golden Rule:

$$W_{i\to j} = \frac{\partial}{\partial t}\left|C_{ij}^{(1)}\right|^2 = \frac{2\pi e^2}{\hbar^2}|z_{ji}|^2|E_z|^2\delta(\omega_{ji}-\omega). \tag{2.28}$$

Here $W_{i\to j}$ is the transition rate (probability of transition per unit time), between energy state $i \to j$, for a single isolated atom. $|z_{ji}|^2$ are the dipole matrix elements. These contain the selection rules, which are determined by symmetry considerations. The transition is allowed for all values except $|z_{ji}|^2 = 0$, in which case it is forbidden.

The selection rules for GaAs NWs can be found in [85]. It is the Γ-point selection rules that are most important for GaAs because this is where the direct bandgap is situated, as discussed in section 2.4.1. For direct bandgap materials, the $|z_{ji}|^2$ factor will maintain the momentum conservation requirement, in addition to the selection rules.

Equation (2.28) is only valid for a single isolated atom, so it must be expanded for a solid crystal structure to be useful. A solid will not consist of single energy levels expressed by the delta function $\delta(\omega_{ji}-\omega)$ (the density of states for a single atom), but by quasi-continuous energy bands. All possible absorption possibilities are expressed by $D(\omega_g-\omega)$, the joint density of states (Sec. 2.5.1). Fermi-Dirac statistics for electrons (Sec. 2.6) gives that the transition probability is proportional to both the number of occupied initial states, $f_{FD}(E_i)$, and the number of vacant final states, $[1-f_{FD}(E_j)]$, where f_{FD} is given by equation (2.26). This is incorporated by multiplying the joint density of states with $f_{FD}(E_i)[1-f_{FD}(E_j)]$.

The following equations are obtained for adsorption and emission, respectively:

$$W_{v\to c} = \frac{2\pi e^2}{\hbar^2}|z_{cv}|^2|E_z|^2 D(\omega_g - \omega) f_{FD}(E_v)[1 - f_{FD}(E_c)], \tag{2.29}$$

$$W_{c\to v} = \frac{2\pi e^2}{\hbar^2}|z_{vc}|^2|E_z|^2 D(\omega_g - \omega) f_{FD}(E_c)[1 - f_{FD}(E_v)]. \tag{2.30}$$

Note that the population factors constitute the only difference between the two transition rates.

2.7.2 Absorption and emission in photoluminescence

The absorption and emission process was discussed in section 2.7, and Fermi's Golden Rule in section 2.7.1. The latter affects the former, and the knowledge will be used in a new review of absorption and emission in this section. In addition we will add our knowledge on doping (Sec. 2.2.2), phonons (Sec. 2.3) and excitons (Sec. 2.4.5).

2.7.2.1 Absorption

Equation (2.29) gives the transition rate of electrons moving from the valence band to the conduction band, $W_{v\to c}$, the rate of absorption. According to this equation, photons of energy $\hbar\omega \geq E_g$ can be absorbed and excite an electron. Since the valence band is initially considered occupied by electrons, while the conduction band is almost empty, absorption is allowed for a wide range of frequencies.

Absorption can also be observed for wavelengths above a certain level. The longer wavelengths (lower energies) are absorbed by excitation of optical phonons [55]. The exponential decrease in transmission, or increase in absorption, when nearing the bandgap (Fig. 2.16), is due to a phenomenon called the Urbach Optical-Absorption Edge (or Urbach tail) [86] [87], and is assumed to arise from "tails" in the DOS.

Even though equation (2.29) gives $W_{v\to c} = 0$ for $\hbar\omega < E_g$ (because $D(\omega_g - \omega) = 0$), photons of energy $\hbar\omega < E_g$ can be absorbed due to the existence of excitons and impurities. At very low temperatures, when electrons are still localized to their donor atoms (and holes to their acceptor atoms), absorption of low energy

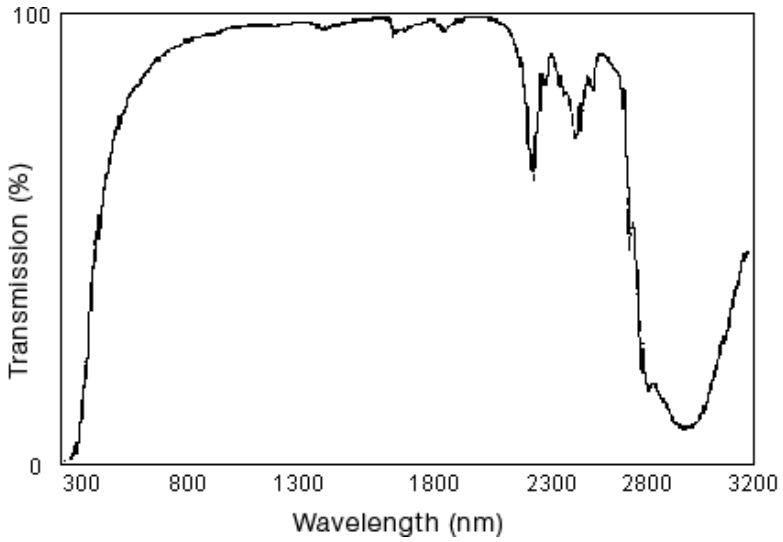

Figure 2.16: Transmission spectrum for a silica aerogel [88], but the result is general and can be applied to GaAs. The bandgap is located near $300nm$, where transmission suddenly cuts off. Transmission decreases again around $2800nm$, due to phonon absorption.

infrared (IR) light can occur. This happens when electrons are excited from their donor levels E_d, to the conduction band E_c, causing sharp absorption lines, $\hbar\omega = E_c - E_d$. At higher temperatures, when nearly all donor electrons are excited into the conduction band, excitation from the valence band to the donor levels is possible, $\hbar\omega = E_d - E_v$. Since this energy is close to E_g, exact determination of the bandgap can be difficult.

Figure 2.17 show two excitonic absorption peaks, and the transition to band-to-band absorption (where $\hbar\omega \geq E_g$).

2.7.2.2 Emission

An emission spectrum might be expected to have an approximately inverse shape of the transmission spectrum in figure 2.16. The rate of emission, given by equation (2.30), also gives a very similar formula for $W_{c\to v}$ as the rate of absorption given by equation (2.29). But due to thermalization effects, the emission spectrum is quite different from the transmission spectrum. As illustrated in figure 2.15(b); when an electron absorb a photon of $\hbar\omega > E_g$, it will be excited to a state above

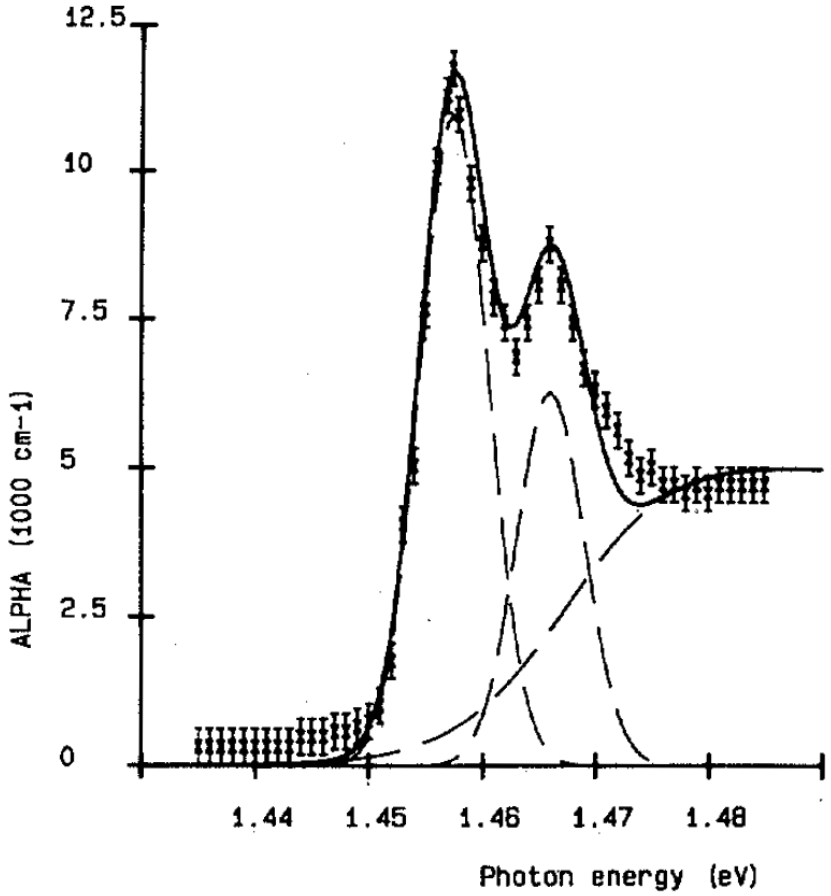

Figure 2.17: Absorption coefficient of GaAs/AlGaAs quantum well structures [89]. The first two excitonic states can be seen as two Gaussian distributions (dashed curves), while conventional absorption dominates at higher energies. The crosses correspond to experimental data, the solid line is an empirical fit.

the conduction band edge E_c. A thermalization process will then follow where the electron loses its energy through collisions and electron-phonon interactions, until it has energy E_c. Similarly, a hole generated below the valence band, will thermalize until it has energy E_v.

As stated in section 2.4.2, the duration of thermalization is on the order of hundreds of femtoseconds, while the lifetime of an electron in the conduction band is on the nanosecond-scale. Since thermalization is $\sim 10^4$ times faster than the recombination process, it is virtually instantaneous, and most electrons will recombine from the conduction band edge, E_c.

Due to the existence of excitons, doping and defects, electrons will also deexcite from levels within the bandgap, causing emission of photons with energy $\hbar\omega < E_g$.

When dopant atoms introduce energy levels close to the conduction band and valence band, they are called *shallow levels*, because they lie close to their respective bands. Levels that lie close to the middle of the bandgap are called *deep levels*. These are often caused by unwanted impurity atoms. Shallow levels can cause extra emission peaks close to the natural emission of the sample. Deep levels can introduce non-radiative paths for the electrons, thus lowering emission.

As discussed in section 2.4.5, several emission lines can occur due to excitons, depending on laser power [69] [90]. Since bound excitons saturate relatively quickly, the emission peaks have sublinear dependence on laser power, and are not visible at higher excitation. Free excitons have linear dependence on laser power, and are therefore usually present for pure materials. Biexcitons have superlinear laser power dependence. Their emission energy is slightly below that of free excitons. What type of excitons are present in a material, can be determined by integrating the intensity of a peak, and plotting its dependence on laser power, as in figure 2.18.

Thermalization results in a sharp peak in the emission spectrum at $E \approx E_g$. From excitons and defects some smaller peaks appear for $E < E_g$. This can be seen in figure 2.19.

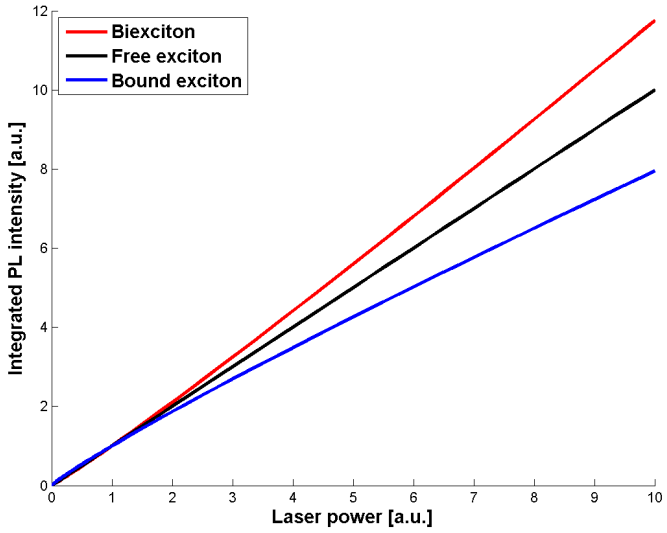

Figure 2.18: Illustration of the integrated intensity of excitonic peaks. This method is used to distinguish from the three excitonic types, **free excitons**, **bound excitons** and **biexcitons**. Note that free excitons have linear dependence on laser power, whereas biexcitons and bound excitons have superlinear and sublinear dependence, respectively.

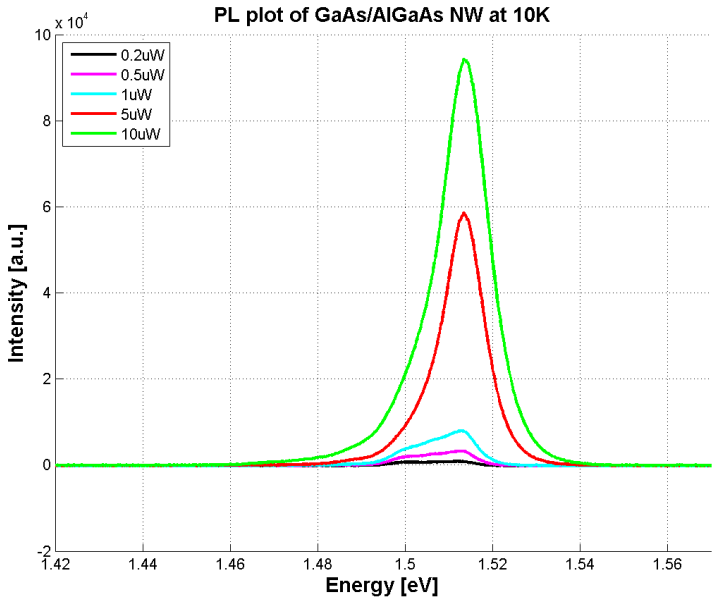

Figure 2.19: Emission spectrum for GaAs/AlGaAs NW, measured at $10K$, at different laser excitation powers. At lower excitation power several peaks are visible, this can be attributed to excitonic levels or crystal phase defect transitions between ZB and WZ segments (type-II transition).

2.7.3 Polarization-resolved photoluminescence

To understand *polarization-resolved photoluminescence* (PRPL), the concept of *polarization* needs to be clear. For monochromatic light in free space, the wave vector, $\mathbf{k}$, the electric field vector, $\mathbf{E}$, and the magnetic field vector, $\mathbf{B}$, forms a right-handed orthogonal triplet. It is the electric field vector, $\mathbf{E}(\mathbf{r}, t)$, that determines the polarization of light at a fixed position, $\mathbf{r}$, at time, t [91]. $\mathbf{E}$ oscillates in both amplitude and direction, and it is the direction of oscillation that determines the polarization direction.

For a monochromatic plane wave traveling in the z direction, the electric field lies in the $x - y$ plane and is described by

$$\mathbf{E}(z, t) = Re\left\{\mathbf{A}e^{i(kz-\omega t)}\right\}, \tag{2.31}$$

where $\mathbf{A} = A_x\hat{\mathbf{x}} + A_y\hat{\mathbf{y}}$, A_x and A_y being complex numbers on the form $A_x = a_x e^{i\varphi_x}$ and $A_y = a_y e^{i\varphi_y}$. The φ-components are the phases of the wave. The polarization of this wave is described by tracing the endpoint of $\mathbf{E}$ through space as a function of time.

The field components of $\mathbf{E}$ are thus

$$\begin{aligned} E_x &= a_x \cos(kz - \omega t + \varphi_x), \\ E_y &= a_y \cos(kz - \omega t + \varphi_y), \\ E_z &= 0, \end{aligned} \tag{2.32}$$

and we see that E_x and E_y are periodic functions of $kz - \omega t$. They can therefore be combined to form the equation for an ellipse,

$$\left(\frac{E_x}{a_x}\right)^2 + \left(\frac{E_y}{a_y}\right)^2 - 2\left(\frac{E_x}{a_x}\right)\left(\frac{E_y}{a_y}\right)\cos\varphi = \sin^2\varphi, \tag{2.33}$$

where $\varphi = \varphi_y - \varphi_x$ is the phase difference between E_y and E_x.

Equation (2.33) is the most general description of polarization in a plane (here the $x - y$ plane), and is known as *elliptical polarization*. If either E_x, E_y or φ is equal to zero however, the light is *linearly polarized* in the direction of the nonzero

component. If $\varphi = \pi/2$ and $E_x = E_y$, the light is *circularly polarized*. The degree of linear polarization is expressed by

$$P = \frac{I_{max} - I_{min}}{I_{max} + I_{min}}, \tag{2.34}$$

where $I = |E|^2$ is the intensity. $P = 1$ means linear polarization, $P = 0$ means circular polarization.

Several properties of matter can be polarization dependent, these include light reflection, light absorption, light scattering and the refractive index (propagation velocity in matter) [91]. This makes PRPL a powerful characterization tool.

2.7.3.1 The Jones formalism

The *Jones formalism* is used for describing polarized light. The Jones vector is used to represent light and Jones matrices are used for optical elements such as waveplates, lenses, mirrors, etc. Applying this formalism to the complex quantities from equation (2.31) gives

$$\mathbf{E} = \begin{bmatrix} E_x \\ E_y \end{bmatrix} = \begin{bmatrix} E_{0x} e^{i(kz - \omega t + \varphi_x)} \\ E_{0y} e^{i(kz - \omega t + \varphi_y)} \end{bmatrix} = \begin{bmatrix} E_{0x} e^{i\varphi_x} \\ E_{0y} e^{i\varphi_y} \end{bmatrix} e^{i(kx - \omega t)} = \mathbf{J} e^{i(kx - \omega t)}, \tag{2.35}$$

where $\mathbf{J}$ is the Jones vector, which represents the relative amplitude and phase of the electric field [91].

The Jones matrices are operators that act on the Jones vectors, thus affecting the polarization. When light interacts with an optical element, the resulting light is expressed as a product of the Jones matrix of the optical element and the Jones vector of the incident light,

$$\mathbf{J}_{out} = \hat{O} \mathbf{J}_{in}. \tag{2.36}$$

For a specific sample, the Jones matrix contains information on the refractive index of the sample, which again holds information on its composition.

In ellipsometry, *polarizer-compensator-sample-analyzer* (PCSA) is a common technique to determine the Jones matrix of a sample. In this method, a linear polarizer (P) is first used to linearly polarize the light. Secondly, a waveplate (for example $\lambda/4$ or $\lambda/2$) is used as a compensator (C) to make the light elliptically

polarized. The light is then reflected off the sample (S), passed to an analyzer (A) and into a detector, such as a CCD camera. The polarizer and compensator are oriented in such a way that the light reflected off the sample is linearly polarized. This gives destructive interference with the analyzer, resulting in a minimum signal to the detector. The angles of P, C and A required for complete destructive interference, the *null condition*, hold information on the optical properties of the sample.

2.7.4 Time-resolved photoluminescence

Time-resolved photoluminescence (TRPL) is a form of PL where short laser pulses, of pico- or femtosecond scale, are used to excite the sample. The emission intensity of the sample is then measured as a function of time, to determine how long electron-hole pairs stay in an excited state, the *carrier lifetime*. For pure materials at low temperature, recombination of electrons and holes happens as decay of excitons, and the measured lifetime will actually be the *exciton lifetime*. For TRPL it is very important that the system has enough time to relax before the next laser pulse arrives, which is normally on the nano- to microsecond scale [51].

The lifetime of a charge carrier in an excited state is dependent on the number of available transitions. For electrons deexciting from the conduction band in a perfectly pure semiconductor, this rate would be $W_{c\to v}$, as given by Fermi's Golden Rule (Eq. (2.30)). In real materials, however, there are defects and trapping levels that introduce alternative paths for the electrons, thus increasing the transition rate. Although some measured lifetimes will be exciton lifetimes, the general derivation is the same.

To find an expression for the electron-hole pair lifetime, the system is assumed to have a discrete number of available states. This is a valid assumption, since thermalization of electrons to the bottom of the conduction band (and holes to the top of the valence band) happens a lot faster than deexcitation. This results in two available states, in addition to states introduced by defects and impurities.

Let $N(t)$ be the number of electrons excited to the conduction band at a time

t. The expected change in N in the interval $(t, t+dt)$, is then given by

$$dN(t) = -N(t) \sum_m w_{n\to m} dt, \tag{2.37}$$

where $w_{n\to m}$ is the transition rate from a state n to m, n having higher energy than m [92]. This is a differential equation with solution

$$N(t) = N(0)e^{-t/\tau_n}, \tag{2.38}$$

$$\tau_n = \frac{1}{\sum_m w_{n\to m}}. \tag{2.39}$$

The lifetime, τ_n, is defined as the time it takes for the probability of finding an electron in state n, to be lowered to $1/e \approx 0.37$.

The main conclusion to be drawn from equation (2.38) is that the decay of electrons and holes is exponential. The measured lifetime will be that of electron-hole pairs recombining, so the number of minority carriers is the limiting factor. Since defects and impurities introduce alternative recombination pathways for electrons and holes, the number of m's increase, and the lifetime τ_n, decreases.

By finding the carrier lifetime, TRPL spectroscopy can provide information regarding transport dynamics, surface recombination [51], hot-carrier cooling rates and electron-hole recombination rates [93], etc. Radiative transition rates are important for all photonic devices, and hot-carrier behavior has importance for fast semiconductor devices [51].

3 Experimental

This section will give the general outline of the instrumental setup, the growth parameters and the methods used to obtain measurements and analyze the results.

3.1 Sample growth parameters

In this section the growth parameters used for growing the NWs evaluated in this thesis, are presented. The NWs were grown by the SC technique using a Varian Gen II Modular MBE system. The NWs were grown on fresh native oxide covered Si(111) substrates. The GaAs/AlGaAs core-shell NW growth was initiated by opening the shutters of Ga and As cells simultaneously. Four different samples were grown for analysis, they will be labeled sample δ, ψ, σ and α.

For samples δ, ψ and σ, the GaAs cores were grown with three different V/III ratios to see their impact on the optical properties. The Ga rate was kept constant at $0.7ML/s$ (monolayers per second) for all the samples and the growth temperature was $640°C$, as measured by a pyrometer. The As_4 fluxes for the samples were $5.5 \cdot 10^{-6}$ (δ), $7.5 \cdot 10^{-6}$ (ψ) and $9.5 \cdot 10^{-6}$ (σ) Torr. They were grown for 30, 25 and 20 min, respectively, in order to achieve similar NW length for each sample. These fluxes correspond to V/III ratios (P_{As}/P_{Ga}) of 17.4, 23.8 and 30.1, respectively. The shell growth conditions were kept identical for all three samples. To form the core-shell structure after the core growth, the Ga droplets were consumed into NW. For this purpose, the Ga shutter was closed and the As_4 flux was set to $1.3 \cdot 10^{-5}$ Torr for 10 min. After that, the substrate temperature was reduced to $460°C$. Then the $Al_xGa_{x-1}As$ (nominal Al content, $x = 33\%$) shell was grown with Ga rate $0.1ML/s$, Al rate $0.1ML/s$ and As_4 flux $1.5 \cdot 10^{-5}$ Torr for 30 min. The AlGaAs shell was further covered by growing a GaAs cap for 20 min to prevent oxidation.

Sample α was grown in a different set as the other three. This sample is included because it was the most promising candidate for optoelectronic applications from a previous project thesis [42]. It was grown at $0.3ML/s$, with a growth temperature of $640°C$. The As_4 ratio was adjusted to obtain non-tapered homogeneous GaAs

NWs and set at $2.8 \cdot 10^{-6}$ Torr. The growth duration was 120 min. After the core growth, the $Al_xGa_{x-1}As$ shell and GaAs cap were grown with similar conditions as mentioned above for the first set of samples, except that the nominal Al content used here, was $x = 50\%$.

The most important parameter for the evaluation, the V/III ratio, is summarized for all four samples in table 3.1.

Sample	V/III ratio $[P_{As}/P_{Ga}]$
δ	17.4
ψ	23.8
σ	30.1
α	20.0

Table 3.1: Table of V/III ratio, measured as As flux (units of pressure) divided by Ga flux. The four samples analyzed in this thesis are included.

3.2 Optical setup

Here follows a an explanation of the setup, as well as some information on the components in the schematic. A number of mirrors and lenses are used to guide and focus the light from the laser source to the sample, then into the spectrometer. The path of the beam is shown in the schematic overview of figure 3.1, with corresponding numbered explanations in this section. The schematic shows that two different lasers can be used for excitation of the sample, and two different spectrometers for measuring the emission. Figure 3.2 is a digital photo of all components.

I. A laser beam of wavelength $532nm$ is created by a Nd:YVO solid state laser (Sec. 3.2.2). This is used to excite the sample.

II. A grating, two lenses and one pinhole placed at their common focus, are used together to improve the monochromaticity of the beam. Termed "monochromator" in figure 3.1.

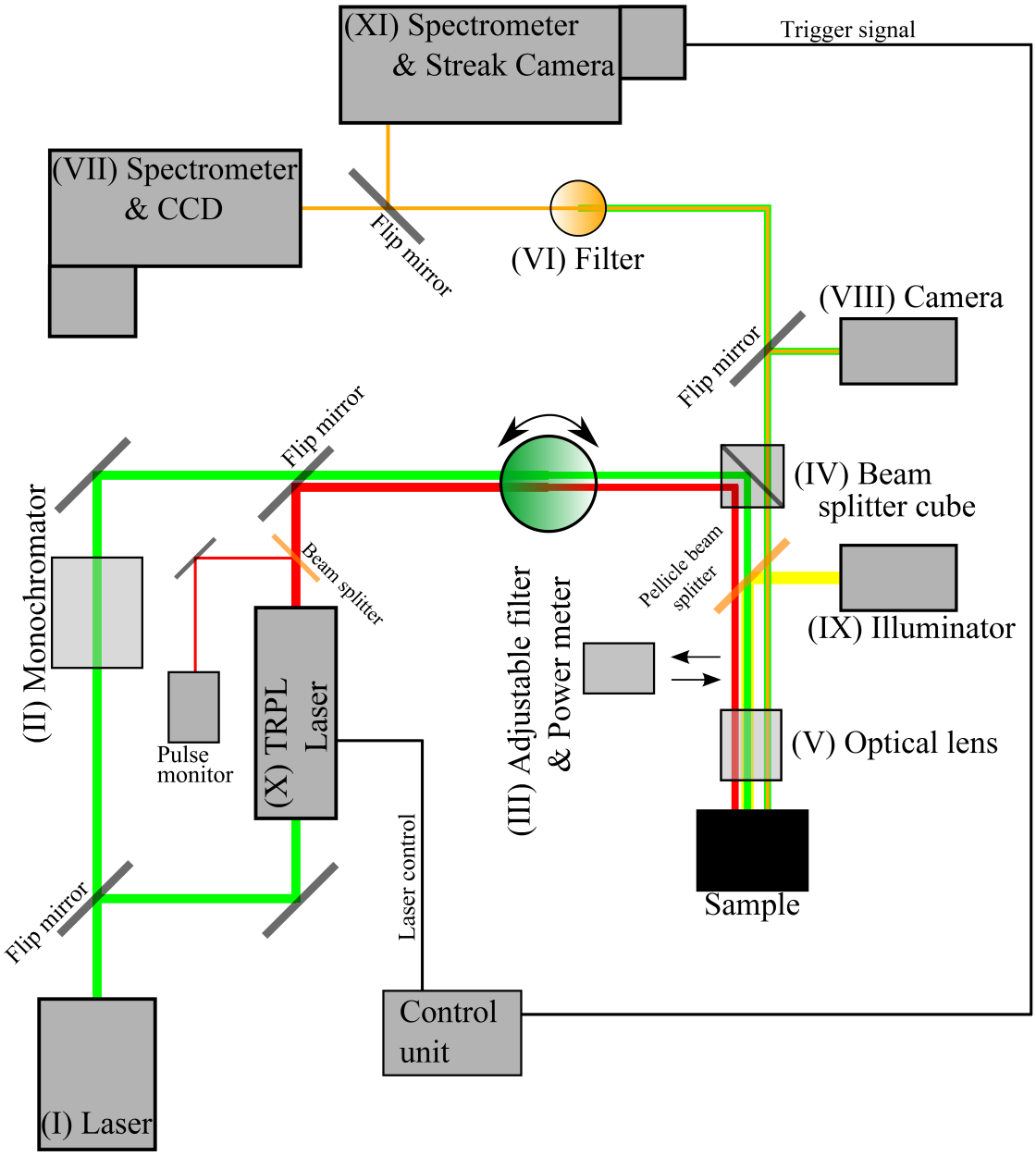

Figure 3.1: Schematic overview of the optical setup used for power dependent PL and TRPL experiments. The green line represents the light coming from the excitation laser source (I). The red line represents the pulsating excitation light used in TRPL measurements, coming from laser source (X). The orange line represents the emitted PL signal coming from the sample. The yellow line represent the illumination light (IX), which is directed into the optical camera (VIII) for navigation.

III. An adjustable filter used to tune the excitation power of the laser and a retractable power meter used to measure it.

IV. A beam splitter cube is used to reflect part of the laser light towards the sample. The light is also transmitted through a pellicle beam splitter, used for guiding illumination light to the sample. The reflection:transmission ratio of the cube- and pellicle beam splitters are $R50 : T50$ [94] and $R8 : T92$ [95], respectively.

V. A focusing lens (Sec. 3.2.1) is used to focus the laser light onto single NWs on the sample.

VI. The emitted PL signal is transmitted through the pellicle and beam splitter cube, then through another filter positioned in front of the spectrometer. The filter is used to remove the unwanted laser peak at $532nm$, which is significantly stronger than the emitted signal from the sample.

VII. The emitted signal ends up in a spectrometer with a CCD camera (Sec. 3.2.3), which is used to convert the photonic signal into an electric signal, used for analysis.

VIII. To observe the sample and navigate the laser light onto the NWs, a flip mirror can be used to guide the beam into a Watec Digital color camera (WAT-202D) connected to a TV screen.

IX. The pellicle beam splitter is is used to guide adjustable white-light illumination to the sample, when observing on the TV screen.

X. By flipping a mirror, the laser beam from (I) can be used to pump a mode-locked Ti:Sa laser (Sec. 3.2.5.1). This laser produces a pulsating IR beam of adjustable wavelength, used for time-resolved measurements. A small part of the pulsating laser goes to a pulse monitor.

XI. Another flip mirror is used to direct the pulsating PL signal from the sample into a different spectrometer. The attached streak camera measures the

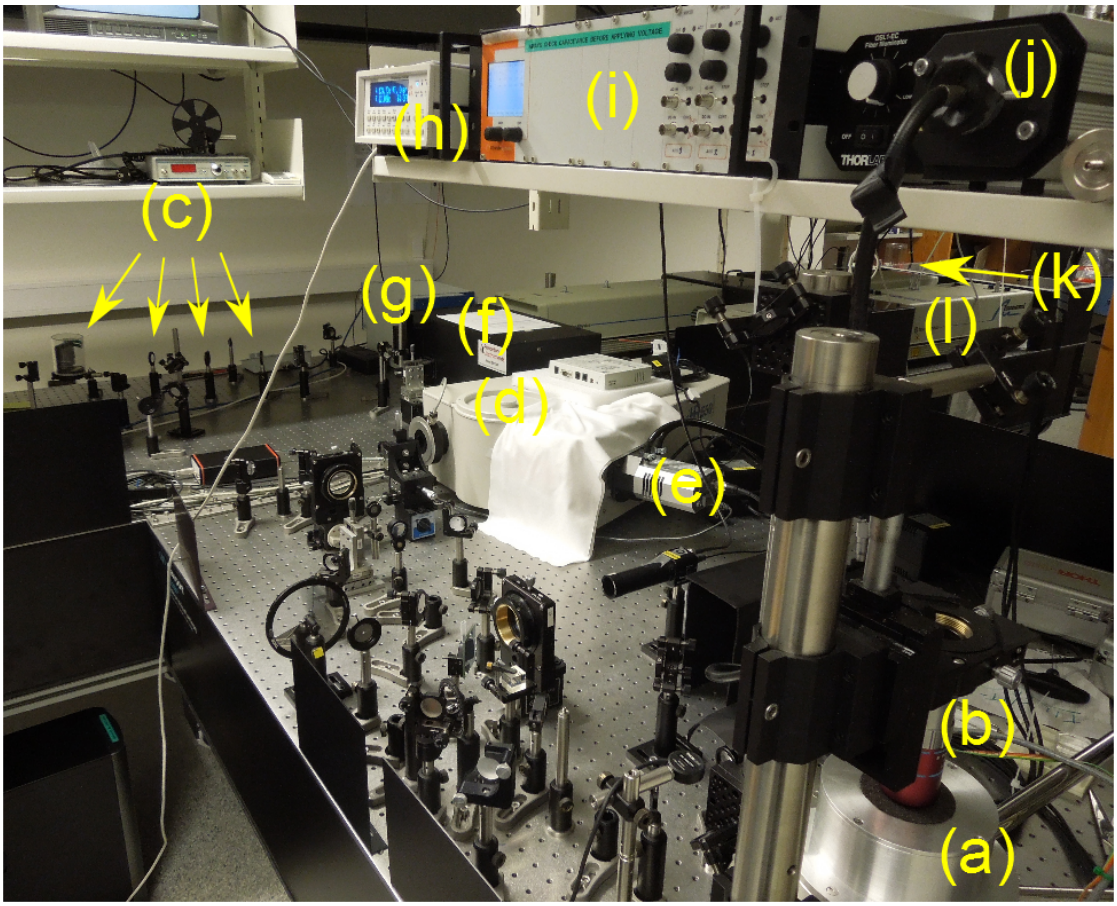

Figure 3.2: A digital photo of the experimental setup. (a) Cryostat; (b) focusing lens; (c) monochromator; (d) spectrometer; (e) CCD; (f) spectrometer TRPL; (g) streak camera; (h) sample heater; (i) piezo controller; (j) illumination source; (k) laser source; (l) pulsating laser TRPL.

variation of the PL signal with time (Sec. 3.2.5.2). The signal from the streak camera is used as a trigger in a feedback loop to the laser control unit.

Now follows a more detailed description of each instrument used.

3.2.1 Cryostat

A Janis ST-500 [96] was used for the measurements. It is a continuous flow optical cryostat, and can do experiments with temperatures ranging from $4K$ to $290K$. It

is cooled by a continuous flow of cryogenic liquid, transferred from a tank through a high efficiency super insulated line. In our case, liquid Helium-4 ($4.2K$) was used to cool the chamber. The sample, which is positioned on a copper sample mount, the *cold finger*, is thus cooled. A thermometer is connected to the cold finger, and measures the sample temperature. To navigate the sample, the finger sits on a 3D piezo-stage.

The objective used to focus the laser is a Mitutoyo infinity-corrected and near infrared (NIR) optimized lens, with a numerical aperture, $NA = 0.65$, and 50x magnification. The focus spot is $\sim 1.5\mu m$, small enough to excite single NWs.

To create the desired vacuum of $\sim 5 \cdot 10^{-5} mbar$ inside the sample chamber, a Pfeiffer Vacuum Technology AG turbo pump was used, model HiCube 80 Eco [97]. This is done to avoid icing from air moisture at low temperatures.

3.2.2 Laser

The main laser used to excite the samples (except for time-resolved PL) was a Spectra-Physics Milennia^{TM} Pro s-Series diode pumped, frequency-doubled continuous wave (CW) solid state laser operating at a wavelength of $532nm$ (green light) [98]. It is pumped by a LED array kept at $18°C$.

A wavelength of $532nm$ corresponds to a photon energy of $2.3308eV$, much larger than E_g for GaAs (ZB and WZ). A high photon energy results in a higher number of allowed transitions into the conduction band, and thus increases the rate of absorption (in accordance with Eq. (2.29)).

The maximum laser output power is $6W$, but for these measurements a power of $0.23W$ was used, and a number of grey filters to lower the intensity further, to avoid damaging the NWs.

3.2.3 Spectrometer and CCD

To disperse the PL spectra, a Horiba Jobin Yvon iHR500 spectrometer [99] was used. The photon beam is passed to a reflection grating that distributes the photons spatially, according to photon energy. They are then directed into one of two attached charge coupled device (CCD) cameras.

To detect the photons transmitted through the spectrometer, a CCD camera was used. The camera is a Thermo-Electrically cooled EMCCD, Andor iDus InGaAs 1.7 detector array, and works for spectroscopy applications from $600nm$ to $1.7\mu m$ [100]. It has optimal signal-to-noise ratio at $-90°C$. For these experiments it was operated at $-70°C$.

The spectrometer and the CCD camera were operated through the Laboratory Virtual Instrumentation Engineering Workbench (LabVIEW) [101] software interface (Sec. 3.3.5).

3.2.4 Polarization-resolved photoluminescence setup

When conducting PRPL measurements, two different setups were used. One approach was to excite the sample with light of variable *linear polarization*, we will call this *excitation polarization*. This can be used to determine the angle of the NW compared to the polarization of the waveplates. The other approach was to excite the sample with *circularly polarized* light, causing the NWs to emit linearly polarized light, which is then analyzed. This will be called *emission polarization*.

Note that the pellicle beam splitter, seen in figure 3.1, was removed for PRPL experiments. This was because the transmission through the beam splitter is polarization dependent [95].

3.2.4.1 Excitation polarization setup

Figure 3.3(i) shows the setup. The laser excitation light goes through a polarizer to ensure linearly polarized light, which is always set to 90°, perpendicular to the optical table. The $\lambda/2$-plate is adjusted to create the desired linear polarization angle, C (Sec. 2.7.3). The emitted PL signal goes through a $\lambda/4$-plate, used to maximize the signal. It then goes through an analyzer set to 90°, polarizing the signal along the grooves of the spectrometer grating.

3.2.4.2 Emission polarization setup

Figure 3.3(ii) shows the setup. The polarizer is used in the same way as in the excitation polarization scheme. Since the beam splitter cube changes the polarization

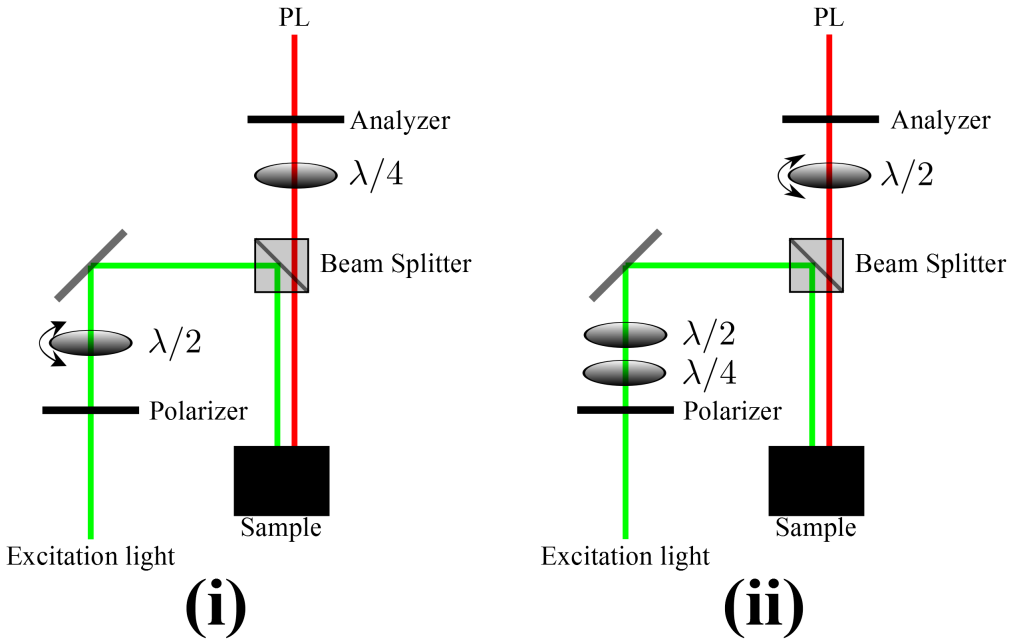

Figure 3.3: Simplified overview of the optical setup used for PRPL measurements. (i) setup used for excitation polarization; (ii) setup used for emission polarization.

of the light, a $\lambda/2$- and a $\lambda/4$-plate are used to prepare an elliptical polarization, which upon reflection in the beam splitter becomes circular. The sample should emit linearly polarized light after being excited circularly. An adjustable $\lambda/2$-plate is positioned in front of the analyzer, which is fixed at 90°, as in the excitation polarization setup.

3.2.5 Time-resolved photoluminescence setup

As described, TRPL can be done by small changes in the setup, namely flipping mirrors (Fig. 3.1). This setup is very similar to the power dependent PL setup, the main difference being that another laser is used for excitation, another spectrometer, and a streak camera instead of the CCD.

3.2.5.1 Pulse laser

The pulse laser used for TRPL measurements was a Spectra-Physics Tsunami 3960-10HP Mode-locked Ti:sapphire Laser [102]. The solid state CW laser from

section 3.2.2 was used to pump the pulse laser. It features a wavelength range from 750 to 950nm, regenerative mode locking, laser pulses of 0.24ps or 2ps and high power up to 10W.

To measure the pulse width of the laser, a glass plate was used to guide a 10% of the pulse into a Spectra-Physics Pulse Monitor connected to a Spectra-Physics Autocorrelator PulseScout. Also, the streak camera used to measure the signal (Sec. 3.2.5.2) was connected to the laser control unit, to make sure the sample emission from one pulse is done, before the next excitation pulse is emitted.

3.2.5.2 Spectrometer and streak camera

Through the combined use of a spectrometer and a streak camera, both spectral resolution and temporal decay time of the PL signal can be obtained. The spectrometer used to disperse the PL spectrum was a Princeton Instruments Acton SP2500 spectrometer [103].

The selected photons were then passed into a Optronics Optoscope SC10 streak camera [104]. It can be used to analyze visible light and ultraviolet (UV) light down to 200nm. The temporal resolution of the camera is $\sim 2ps$. It was operated through the OptoAnalyse Software [105] which was also used to obtain images.

The working principles of the streak camera is illustrated in figure 3.4. The photons dispersed in the spectrometer are horizontally distributed before the streak camera entrance slit. A photocathode converts the light to electrons and the first electrons trigger a perpendicular sweep voltage, deflecting them vertically. Since the voltage changes, electrons arriving at different times are deflected at different angles. They then enter a multichannel plate (MCP) that multiplies the electronic signal. The gain ratio is typically $10^5 - 10^6$ [51]. The beam then hits a phosphor screen that converts the electrons back to photons. This light signal is then analyzed by a CCD camera.

3.3 Measurements

To detach NWs from the Si surface on which they were grown, a diamond scriber was used. Isopropanol was then applied, and a grid placed on top. A substantial

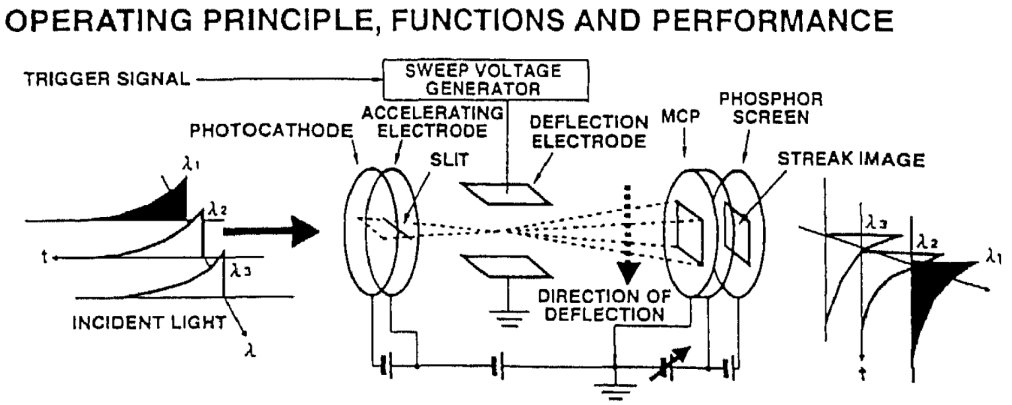

Figure 3.4: Schematic illustration of a streak camera [51].

amount of NWs were attached to the grid after the isopropanol had dried. The grid used was a Cu-grid with windows of $\sim 7x7\mu m$ (Fig. 3.5(i)), with a few monolayers of graphene on top. After adding the NWs, another Cu grid was added, with numbered windows of $\sim 100x100\mu m$ (Fig. 3.5(ii)). The numbering was helpful for locating NWs on the sample.

After depositing the NWs on the grids, *scanning electron microscope* (SEM) was used to pick which NWs to study. The NWs chosen for further examination were all deposited directly on the graphene, as seen in figure 3.5(i). The SEM mapping was necessary to identify the exact positions of the NWs on the grid, and to make sure measurements were done on single NWs (not clusters), which was not distinguishable in the PL setup. This setup enabled for easy navigation and localization of the NWs in the PL setup.

Since the preselected NWs were deposited directly on graphene, characterized by high resolution transmission electron microscope (HR-TEM) is possible. With a thickness of a few monolayers and high conductivity, graphene is an optimal substrate for HR-TEM. This can give information about the crystal structure of the samples, which is useful for analyzing the results. For this work, however, HR-TEM was not done.

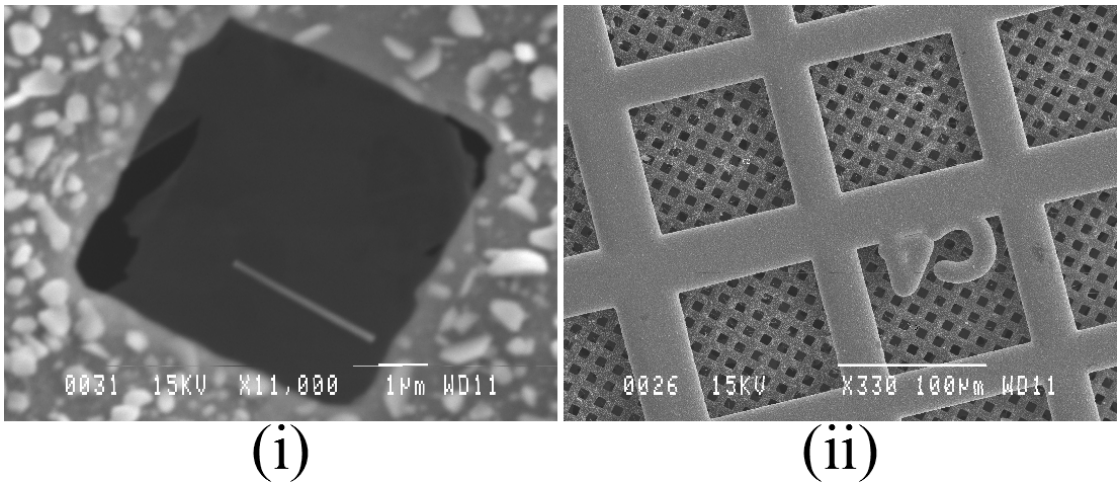

Figure 3.5: (i) x11,000 SEM image of a NW deposited directly on graphene, inside a small grid window; (ii) x330 SEM image of larger, numbered grid windows. These images were used for locating preselected NWs during PL.

3.3.1 Excitation power and temperature dependence measurements

Measurements were done at different laser excitation power. Power was regulated by the use of an adjustable filter and measured by a power meter (Fig. 3.1(III)).

Temperature dependent measurements were done for fixed temperatures from $10 - 16K$, up to room temperature ($293K$). Liquid helium (He) of temperature $4.2K$ was used as a cryogenic cooling liquid. To adjust the temperature, the flow of He was controlled while a heating ring inside the chamber was used to heat the cold finger, i.e. the sample.

3.3.2 Excitation polarization measurements

Since the bandgap is much smaller than the excitation energy, the number of allowed transitions is large, and selection rules becomes negligible. Light absorption will depend on the angle between the polarized beam and the NW, due to dielectric mismatch effects [106]. The result is a minimum in absorption, and thus emission, when the light is polarized perpendicular to the NW axis, and a maximum when they are parallel.

Now a consideration of a PCSA setup for excitation polarization dependence,

by using the Jones formalism. For a review on PCSA and the Jones formalism, see section 2.7.3. A beam was passed through a polarizer, polarizing it at 90°, i.e. perpendicular to the optical table, defined as the y-direction. The light has Jones vector

$$\mathbf{E}_{in} = \begin{bmatrix} 0 \\ 1 \end{bmatrix}. \tag{3.1}$$

By placing a $\lambda/2$-plate after the polarizer, the light reaching the sample is expressed by

$$\mathbf{E}_{sample} = \hat{R}(-C)\hat{C}\hat{R}(C) \begin{bmatrix} 0 \\ 1 \end{bmatrix}, \tag{3.2}$$

$$\hat{R}(C) = \begin{bmatrix} \cos C & \sin C \\ -\sin C & \cos C \end{bmatrix}, \quad \hat{C} = \begin{bmatrix} 1 & 0 \\ 0 & -1 \end{bmatrix},$$

where $\hat{R}$ is the rotation matrix, $\hat{C}$ is the Jones matrix for a $\lambda/2$-plate and C is the angle of the $\lambda/2$-plate. Using matrix calculations, this equates to

$$\mathbf{E}_{sample} = \begin{bmatrix} E_{s,x} \\ E_{s,y} \end{bmatrix} = \begin{bmatrix} \sin(2C) \\ -\cos(2C) \end{bmatrix}. \tag{3.3}$$

Next it is assumed that the sample is a NW, lying with an angle α to the x-axis (parallel to the optical table). The components of $\mathbf{E}_{sample}$ hitting the NW is then split into a parallel and perpendicular component, $E_{s\parallel NW}$ and $E_{s\perp NW}$. The components are determined by

$$\begin{bmatrix} E_{s\parallel NW} \\ E_{s\perp NW} \end{bmatrix} = \begin{bmatrix} \cos\alpha & \sin\alpha \\ -\sin\alpha & \cos\alpha \end{bmatrix} \begin{bmatrix} \sin(2C) \\ -\cos(2C) \end{bmatrix} = \begin{bmatrix} \sin(2C-\alpha) \\ -\cos(2C-\alpha) \end{bmatrix}. \tag{3.4}$$

Due to the lattice mismatch effect, absorption of light perpendicular to the sample is neglected. Since emission is proportional to absorption, the emitted PL intensity is therefore proportional to $E_{s\parallel NW}$

$$I_{PL} \sim \left|E_{s\parallel NW}\right|^2 = \sin^2(2C-\alpha). \tag{3.5}$$

This was used to determine the angle of the NW to the predetermined x-axis, which is parallel to the optical table.

The excitation polarization was regulated by rotating the adjustable $\lambda/2$-plate seen in figure 3.3(i). Measurements were taken for $C \in [0°; 100°]$, with intervals of 5°. Emission is periodic for every 90°, but the extra measurements were taken to allow some overlap, to ensure no changes in alignment had occurred. This method yields 21 spectra, and each peak from each spectra was curve fitted (Sec 3.3.6) and all plotted together. The resulting plot was again curve fitted to equation (3.5) to determine the orientation of the NW with respect to the x-axis, α.

3.3.3 Emission polarization measurements

For emission polarization experiments the sample was excited by circularly polarized light. The sample emitted linearly polarized light, which was analyzed to determine the polarization dependence on the PL intensity.

Now considered through the Jones formalism (Sec. 2.7.3). The beam hitting the sample is circularly polarized, while the polarization of the beam leaving the sample, $\mathbf{E}_{PL}$, is unknown

$$\mathbf{E}_{PL} = \begin{bmatrix} A \\ B \end{bmatrix}. \tag{3.6}$$

By placing a $\lambda/2$-plate after the sample, the light reaching the analyzer will be

$$\mathbf{E}_{analyzer} = \hat{R}(-C)\hat{C}\hat{R}(C) \begin{bmatrix} A \\ B \end{bmatrix}, \tag{3.7}$$

where $\hat{R}(C)$ and $\hat{C}$ are defined as in equation (3.2). This equates to

$$\mathbf{E}_{analyzer} = \begin{bmatrix} \cos(2C) & \sin(2C) \\ \sin(2C) & -\cos(2C) \end{bmatrix} \begin{bmatrix} A \\ B \end{bmatrix}. \tag{3.8}$$

This beam is passed through the analyzer, with Jones matrix $\hat{A}$, and the beam reaching the spectrometer is

$$\begin{aligned} \mathbf{E}_{spectrometer} = \hat{A}\mathbf{E}_{analyzer} &= \begin{bmatrix} 0 & 0 \\ 0 & 1 \end{bmatrix} \begin{bmatrix} \cos(2C) & \sin(2C) \\ \sin(2C) & -\cos(2C) \end{bmatrix} \begin{bmatrix} A \\ B \end{bmatrix} \\ &= \begin{bmatrix} 0 & 0 \\ \sin(2C) & -\cos(2C) \end{bmatrix} \begin{bmatrix} A \\ B \end{bmatrix}. \end{aligned} \tag{3.9}$$

Then, assuming that the emitted PL signal, $\mathbf{E}_{PL}$ makes an angle β with the x-axis, we get

$$\begin{bmatrix} A \\ B \end{bmatrix} = \begin{bmatrix} \cos\beta \\ \sin\beta \end{bmatrix}, \tag{3.10}$$

thus giving

$$\mathbf{E}_{spectrometer} = \begin{bmatrix} 0 & 0 \\ \sin(2C) & -\cos(2C) \end{bmatrix} \begin{bmatrix} \cos\beta \\ \sin\beta \end{bmatrix} = \begin{bmatrix} 0 \\ \sin(2C-\beta) \end{bmatrix}. \tag{3.11}$$

The result is similar as for excitation polarization, the intensity of the signal being

$$I_{spectrometer} \sim |E_{PL}|^2 = \sin^2(2C-\beta). \tag{3.12}$$

This result was used to obtain information on the Jones matrix of the sample.

For emission polarization, when the sample was excited with circularly polarized light, the polarization was regulated by rotating the $\lambda/2$-plate seen in figure 3.3(ii), now positioned *after* the sample. The polarization of the waveplate was varied for $C \in [0°; 100°]$, with intervals of 5°, as before. The resulting data was processed in almost the exact same way. The only difference being that excitation polarization analysis was done beforehand, so the angle of the NW, α, was now known. α was added to the value of C used for the adjustable $\lambda/2$-plate. This gave the linear polarization of the emitted PL signal, with respect to the NW. Using selection rules, this information can be used to get knowledge on the optical properties and crystal structure of the NW.

3.3.4 Time-resolved photoluminescence data processing

The TRPL data output from the streak camera is a three dimensional dataset, resolved for emission energy (ϵ), time (t) and intensity (I) (Fig. 3.6). Analysis was done by plotting the data in MATLAB, then choosing what region of emission energy to be used $\epsilon \in [\epsilon_{lower}; \epsilon_{upper}]$. The intensity data was then summed for these energies,

$$I(t) = \sum_{\epsilon_{lower}}^{\epsilon_{upper}} I_\epsilon(t). \tag{3.13}$$

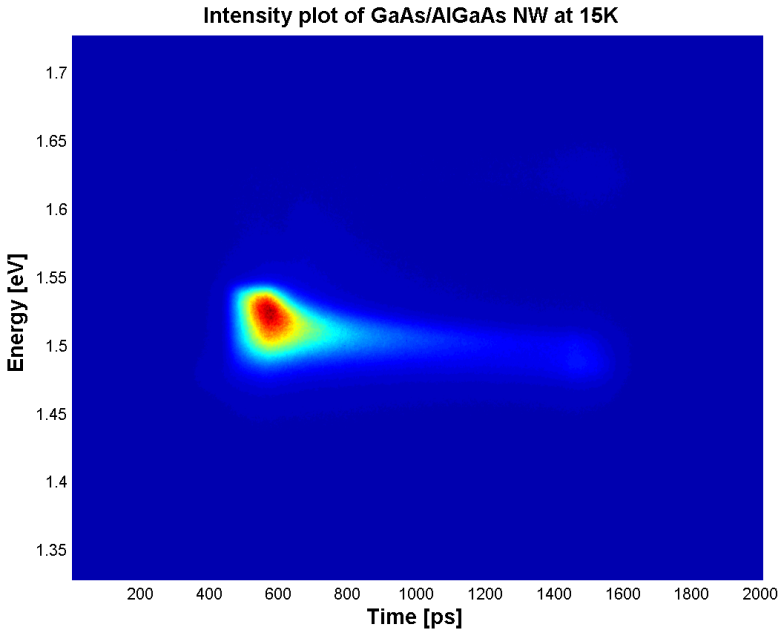

Figure 3.6: Plot of the streak camera output for TRPL measurement on GaAs/AlGaAs NW at $15K$. This type of plot was used to decide what emission energy interval to be used for further analysis.

The resulting dataset was used to make a two dimensional plot of intensity and time, as in figure 3.7. This plot shows the decay of the emitted signal, which was curve fitted to two exponential decay functions from equation (2.38). Two decay functions were used because there could be several recombination routes not possible to distinguish in energy, or there could be a change in the emission mechanism during the decay process.

3.3.5 Measurement parameters

The LabVIEW interface, used for all except TRPL measurements, enabled control of several measurement parameters. The *center wavelength* of the spectrometer was usually set to $830nm$, the equivalent of $1.495eV$, because this was the region where emission peaks were expected to occur.

The *exposure time* of the spectrometer was set in order to clearly distinguish the emission signal from the background noise. It was limited by overexposure of

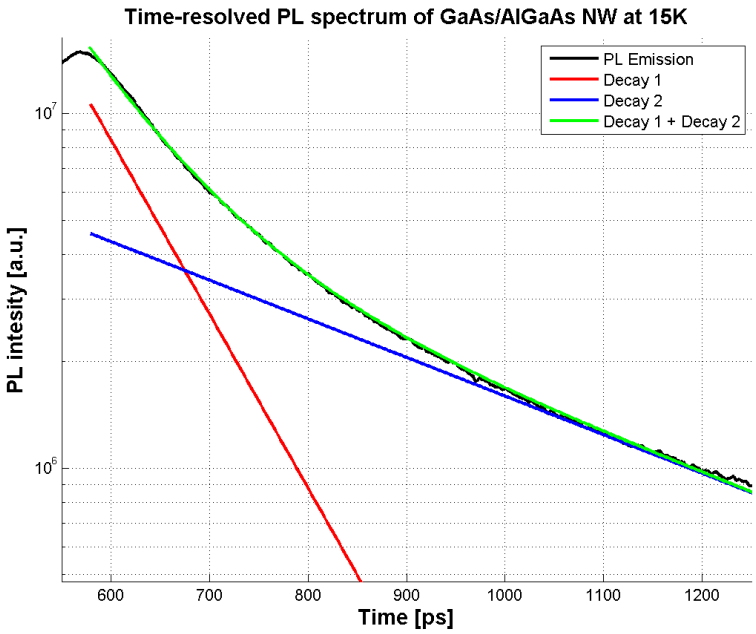

Figure 3.7: Time-resolved emission spectrum of GaAs/AlGaAs NW, measured at $15K$.

the CCD for higher power excitation, which can damage the equipment.

The *target front entrance* was set to $0.2mm$. Decreasing the entrance increases resolution, but decrease exposure strength. This can be compensated for by increasing the exposure time. The target grating was set to 300.

3.3.6 Data processing

The output data from LabVIEW was in .txt format. The files consisted of two columns of numbers, the first containing *wavelength* in nanometers $[nm]$, the second containing measured *emission intensity* in arbitrary units $[a.u.]$. The data was analyzed using MATLAB (version R2012b), a numerical computing software developed by MathWorks [107].

For each dataset of intensities, obtained with specific spectrometer and CCD settings, the corresponding dark spectrum was subtracted. Because the exposure time, t_{ex} of the measurements could differ, all intensities were multiplied by $\frac{10}{t_{ex}}$ (where $10s$ was the highest exposure time used), to ensure comparability of the

spectra. The wavelength data was corrected using calibrated values. See section 3.3.7 for information on dark spectrum and calibration.

Since the goal of the experiments was to analyze the optical properties of the NWs, the measured wavelengths were transformed to units of electron volts eV. The expression used was

$$E = \hbar\omega = \hbar\frac{c}{\lambda}, \tag{3.14}$$

which gives the energy in joule (J), while divided by the unity charge ($1.6 \cdot 10^{-19} C$) yields eV. This was done to simplify the discussion of results with respect to bandgap, exciton binding energy etc, all in eV.

3.3.6.1 Curve fitting

Most of the obtained spectra contained several emission peaks, superimposed on top of each other. Since the spectrometer and LabVIEW software measured total intensity, it was necessary to separate these peaks from one another. The total plot can be interpreted as overlapping Gaussian distributions, as is illustrated in figure 3.8. The plot was obtained by a method known as curve fitting, and was done in MATLAB through use of the least squares method [108].

3.3.7 Calibration and background noise

The emission spectra measured by the CCD were not necessarily correctly calibrated. Since a high energy resolution was required (exciton binding energy is on the order of meV), a correction of the measured results was necessary. This was achieved by leading the $532nm$ laser light into a Spectra-Physics 3900S CW tunable Ti:sapphire laser [109], then measuring the wavelength with a highly reliable Avantes high-resolution spectrometer, AvaSpec 3648 [110].

The center wavelength of the spectrometer was set at $830nm$. While the center wavelength was kept constant, a spectrum was measured with the laser output wavelength varied from the lower to the upper end of the scope of the spectrometer ($770nm - 900nm$). Knowing the exact wavelength of the intensity peak, and comparing with the measured result from the CCD, curve fitting was used to create a corrected relation between the measured and real wavelength. The result

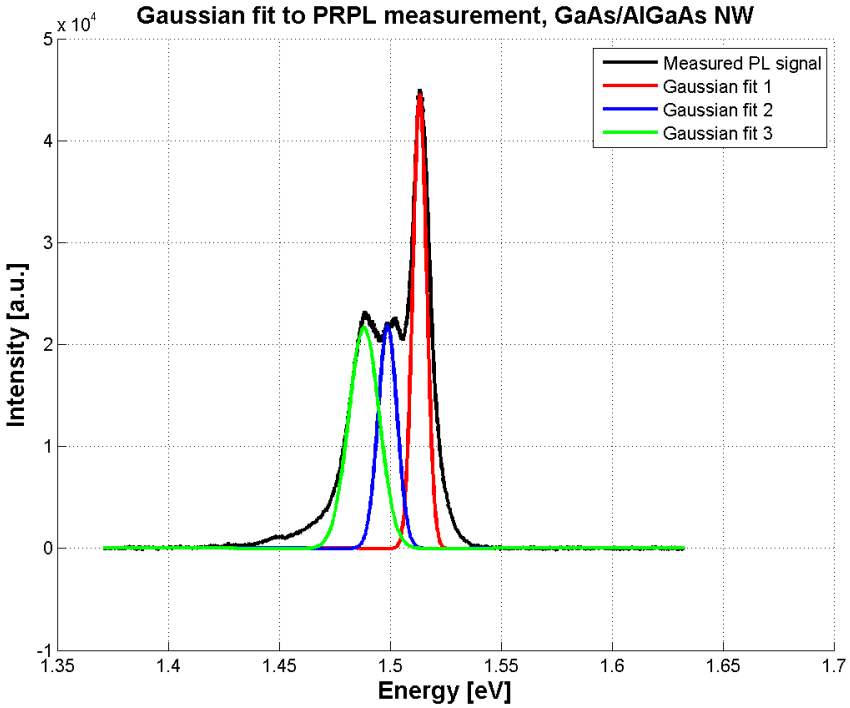

Figure 3.8: Least squares method used to curve fit three Gaussian distributions on one measured PL signal from a GaAs/AlGaAs NW, at $12K$.

being a close to linear polynomial function, taking the measured wavelength as argument and returning a new, corrected wavelength.

The CCD will always register background noise, distributed over all wavelengths. For longer exposure time, the magnitude of the background noise increases, and the noise can be larger than the PL signal for low laser excitation power. After each experiment it was therefore necessary to take one *dark spectrum* for every combination of measurement parameters used. This background noise was later subtracted from the obtained PL signal, to make sure only the emitted NW signal was analyzed.

4 Results

This section contains the results obtained from measurements by methods described in section 3. Measured values and plots are presented while differences and similarities are pointed out. The implications of the results are analyzed in section 5.

The main focus is on three samples, namely δ, ψ and σ, which were grown with different V/III ratios. Measurements were also done on sample α, which was the most promising sample from a previous project thesis [42]. α is used as a reference for the results obtained for the other three samples. Section 3.1 contains detailed growth parameters for the NWs, while the V/III ratios are repeated here:

Sample	V/III ratio $[P_{As}/P_{Ga}]$
δ	17.4
ψ	23.8
σ	30.1
α	20.0

Table 4.1: Table of V/III ratio, measured as As flux (units of pressure) divided by Ga flux. The four samples analyzed in this thesis are included.

The goal of this master thesis is to find the effect the V/III ratio has on optical and material properties of the NWs grown. Therefore, the collected data will be presented in sections according to the type of data, with every sample as a subsection. This is to illustrate the differences between the four samples, for every property measured.

For each of the four samples, 10-15 NWs had been preselected as candidates for measurement, through SEM, as described in section 3.3. After doing power dependent PL measurements on these NWs at low temperature ($10 - 16$K), 3-5 NWs were again selected based on the results. The criteria for being chosen was that the NWs showed strong PL emission, and preferably indications of a ZB GaAs exciton emission peak around $1.515eV$. On these NWs, further, more advanced measurements were done.

One NW will be presented for each sample, as a representation for that sample's properties. Plots and results from NWs not presented here can be found in the appendices, and are used for supporting the discussion.

4.1 PL intensity dependence on laser excitation power

Measurements were done of the *PL emission intensity* at at different *laser excitation power* (LP). The laser power was set by an adjustable grey filter and measured by a power meter (Sec. 3.3.1). The output text files were plotted in MATLAB. Background noise was accounted for, and a calibrated axis for emission energy data was used (Sec. 3.3.6).

Separate peaks in the emission spectrum are resolvable at LP down to $200nW$, and measurements are done for LP up to $70\mu W$. As mentioned, peaks emitting close to the ZB GaAs exciton level of $1.515eV$ are of special interest. By analyzing these peaks for varying LP and temperature (Sec. 4.2), the type of exciton binding in the NWs can be determined (Sec. 2.4.5 and 2.7.2.2).

Transitions emitting close to $1.515eV$ were curve fitted to Gaussians, and the total emission intensity originating from these peaks determined by integration to find the area under the curves. The integrated signal is plotted as a function of LP, then curve fitting to a function of the form

$$y = a \cdot LP^b. \tag{4.1}$$

From the value of b, is possible to determine if the peaks have sublinear- ($b < 1$), linear- ($b \approx 1$) or superlinear dependence ($b > 1$) on LP. This indicates the existence of bound excitons, free excitons or biexcitons, respectively.

4.1.1 Sample δ

Figure 4.1 shows the PL emission intensity of δ-NW14, measured at $14K$. There are no resolvable transitions around $1.515eV$, although there is some emission for high laser power ($LP > 30uW$). The observable peak is broad, indicating that many transitions are contributing to the signal. The strongest peak emits at $1.477eV$ at low temperature and $10\mu W$ laser power, but shifts for higher and lower LPs. This may be because different transitions dominate at different LPs. This plot was found to be representative of the NWs from sample δ, none of which emitted strongly at $1.515eV$.

Since no excitonic emission is observed, power dependence analysis on the emission was not conducted.

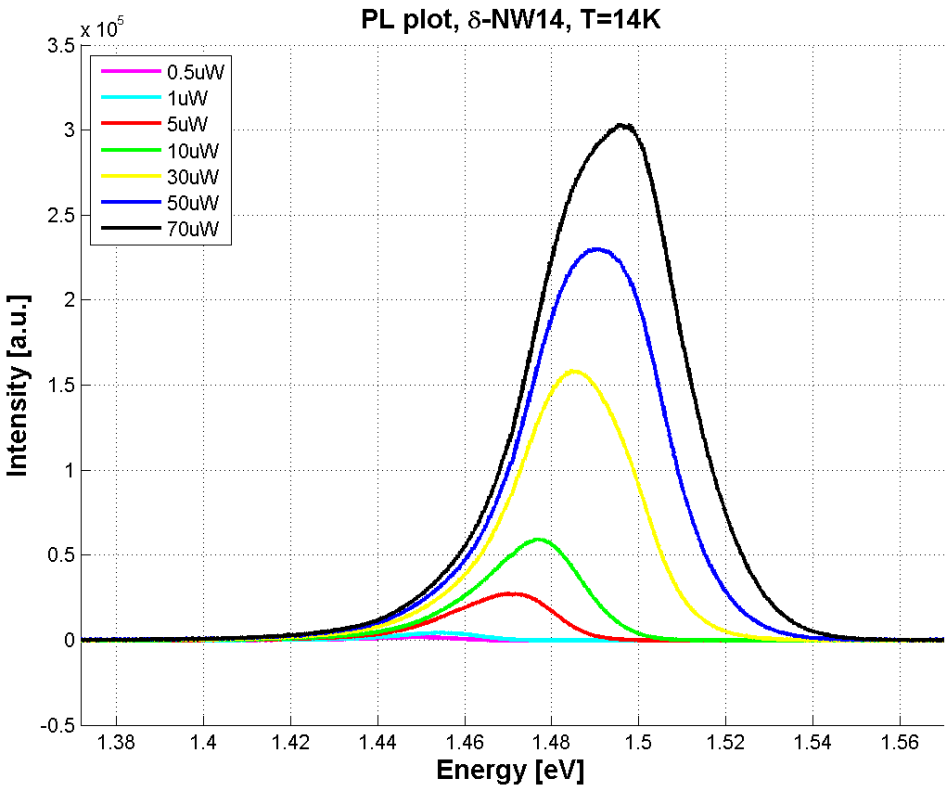

Figure 4.1: PL emission spectrum and emission energy for δ-NW14 at $14K$. Measurements are done at increasing laser excitation power.

4.1.2 Sample ψ

Figure 4.2 shows the PL emission intensity of ψ-NW01, measured at $14K$. Emission is strongest at $1.481eV$ at low temperature and $10\mu W$ laser power. It shows a strong shift to higher energy as LP increases. The emission is similar to the peak of δ-NW14, but ψ-NW01 has a narrower peak. This plot is representative for all but one NW from sample ψ, presented in Appendix A.

Since no excitonic transitions are observed, power dependence analysis on the emission was not conducted.

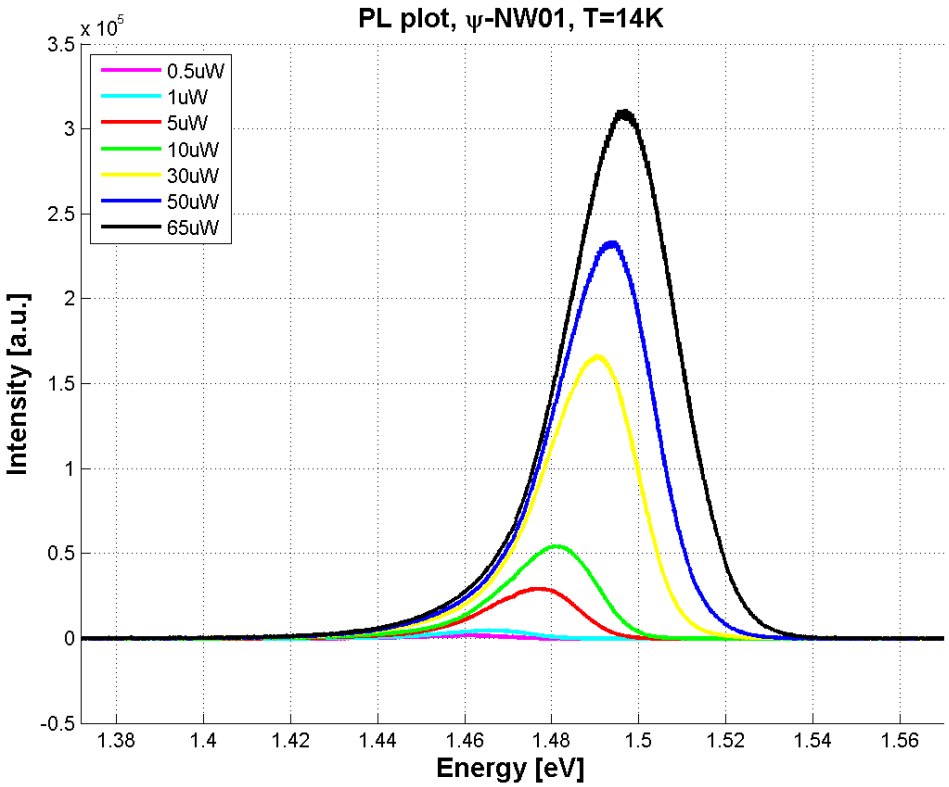

Figure 4.2: PL emission spectrum and emission energy for ψ-NW01 at $14K$. Measurements are done at increasing laser excitation power.

4.1.3 Sample σ

Figure 4.3 shows the PL emission intensity of σ-NW16, measured at $16K$. Two peaks are dominating, one at $1.500eV$ and one at $1.517eV$ for $5\mu W$ laser power. From the $1\mu W$ plot, another peak around $1.470eV$ is also resolvable. The plot of σ-NW16, with two peaks at around $1.500eV$ and $1.515eV$ is representative for other NWs from sample σ.

The $1.515eV$ transition was fitted to Gaussians from $0.5 - 10\mu W$ LP (Fig. 4.4a), and the total signal from these Gaussians fitted to equation (4.1) (Fig. 4.4b). The integrated intensity fit shows that the NW exhibits near linear laser power dependence, which is in accordance with free exciton emission.

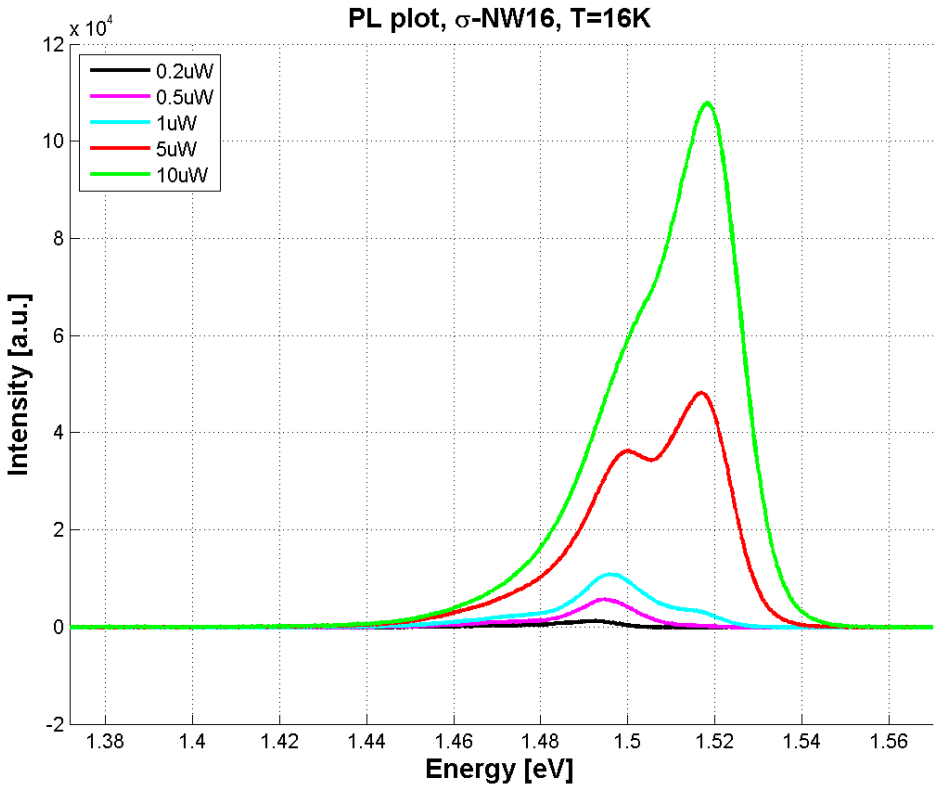

Figure 4.3: PL emission spectrum and emission energy for σ-NW16 at $16K$. Measurements are done at increasing laser excitation power.

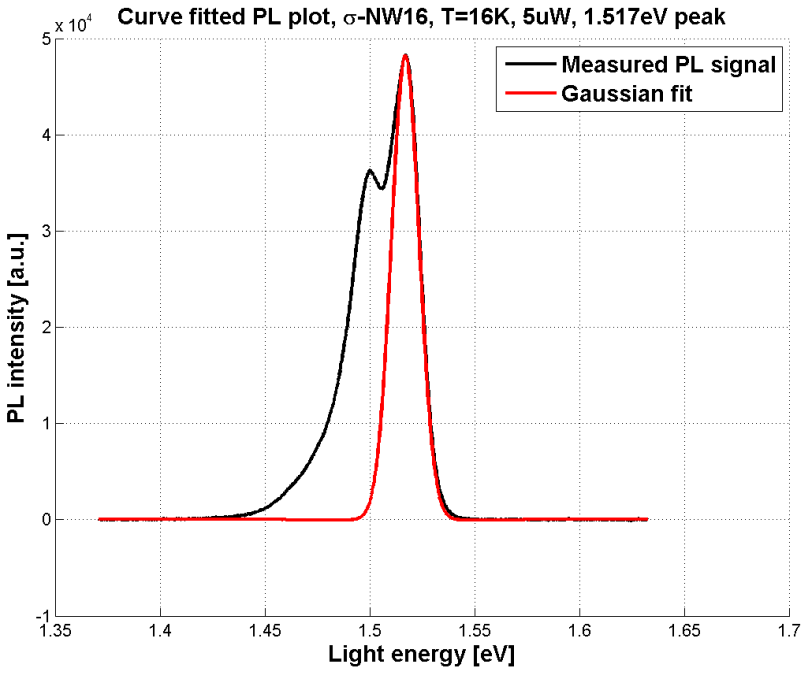

(a) Gaussian fit of $1.517eV$ peak, measured at $5\mu W$ laser power.

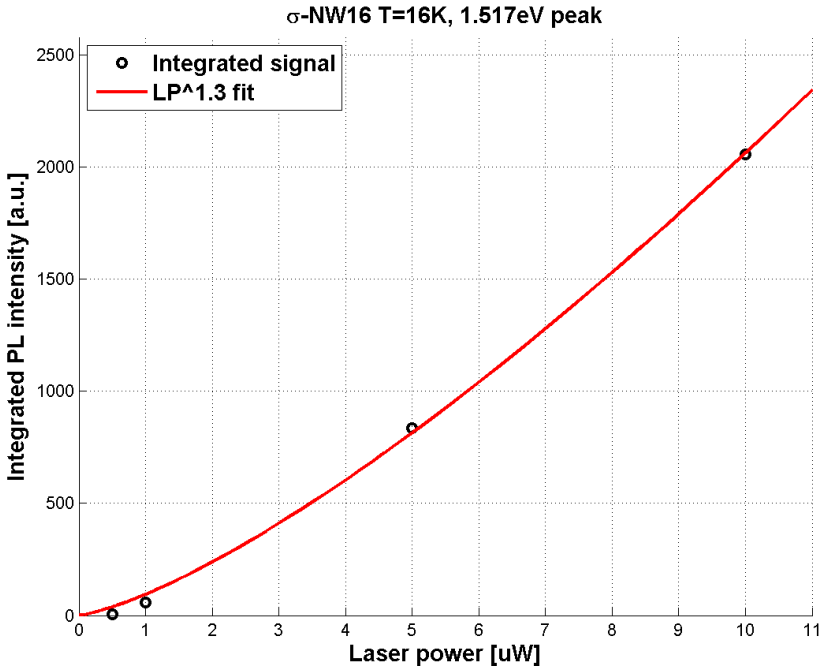

(b) Integrated intensity plot for σ-NW16, peak at $1.517eV$.

Figure 4.4: Gaussian fit and curve fit of integrated intensity of the $1.517eV$ emission peak, sample σ-NW16, measured at $16K$.

4.1.4 Sample α

Sample α is to be used as a reference sample during analysis of the other three samples. Figure 4.5 shows the PL emission intensity of α-NW09, measured at $10K$. For low laser power, $0.2-1\mu W$, peaks at $1.496eV$ and $1.506eV$ are dominating. For higher laser power, $5-10\mu W$, two peaks at $1.506eV$ and $1.515eV$ are dominating, while the lower peak at $1.496eV$ is visible as a shoulder in the total spectrum. The emission from α-NW09 is representative for the NWs from sample α.

As for sample σ, the $1.515eV$ emission was fitted to Gaussians from $0.2-10\mu W$ LP (Fig. 4.6a), and the total signal from these Gaussians fitted to equation (4.1) (Fig. 4.6b). The integrated intensity shows that the NW exhibits linear to superlinear laser power dependence. The data points at low laser power ($LP \leq 1\mu W$) are uncertain, making the curve appear more superlinear than what is likely the case. It is therefore more likely that this is free exciton emission. Also the temperature dependence of this peak, presented in figure 4.11b, support this.

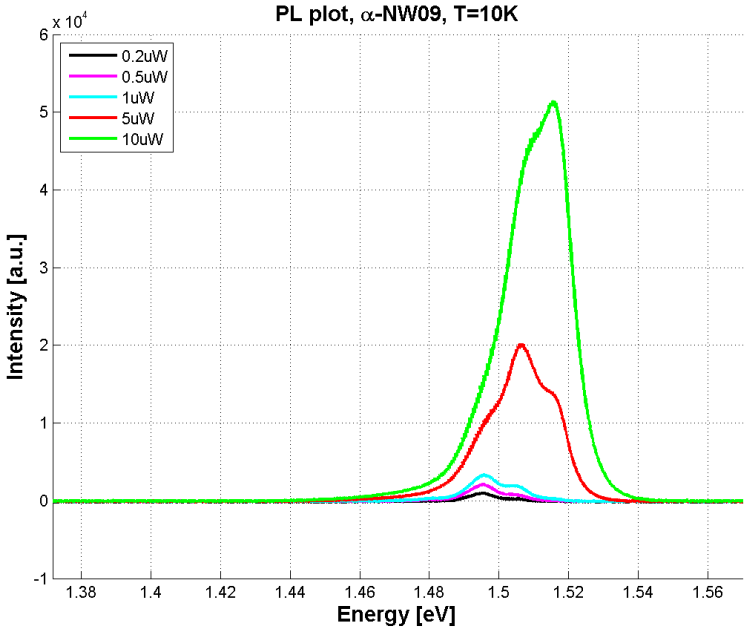

Figure 4.5: PL emission spectrum and emission energy for α-NW09 at $10K$. Measurements are done at increasing laser excitation power.

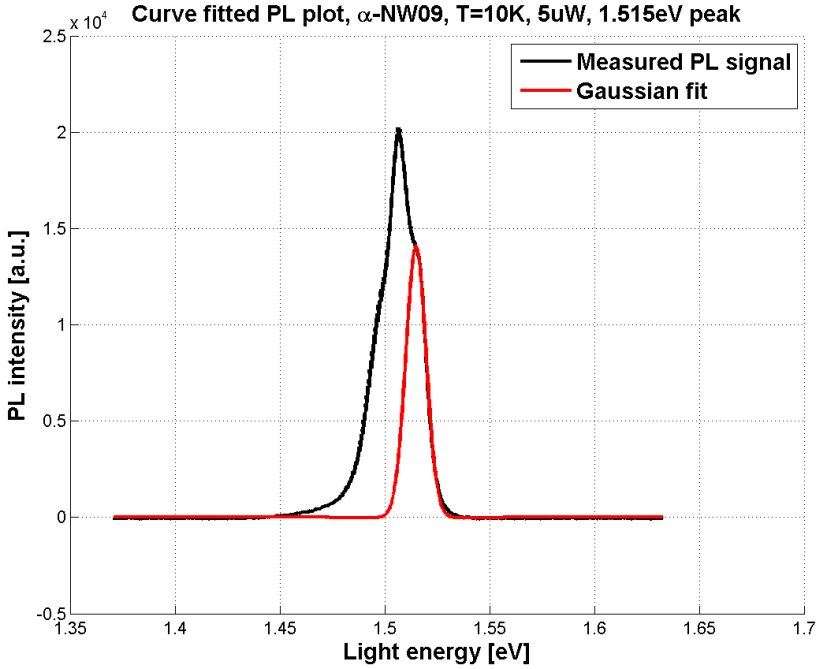

(a) Gaussian fit of $1.515eV$ peak, measured at $5\mu W$ laser power.

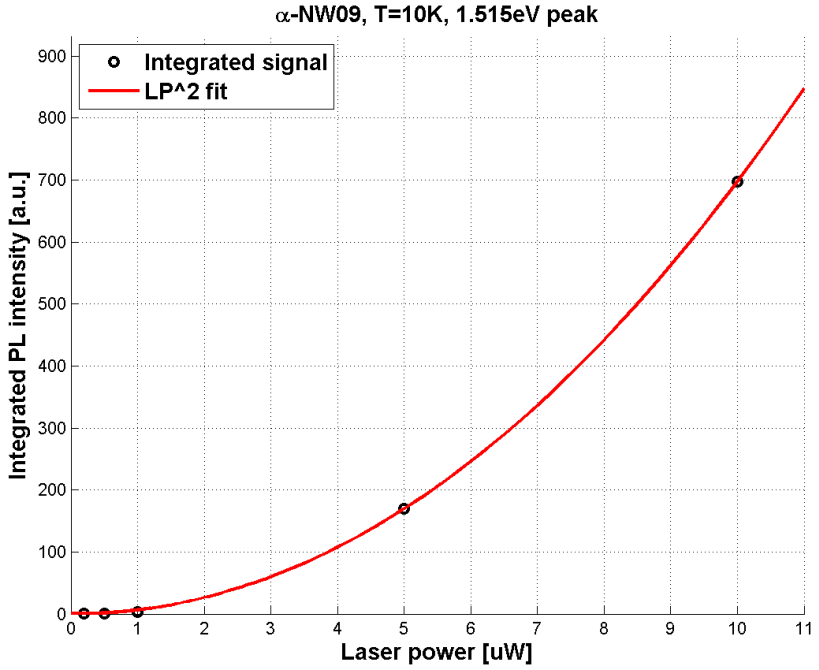

(b) Integrated intensity plot for α-NW09, peak at $1.515eV$.

Figure 4.6: Gaussian fit and curve fit of integrated intensity of the $1.515eV$ emission peak, sample α-NW09, measured at $10K$.

4.1.5 Full width at half maximum

The *full width at half maximum* (FWHM) was measured for the samples that exhibited emission around the ZB GaAs free exciton energy of $1.515eV$. The results are taken from Gaussians fitted at $5\mu W$ LP measurements at low temperature, and are presented in table 4.2.

Sample-NW	FWHM [meV]
δ-NW14	–
ψ-NW01	–
σ-NW16	$16.3meV$
α-NW09	$11.6meV$

Table 4.2: Table showing the full width at half maximum for the $\sim 1.515eV$ peak, of the NWs analyzed. The data is obtained at low temperature and at laser power $5\mu W$.

The FWHM value for sample δ and ψ is left blank, because no NWs from these samples had emission at the free exciton energy. The FWHM values for sample σ and α are obtained from the fits seen in figures 4.4a and 4.6a, respectively. The two samples have relatively narrow peaks, within what is expected of free exciton emission.

4.2 Temperature dependence of emission energy

As mentioned, laser power dependent measurements were done on all NWs at low temperature. The most promising NWs were chosen for further measurements, which involves doing LP dependent measurements at higher temperatures. In total, measurements were done at $\sim 14K$, $30K$, $50K$, $70K$, $100K$, $150K$, $200K$, $250K$ and $290K$, giving 9 sets of PL spectra for each NW. Peaks were followed from low to high energy, as is shown in the seven plots of figure 4.7, with temperature as the only changing parameter (LP = $10\mu W$).

The result was a data set containing temperature and emission energy, which was plotted together. This was done for all four samples, and for samples with several transitions, all peaks were followed. Included in the plots is data from bulk ZB GaAs [75] and a ZB GaAs epilayer [61], used for comparison. The results from δ-NW14, ψ-NW01, σ-NW16 and α-NW09 are listed in table 4.3, and the temperature dependent plots resulting from the data in the table follows.

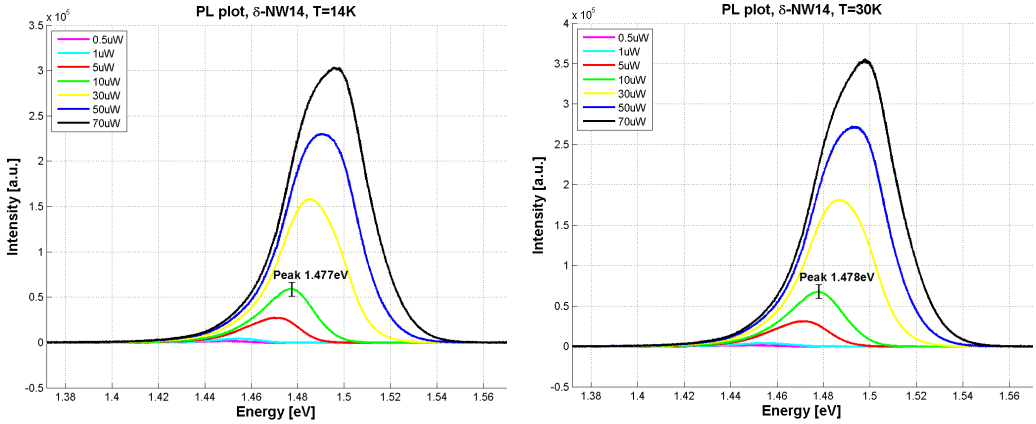

(a) $14K$

(b) $30K$

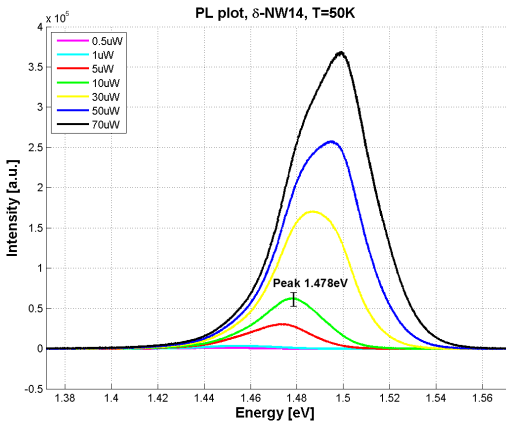

(c) $50K$

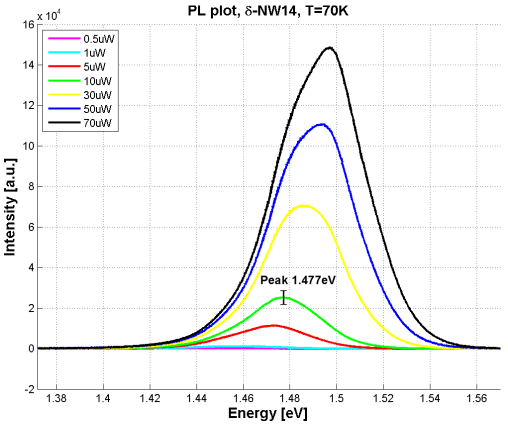

(d) $70K$

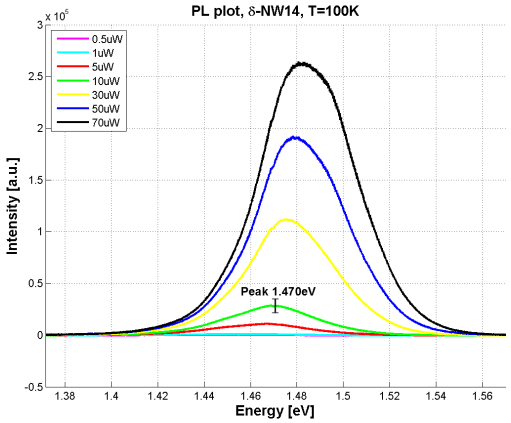

(e) $100K$

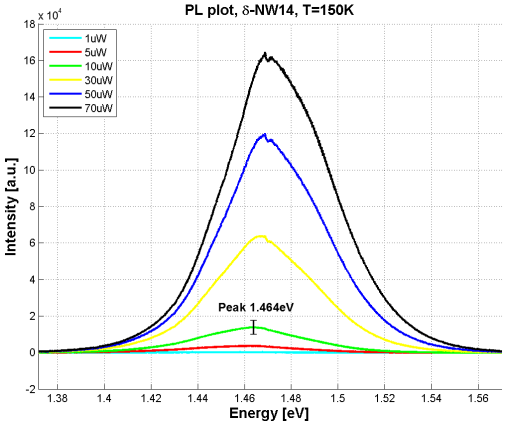

(f) $150K$

Figure 4.7: PL emission spectra for δ-NW14, done at temperatures ranging from $14K$ to $290K$. The $1.477eV$ (low temperature) peak is followed and marked for $LP = 10\mu W$. These are figures for $14 - 150K$.

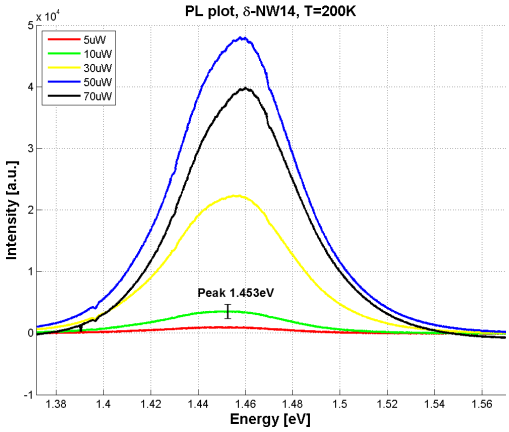

(g) $200K$

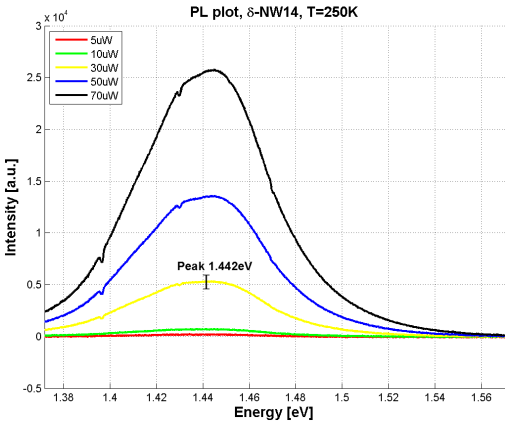

(h) $250K$

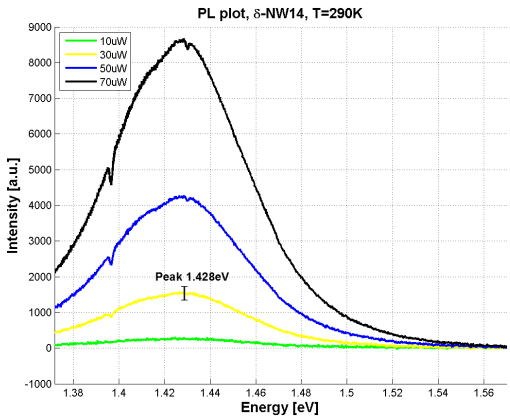

(i) $290K$

Figure 4.7: PL emission spectra for δ-NW14, done at temperatures ranging from $14K$ to $290K$. The $1.477eV$ (low temperature) peak is followed and marked for $LP = 10\mu W$ (and $LP = 30\mu W$ for high temperature). These are figures for $200 - 290K$.

(a)

$\delta - NW14$									
Temp. [K]	14	30	50	70	100	150	200	250	290
Emission en. Low peak [eV]	1.477	1.478	1.478	1.477	1.470	1.464	1.453	1.442	1.428

(b)

$\psi - NW01$									
Temp. [K]	14	30	50	70	100	150	200	250	290
Emission en. Low peak [eV]	1.481	1.475	1.481	1.476	1.472	1.467	1.446	1.445	1.439

(c)

$\sigma - NW16$									
Temp. [K]	16	30	50	70	100	150	200	250	293
Emission en. Low peak [eV]	1.502	1.500	1.497	1.492	1.481	1.464	1.436	1.423	1.422
High peak [eV]	1.518	1.515	1.517	1.513	1.507	1.490	1.471	1.454	1.432

(d)

$\alpha - NW09$									
Temp. [K]	10	30	50	70	100	150	200	250	293
Emission energy Low peak [eV]	1.506	–	1.502	–	1.483	1.469	1.455	1.424	1.427
High peak [eV]	1.516	–	1.515	–	1.504	1.490	1.471	1.454	1.434

Table 4.3: Temperature dependence of emission energy for chosen peaks from NWs of all samples.

4.2.1 Sample δ

The temperature dependence of δ-NW14 (Fig. 4.8), accurately depicts the observed results of NWs from sample δ. It is evident that the emission energy at low temperature, $1.477eV$, diverges from that of free exciton emission, $1.515eV$. The low energy can be due to type-II transitions, as is described in section 2.4.3 and figure 2.8. The bulk ZB→WZ emission energy is $\sim 1.43eV$ at $290K$ [37], consistent with these results. The temperature dependent measurements are in accordance with type-II emission at low temperature, indicating interchanging ZB-WZ segments. At room temperature, ZB band-to-band transitions become dominant.

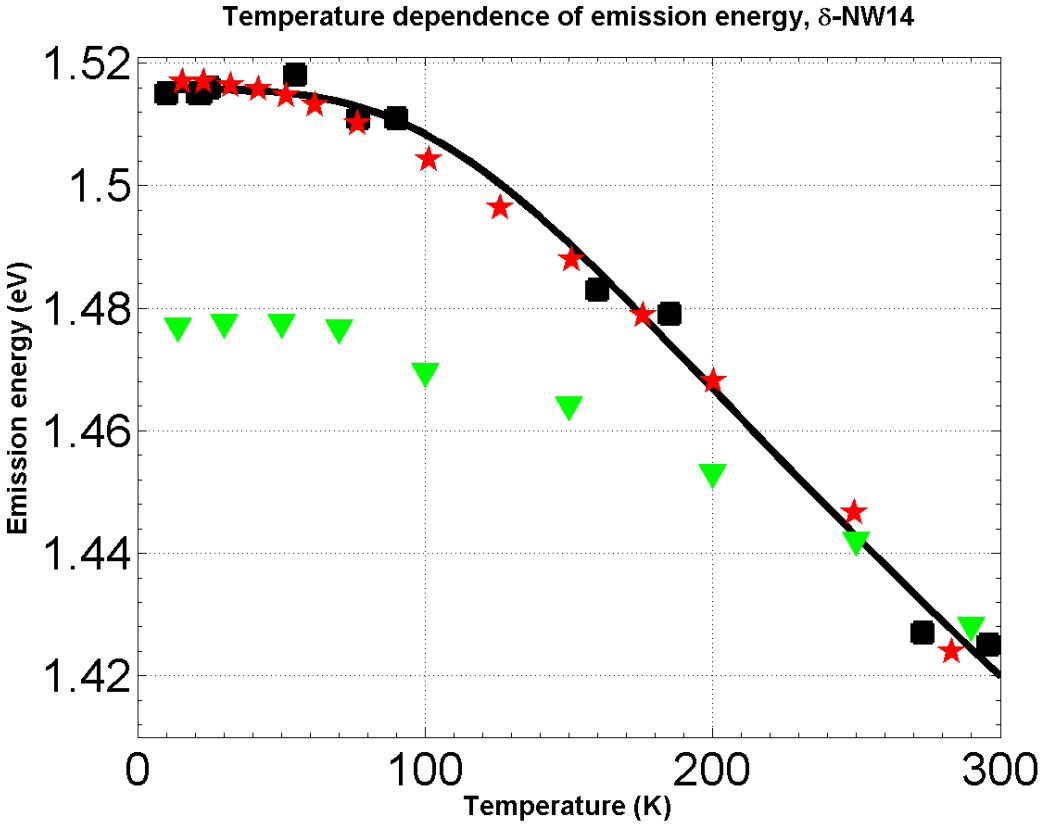

Figure 4.8: Temperature dependence of emission energy for δ-NW14, resulting from data in table 4.3a. Also included in the plot is data for a **ZB GaAs epilayer** and a Varshni fitted curve for **bulk ZB GaAs**.

4.2.2 Sample ψ

Figure 4.9 shows the temperature dependence of ψ-NW01, emitting at $1.481eV$ at low temperatures. The energy is lower than that of free exciton emission at all temperatures, an indication of type-II transitions from several ZB-WZ stacking faults. Band-to-band transitions are observed at room temperature.

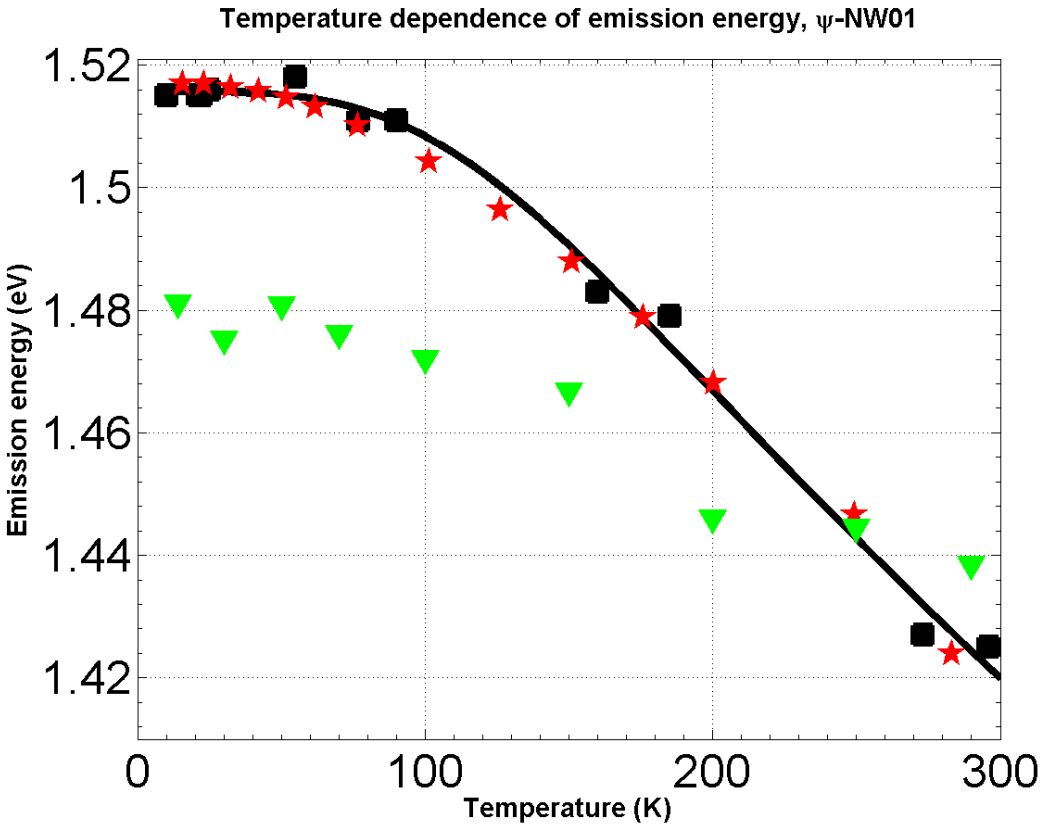

Figure 4.9: Temperature dependence of emission energy for ψ-**NW01**, resulting from data in table 4.3b. Also included in the plot is data for a **ZB GaAs epilayer** and a Varshni fitted curve for **bulk ZB GaAs**.

4.2.3 Sample σ

For σ-NW16, two transitions are observed. The lower energy peak emits at $1.502eV$ at low temperatures, whereas the high energy peak emits at $1.518eV$. Both these peaks were followed and plotted, resulting in figures 4.10a and 4.10b.

The low energy transition emits at energies lower than free exciton, indicating type-II emission and ZB-WZ stacking faults, as in the other samples. The high energy emission follows the bulk ZB emission line quite well, indicating free exciton emission at low temperature. This can occur in large, pure segments of ZB GaAs in the core of the NW.

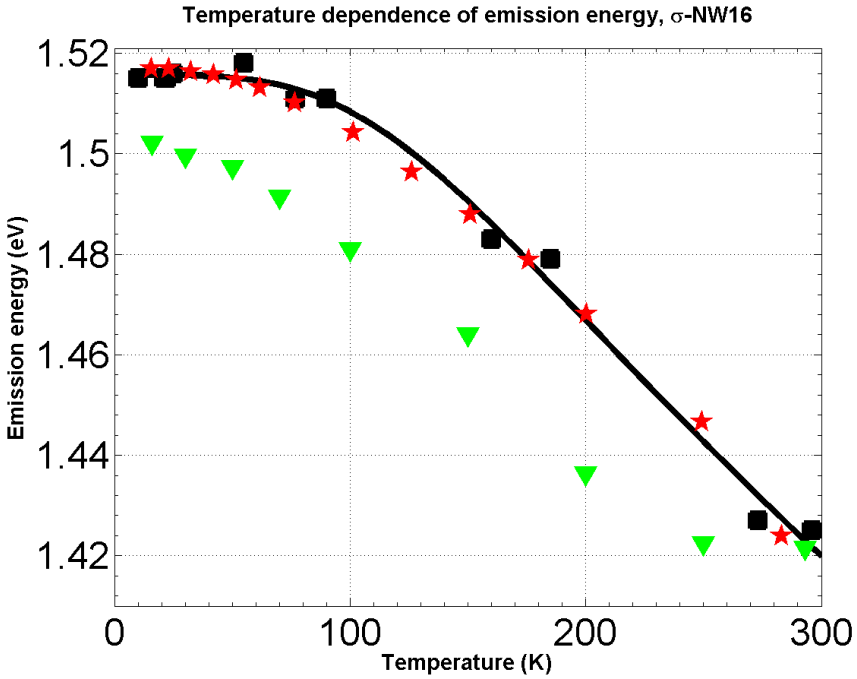

(a) Low energy peak starting at $1.502eV$.

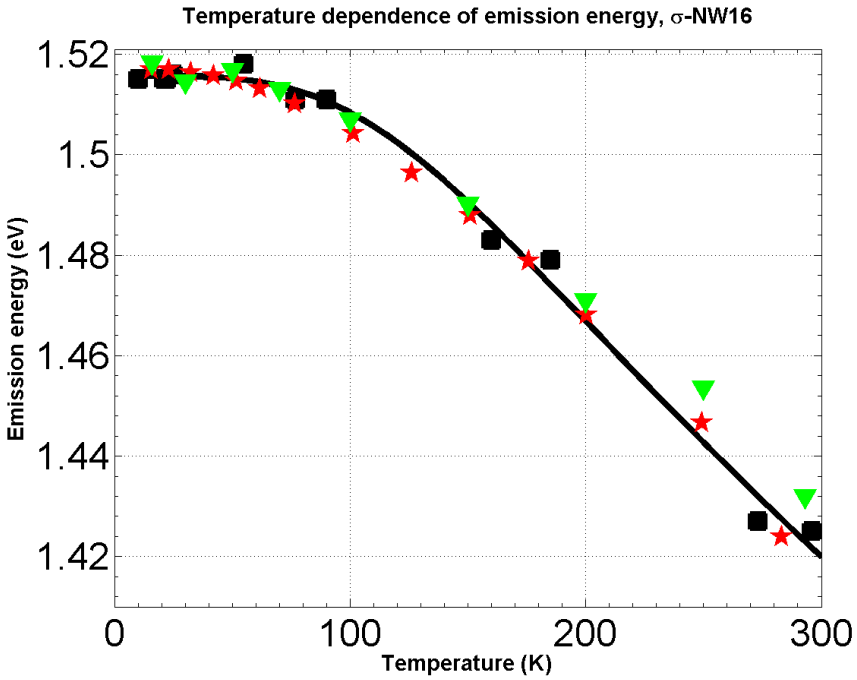

(b) High energy peak starting at $1.518eV$.

Figure 4.10: Temperature dependence of emission energy for σ-NW16, resulting from data in table 4.3c. Also included in the plot is data for a **ZB GaAs epilayer** and a Varshni fitted curve for **bulk ZB GaAs**.

4.2.4 Sample α

Two peaks are also observed for α-NW09. They have low temperature emission energy of $1.506eV$ and $1.516eV$. The temperature dependence of these transitions are seen in figures 4.11a and 4.11b.

The low energy peak shows similar behavior as the low energy peak of σ-NW16 (Fig. 4.10a) at low temperatures. At higher temperatures, however, the lower peak is hard to resolve, and nearly disappears from the PL emission plot at $200K$. The high energy peak emits very close to the free exciton line at low temperature, and is likely to come from the core of the NW.

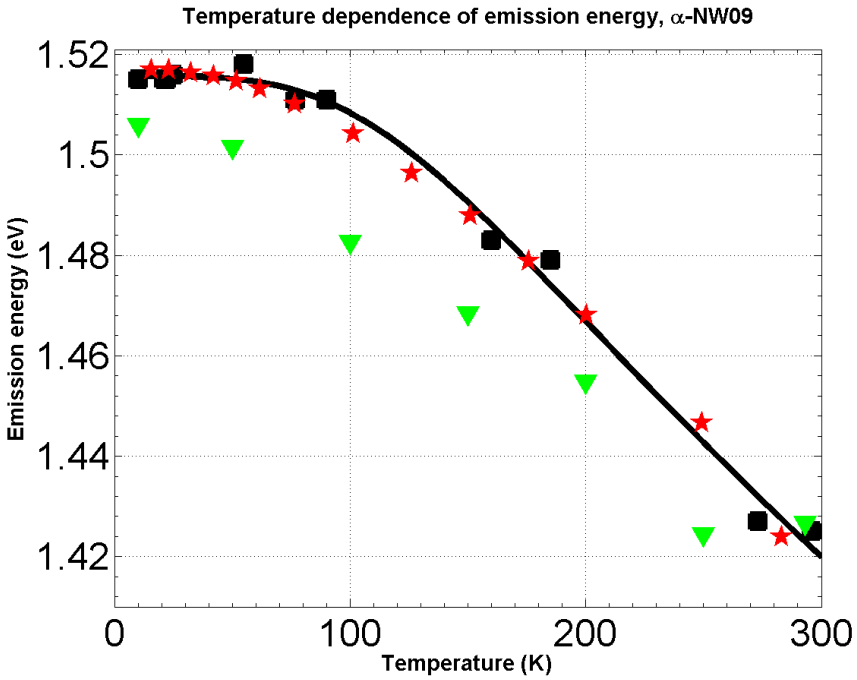

(a) Low energy peak starting at $1.506eV$.

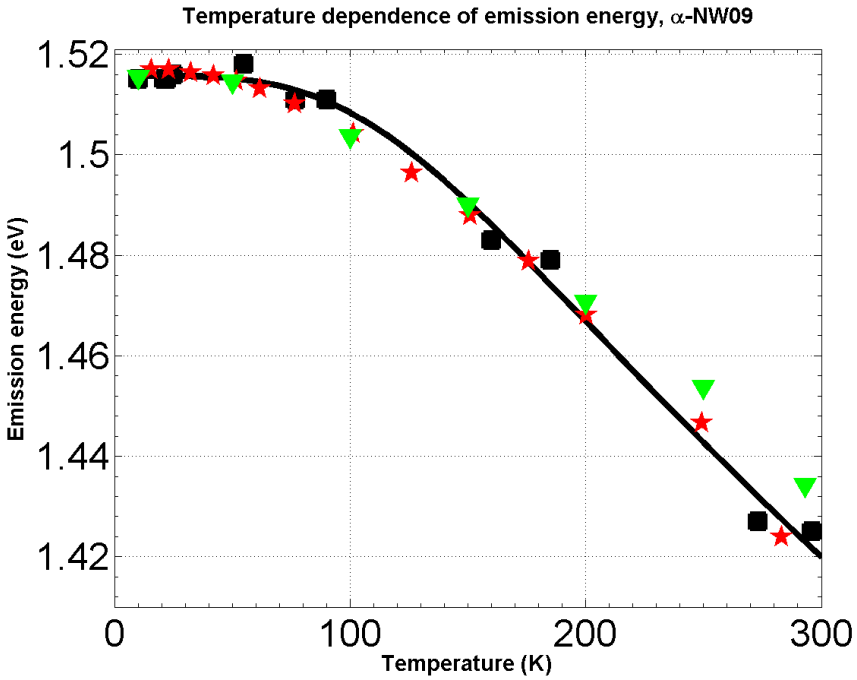

(b) High energy peak starting at $1.516eV$.

Figure 4.11: Temperature dependence of emission energy for α-NW09, resulting from data in table 4.3d. Also included in the plot is data for a **ZB GaAs epilayer** and a Varshni fitted curve for **bulk ZB GaAs**.

4.2.5 Temperature dependence of emission intensity

The temperature dependence of the emission intensity of the NWs is compared at low temperature $\sim 15K$ and high temperature $\sim 290K$. When comparing PL spectra at different temperatures, all other parameters staying constant, the decrease in PL brightness is due to decrease in quantum efficiency. Therefore, this ratio can be used as one measure of the optical quality of the samples, and their suitability for optoelectronic applications at normal temperatures. A lower value is preferred.

Table 4.4 contains the data found from figures 4.12a-4.12d. Different laser power was used for the different samples because some samples did not emit at lower laser power at high temperature.

Sample-NW	PL($15K$) / PL($290K$)
δ-NW14	101
ψ-NW01	354
σ-NW16	1021
α-NW09	468

Table 4.4: Table showing the ratio between PL emission at $\sim 15K$ and $\sim 290K$ for all samples. This ratio can be used as a measure of optical quality.

The data clearly shows that sample δ has the lowest value, which is preferred for this test. Samples ψ and α has similar values, whereas σ has a much higher value than the other samples, thus indicating poor optical properties at room temperature.

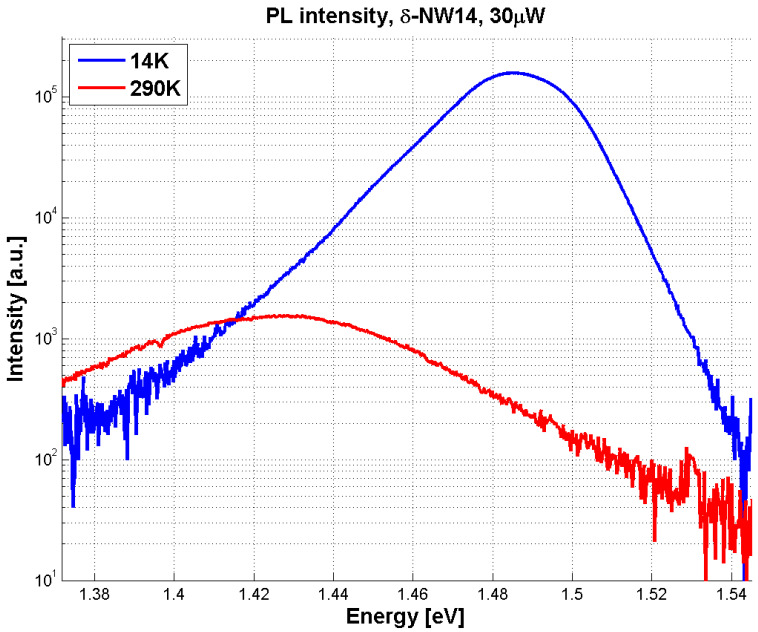

(a) δ-NW14, measured at $30\mu W$ laser power

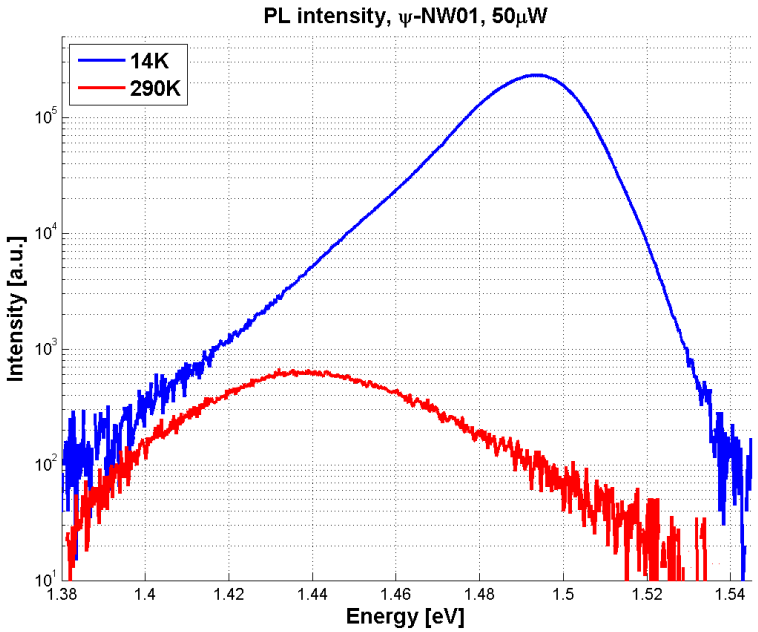

(b) ψ-NW01, measured at $50\mu W$ laser power

Figure 4.12: Plots showing the PL emission intensity versus emission energy, for NWs from samples δ and ψ.

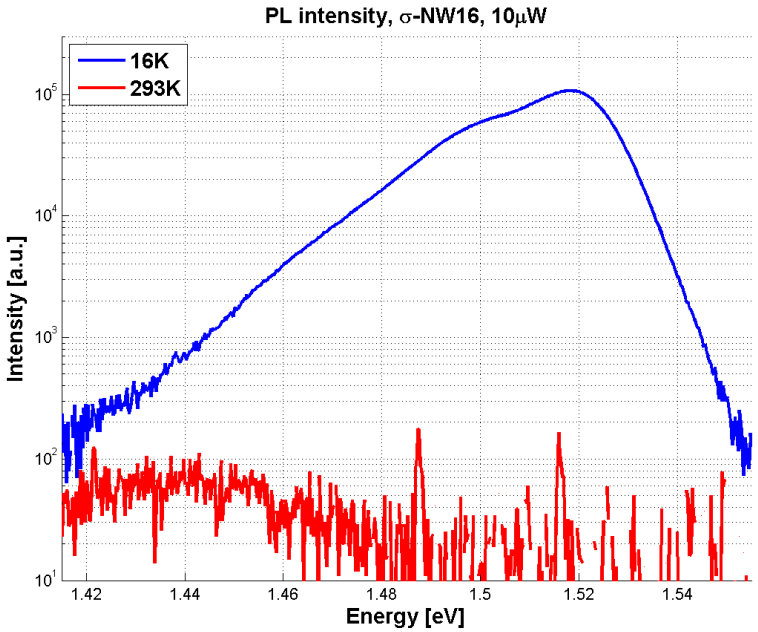

(c) σ-NW16, measured at $10\mu W$ laser power

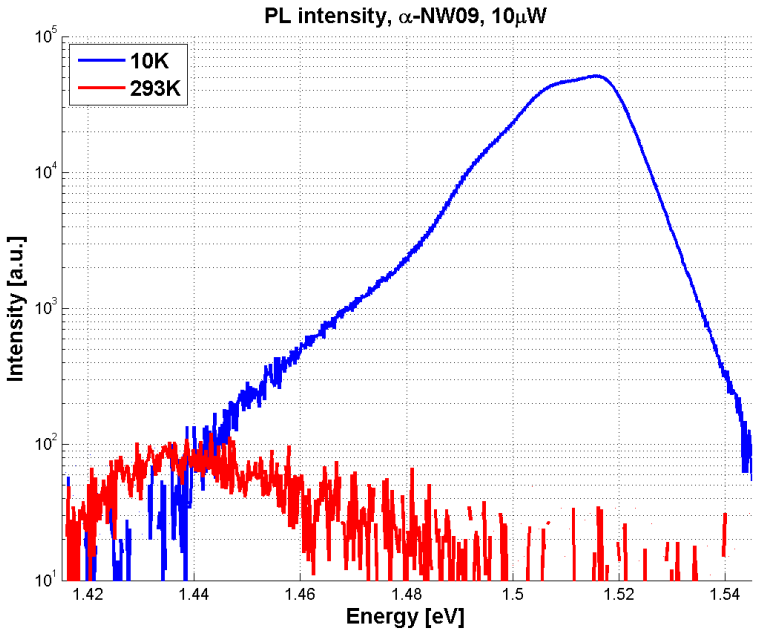

(d) α-NW09, measured at $10\mu W$ laser power

Figure 4.12: Plots showing the PL emission intensity versus emission energy, for NWs from samples σ and α.

4.3 Polarization dependence of emission intensity

For a detailed description of the polarization-resolved photoluminescence (PRPL) instrumental setup and measurement techniques, see sections 3.2.4.2 and 3.3.3, respectively.

The PRPL measurements consisted of two steps. In the first step, the laser excitation light was polarized before exciting the NWs to determine the angular position of the NW with respect to the x-axis (parallel to the optical table). The method involved exciting the NW with light of polarization prepared by a half-wave plate at angles $C \in [0°; 100°]$, with steps of 5°, placed after a polarizer at 90°. The 21 emitted signals were then fitted to an appropriate number of Gaussians. Then the total emission intensity of each Gaussian fit was plotted for each value of C, and fitted to equation (3.5), which is restated here:

$$I_{PL} \sim \left|E_{s\|NW}\right|^2 = \sin^2(2C - \alpha).$$

Here I_{PL} is the emission intensity, C is the compensator angles and α is the angle of the NW with respect to the x-axis. For more information on the setup and measurements, see sections 3.2.4.1 and 3.3.2, respectively.

When α has been determined, the sample is excited with circularly polarized light. Then the signal *emitted* from the NW is polarized, and scanned over $C \in [0°; 100°]$, as before. The data is processed almost exactly as for excitation polarization, except now the emission is fitted to equation (3.12):

$$I_{spectrometer} \sim |E_{PL}|^2 = \sin^2(2C - \beta),$$

where $I_{spectrometer}$ is the intensity of the signal detected by the spectrometer. By combining the values found for the orientation of the NW, α, and the polarization of the emitted signal, β, the polarization with respect to the NW can be found. This holds information on the material properties of the sample.

One of the 21 Gaussian curve fits can look like the one in figure 4.13a. Combining the 21 plots gives a 3D energy and polarization dependent intensity plot, as in figure 4.18a, where the color scales ranges from dark blue to dark red with increasing intensity. Also the emission intensity from one peak, fitted to a sin^2 function,

can be seen in figure 4.13c. The function also accounts for drift in the experimental setup, which affects intensity over the time it takes to do the measurements. A margin of error of $\pm 5^{\circ}$ must be taken into account.

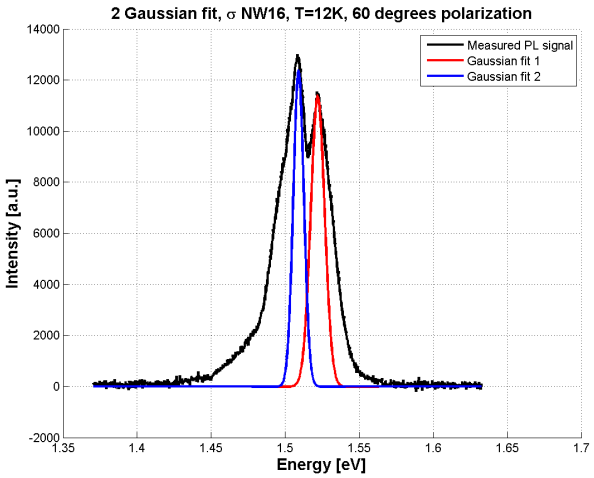

(a) Polarization dependence measurement at 60° compensator angle. Two Gaussian curves are fitted to the signal.

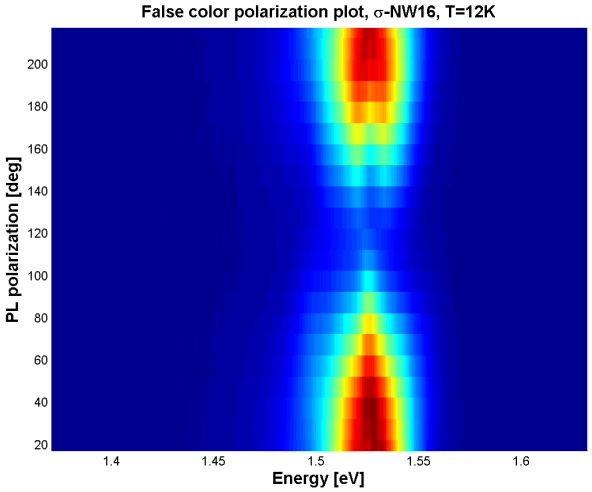

(b) False color plot of intensity dependence on emission energy and compensator angle.

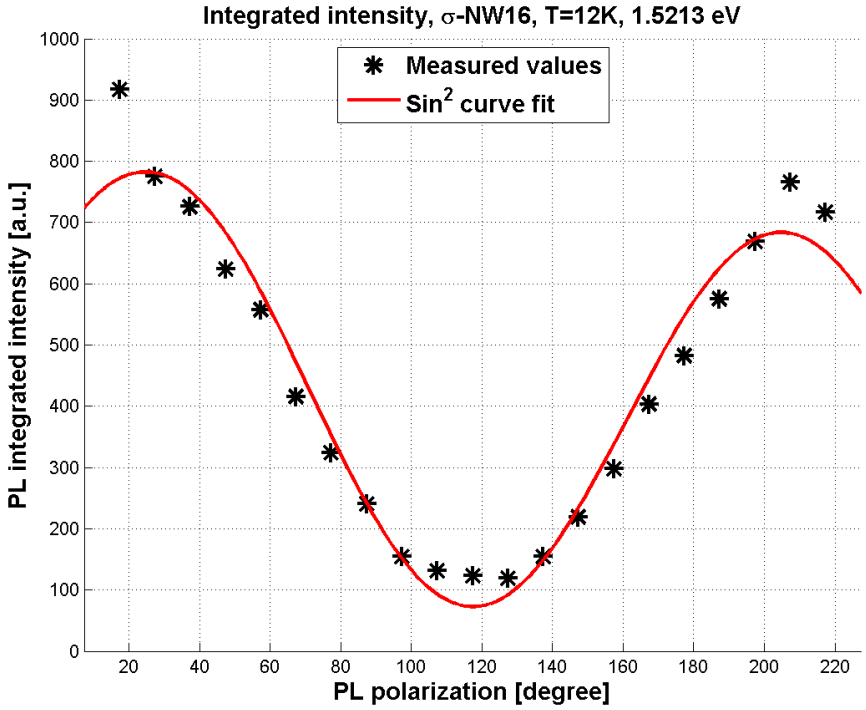

(c) Polarization dependence of emission intensity of $1.5213eV$ peak fitted to sin^2 function.

Figure 4.13: Excitation polarization dependence measurement on σ-NW16 at $12K$ and $20\mu W$ LP.

4.3.1 Sample δ

The polarization data collected from δ-NW14 is plotted as a false color plot in figure 4.14a. Figure 4.14b shows the same data, where the plot is viewed from a different angle to visualize the difference in emission intensity. The PL emission from δ-NW14 does not show much polarization dependence, as can also be seen for other NWs from this sample, in Appendix B. Two peaks can be resolved, at energy $\sim 1.45eV$ and $\sim 1.48eV$, where the latter is much stronger than the former.

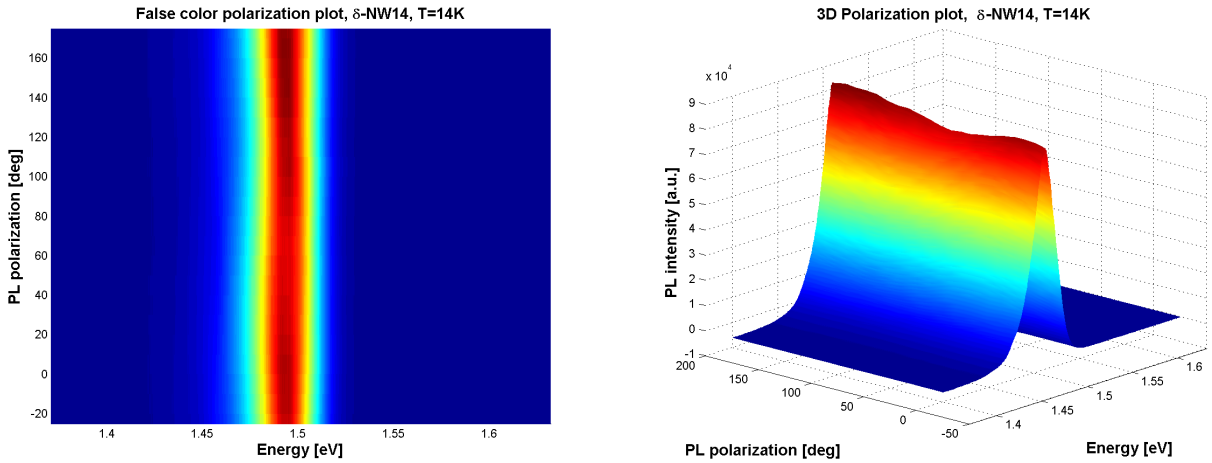

(a) Viewed from above.

(b) Viewed from the side.

Figure 4.14: False color plots of the polarization- and energy dependence of emission intensity for δ-NW14, done at $14K$.

The result from curve fitting with two Gaussians and the sin^2 function is shown in figures 4.15a and 4.15b. Because the low energy transition is only visible as a "shoulder" in the total plot, the curve fitting method has difficulties getting a good fit for both peaks at the same time. The results from the sin^2 curve fitting is presented in table 4.5.

The results clearly shows that none of the peaks are emitting at parallel or perpendicular polarization to the NW. Because there is a big difference in polarization from the two peaks, a plot of the total emission from the sample fitted to a sin^2 curve is not of interest, and therefore not included.

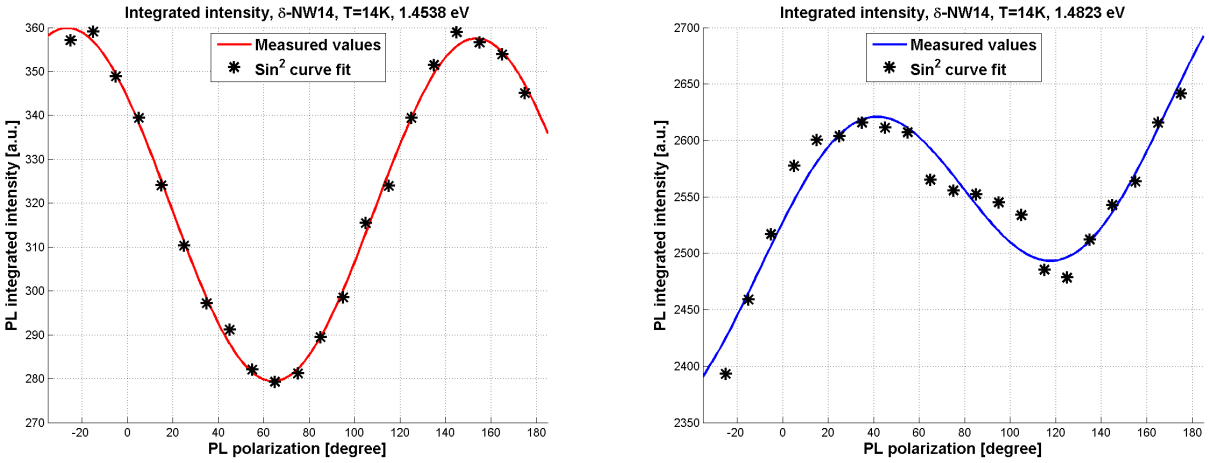

(a) δ-NW14, 1.454eV peak.

(b) δ-NW14, 1.482eV peak.

Figure 4.15: sin^2 fits of the PL emission intensity for δ-NW14 at 14K. The figures are for peaks at different energies.

δ-NW14	Peak energy [eV]	Angle to NW [deg]
	1.454	$-26.2°$
	1.482	$34.5°$

Table 4.5: Polarization data for δ-NW14 at 14K, resulting from curve fitting of peaks to a sin^2 function (Fig. 4.15).

4.3.2 Sample ψ

False color plots of ψ-NW01 are shown in figures 4.16a and 4.16b. The plot indicates that at least two peaks are emitting at fairly close energies, $\sim 1.49eV$ and $\sim 1.51eV$. The polarization difference of the two transitions seems to be about 20°.

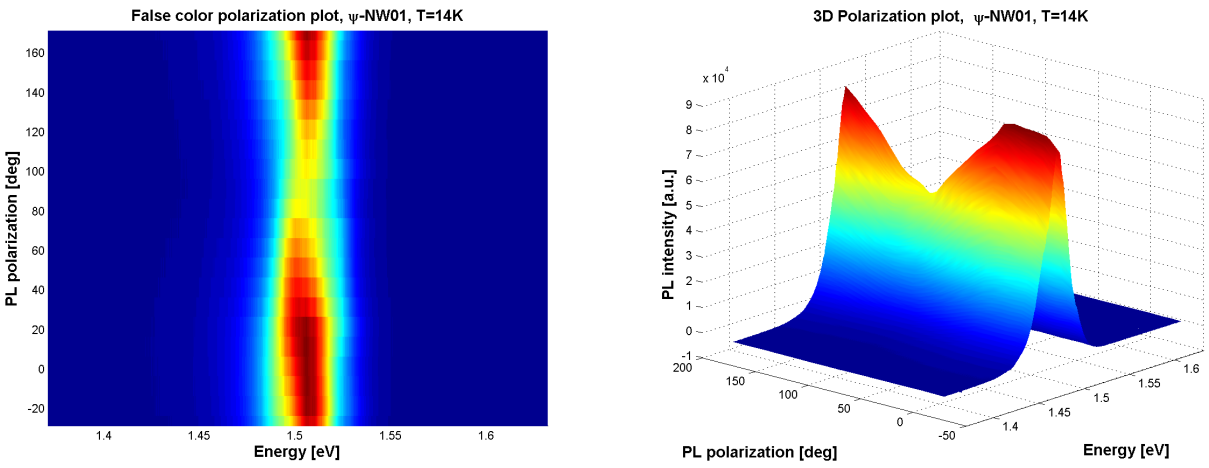

(a) Viewed from above.

(b) Viewed from the side.

Figure 4.16: False color plots of the polarization- and energy dependence of emission intensity for ψ-NW01, done at $14K$.

From figure 4.16, it was concluded to use two Gaussians to fit the spectrum. The total spectrum was also fitted. The three resulting sin^2-fitted plots are shown in figure 4.17. Table 4.6 contains the results from the fits.

Both peaks are emitting fairly close to parallel with the NW axis, and so is the total emission. The peaks are also of similar intensity.

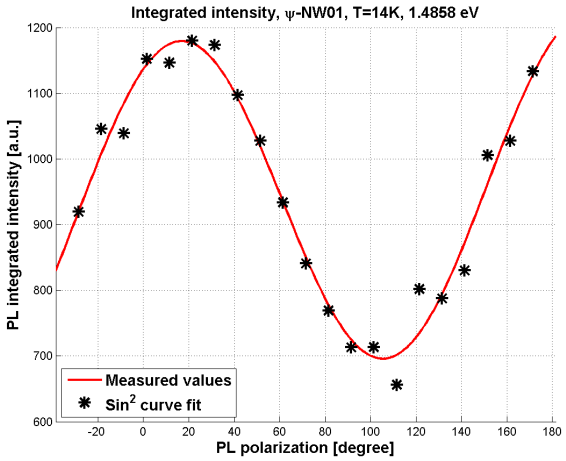

(a) ψ-NW01, 1.486eV peak.

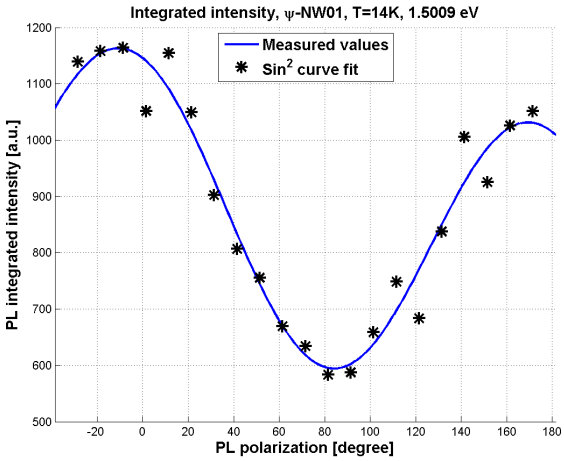

(b) ψ-NW01, 1.501V peak.

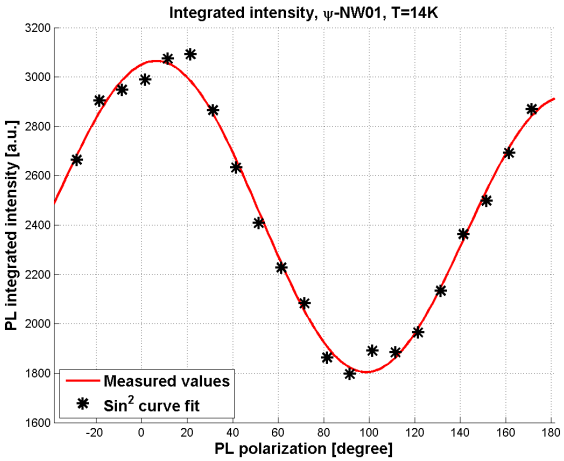

(c) ψ-NW01, total emission.

Figure 4.17: sin^2 fits of the PL emission intensity for ψ-NW01 at 14K. The figures are for peaks at different energies and one fit for the total emission.

ψ-NW01	Peak energy [eV]	Angle to NW [deg]
	1.486	16.1°
	1.501	−8.4°
	Total	7.4°

Table 4.6: Polarization data for ψ-NW01 at 14K, resulting from curve fitting of peaks to a sin^2 function (Fig. 4.17).

4.3.3 Sample σ

Figures 4.18a and 4.18b show the result from polarization dependent measurements on σ-NW16. Two peaks are visible $\sim 1.51eV$ and $\sim 1.52eV$. The PL emission intensity of the two peaks are on the same order of magnitude.

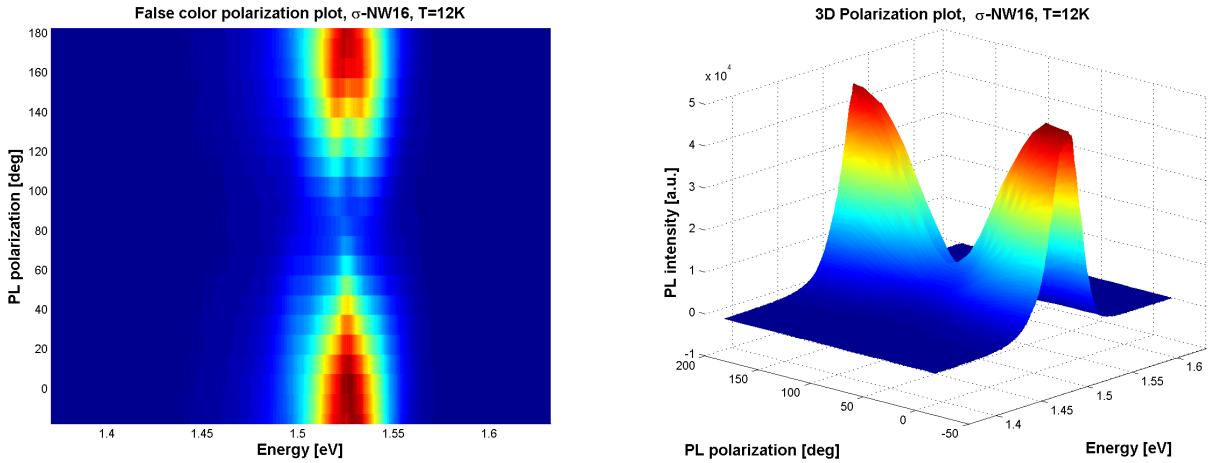

(a) Viewed from above.

(b) Viewed from the side.

Figure 4.18: False color plots of the polarization- and energy dependence of emission intensity for σ-NW16, done at $12K$.

Curve fitting two Gaussians to the polarization data, yielded the sin^2 plots in figures 4.19a and 4.19b. The fit to the total emission is seen in figure 4.19c. The numerical results are included in table 4.7.

The $1.507eV$ emission and the $1.522eV$ emission are both close to parallel polarization, at angles $7.5°$ and $-10.0°$, respectively. The high energy peak, might therefore be excitonic emission. Polarization data for the $\sim 1.515eV$ peak of other NWs from sample σ is included in Appendix C.

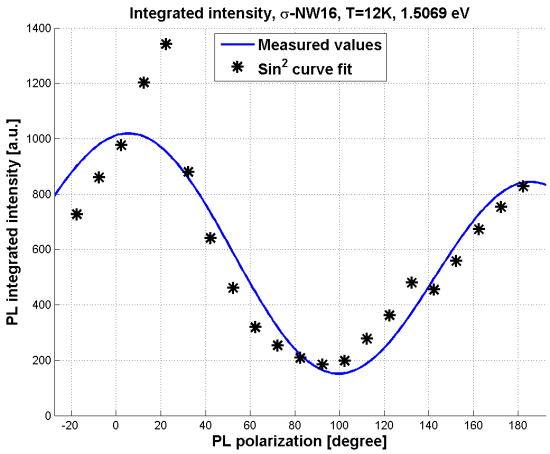

(a) σ-NW16, 1.507eV peak.

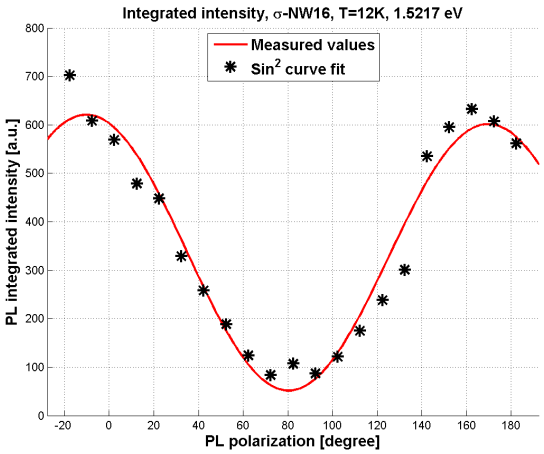

(b) σ-NW16, 1.522eV peak.

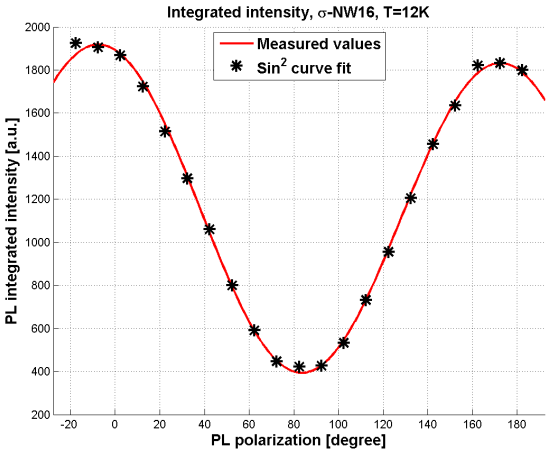

(c) σ-NW16, total emission.

Figure 4.19: sin^2 fits of the PL emission intensity for σ-NW16 at 12K. The figures are for peaks at different energies and one fit for the total emission.

σ-NW16	Peak energy [eV]	Angle to NW [deg]
	1.507	7.5°
	1.522	−10.0°
	Total	−7.0°

Table 4.7: Polarization data for σ-NW16 at 12K, resulting from curve fitting of peaks to a sin^2 function (Fig. 4.19).

4.3.4 Sample α

Polarization data from α-NW09 is plotted in false color plots in figures 4.20a and 4.20b. It can be assumed that the plots show two peaks emitting at similar energies, $\sim 1.51eV$ and $\sim 1.52eV$. The emissions are of approximately the same intensity, but have almost perpendicular polarization with regard to one another.

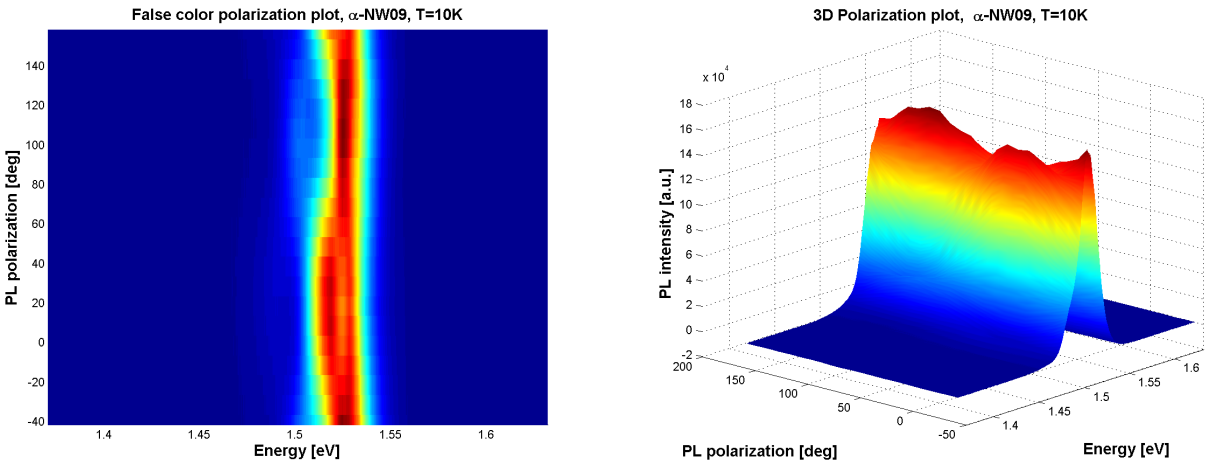

(a) Viewed from above.

(b) Viewed from the side.

Figure 4.20: False color plots of the polarization- and energy dependence of emission intensity for α-NW09, done at $10K$.

Figures 4.21a and 4.21b shows sin^2 fits of the emission at $1.508eV$ and $1.520eV$, respectively. Since the peaks are emitting at very close energies, the curve fitting method has difficulties resolving the peaks, which can be seen from the somewhat bad fit to the sin^2 function. Table 4.8 shows the numerical results from the fitting procedure. The sin^2 fit of the total emission was not included, because of the large difference in emission polarization from the two peaks.

The lower energy peak is closer to parallel- than perpendicular polarization, but is not perfectly parallel. The $1.520eV$ peak is polarized at 121.4°, which is closer to perpendicular- than parallel polarization. This might be an indication of emission from a WZ GaAs segment, and not ZB. Polarization data for the $\sim 1.515eV$ peak of other NWs from sample α is included in Appendix D.

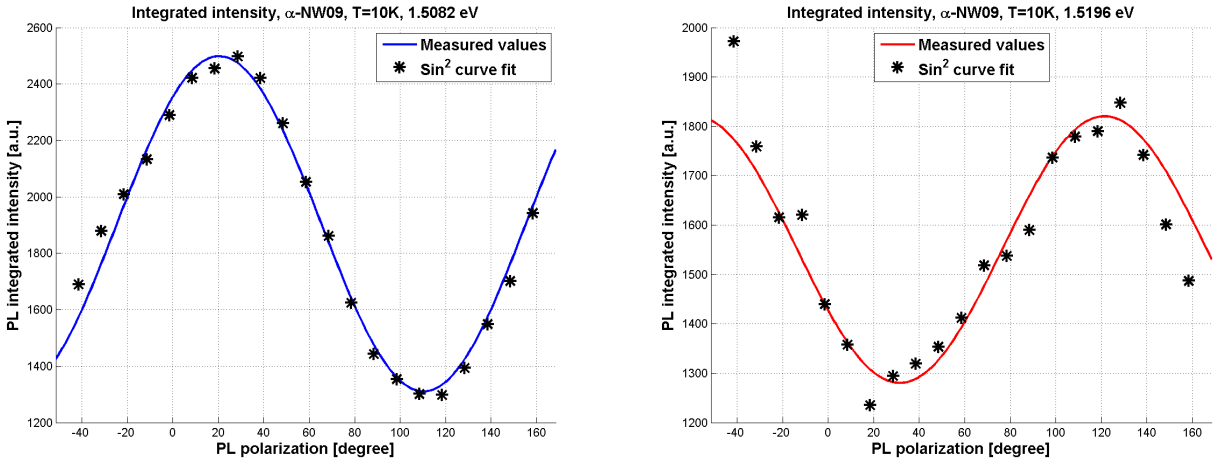

(a) α-NW09, 1.508eV peak.

(b) α-NW09, 1.520eV peak.

Figure 4.21: sin^2 fits of the PL emission intensity for α-NW09 at 10K. The figures are for peaks at different energies.

α-NW09	Peak energy [eV]	Angle to NW [deg]
	1.508	20.4°
	1.520	121.4°

Table 4.8: Polarization data for α-NW09 at 10K, resulting from curve fitting of peaks to a sin^2 function (Fig. 4.21).

4.4 Time-resolved photoluminescence

The time-resolved photoluminescence (TRPL) measurements were done by exciting the samples with short laser pulses. See section 3.2.5 for experimental setup, and section 3.3.4 for experimental method. TRPL measurements yield information on the electron-hole pair lifetime, and thus the transition rate of the electron-hole pairs. The transition rate can give an indication of the type of transitions that occurs in the NWs, giving insight into the number of defects present. TRPL measurements were conducted on samples δ and ψ, and are presented in this section.

The result was a three dimensional data set consisting of emission energy, time and emission intensity. This yielded plots as seen in figure 4.22a. From this, an interval of emission energy is chosen, and the emission intensity in that region summarized according to equation 3.13, restated here:

$$I(t) = \sum_{\lambda_{lower}}^{\lambda_{upper}} I_\lambda(t).$$

This gives a two dimensional data set resolved for emission intensity and time. Fitting this data to two exponential decay functions results in a plot like that seen in figure 4.22b. The fit parameters contain two decay lifetimes.

Notice that all peaks in the false color plots presented in this section are cut off at the same energy. This is because a filter was used to prevent laser light from reaching the streak camera. The filter is designed to cut a laser line at $808nm$, and effectively only signals above $815nm$ (energy below $1.523eV$) are transmitted through. Also, the streak tube sensitivity decreases with one order of magnitude between $1.552eV$ and $1.380eV$, making emission peaks at lower energies difficult to observe.

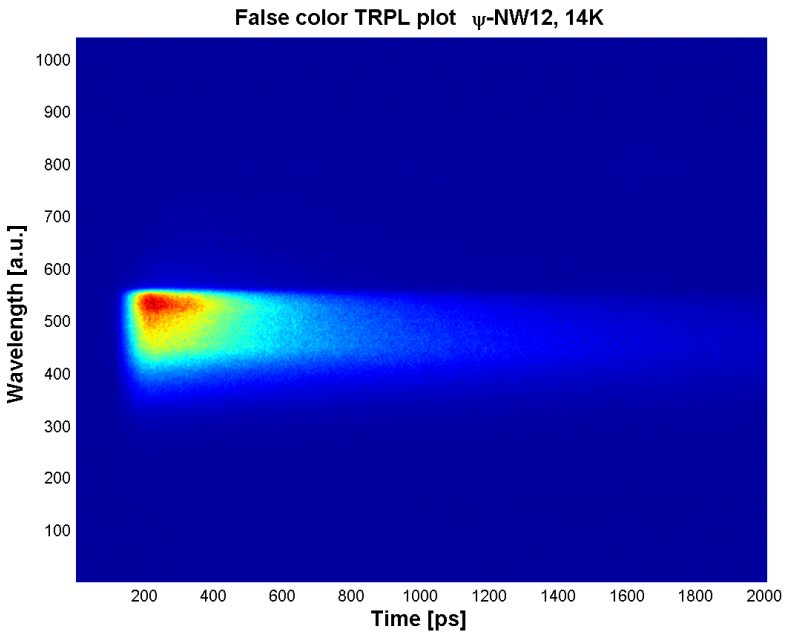

(a) False color plot of data output.

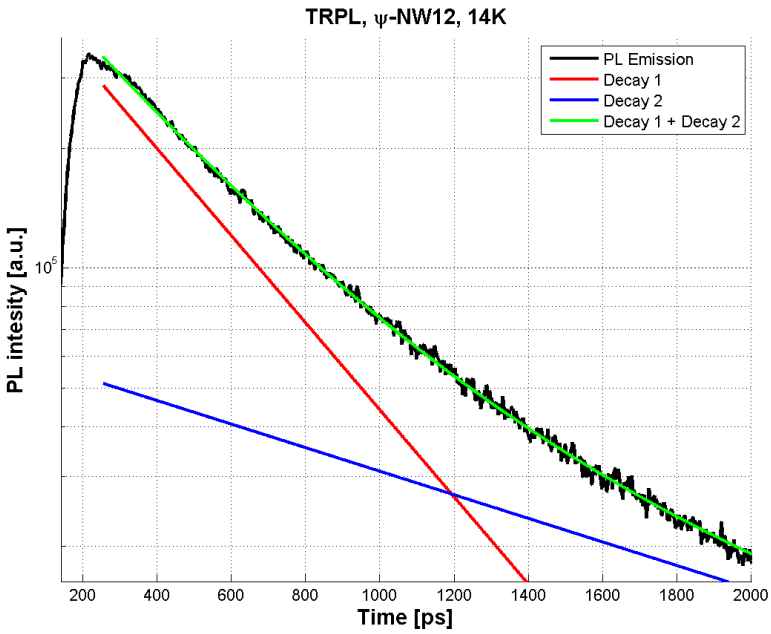

(b) Signal decay over time.

Figure 4.22: Data analysis of TRPL measurement on ψ-NW12, at $14K$.

4.4.1 Sample δ

The false color TRPL plot from δ-NW14 is presented in figure 4.23. As can be seen from the plot, at least two peaks are resolved, one at energy $\sim 1.47 - 1.49eV$, and one at $\sim 1.50 - 1.53eV$. The higher energy emission is broad, and can be compromised of several transitions. The lower peak seems to have a longer lifetime than the high energy peak(s). The result from curve fitting the data to two exponential functions, is shown in figure 4.24, with the numerical results in table 4.9.

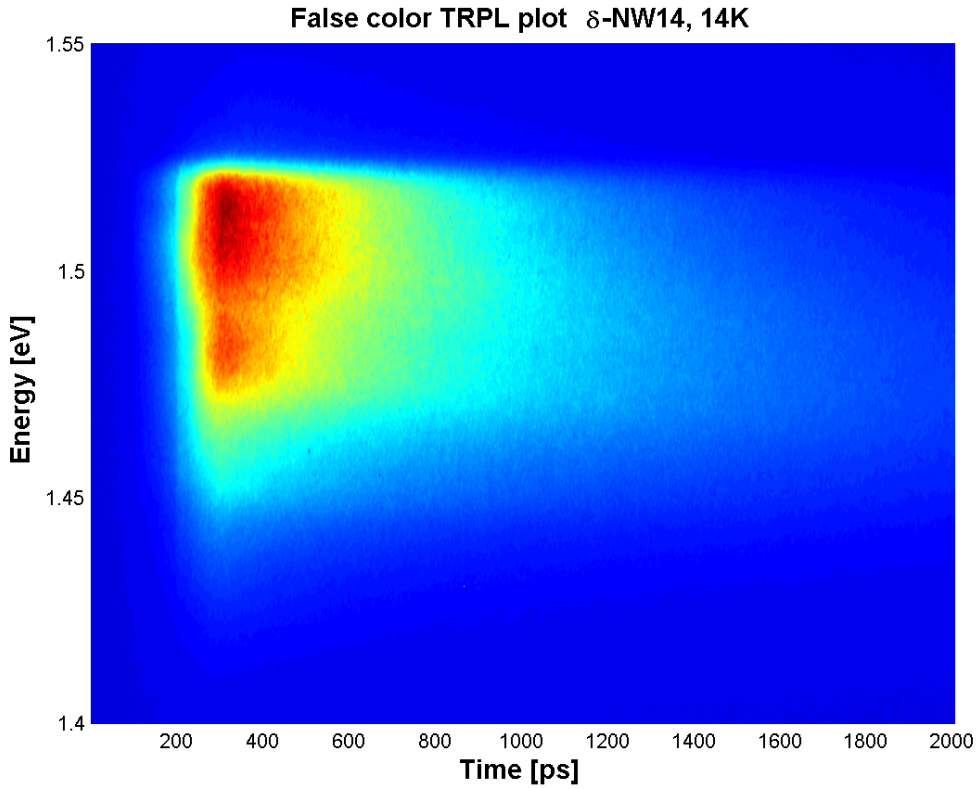

Figure 4.23: False color TRPL plot showing the emission intensity of δ-NW14 as a function of energy and time. The measurement is done at $14K$, with $765nm$ excitation light at $5mW$ LP. The laser pulses had a FWHM of $240fs$.

The low energy fit had one decay functions that decays at $300ps$ and one at $881ps$. From the figure, the slower decay is dominating over the fast decay. The

δ-NW14	Fit energy $[eV]$	Lifetime, decay 1 $[ps]$	Lifetime, decay 2 $[ps]$
	$1.474 - 1.496$	300	881
	$1.497 - 1.530$	560	$-$
	$1.473 - 1.528$	537	999

Table 4.9: Carrier lifetimes for δ-NW14, from data plotted in figures 4.24a-4.24c ("decay 1"; red curves, "decay 2"; blue curves). Obtained from curve fitting the signal to exponential decay functions.

high energy peak had a perfectly exponential decay, meaning that only one decay function was sufficient for fitting the signal. This peak had a lifetime of $560ps$. The total signal fit confirms the two other fits. The two decay functions for the total signal is similar in both brightness and lifetime to the other two.

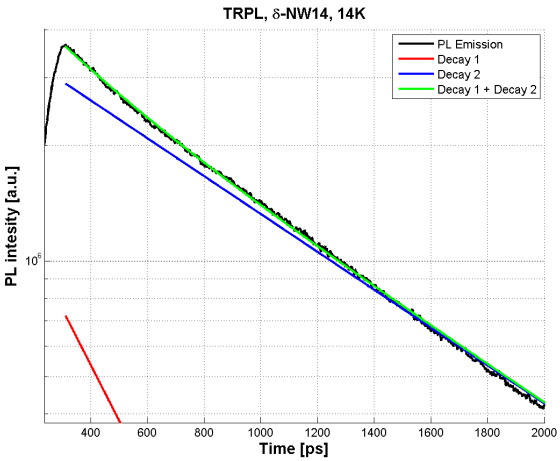

(a) Low energy peak fit, $1.474 - 1.496eV$.

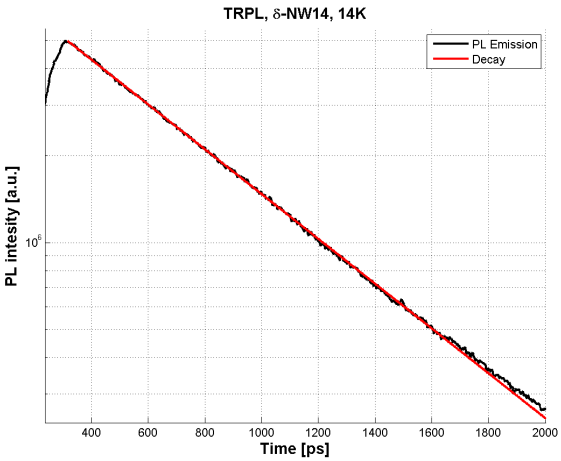

(b) High energy peak fit, $1.497 - 1.530eV$.

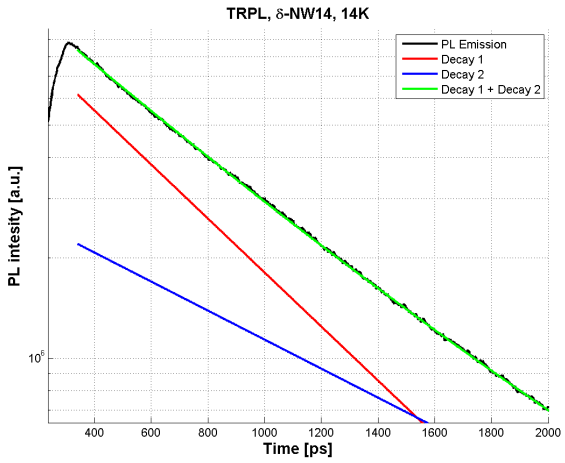

(c) Total signal fit, $1.473 - 1.528eV$.

Figure 4.24: TRPL signal decay plots for δ-NW14, taken by curve fitting the signal in figure 4.23 to exponential functions. See table 4.9 for numerical results.

4.4.2 Sample ψ

Figure 4.25 shows the TRPL data collected for ψ-NW01. Several peaks are visible from this plot, one strong at energy $1.505 - 1.515eV$, one medium peak at $1.48 - 1.50eV$, and at least one weaker peak at $1.46 - 1.475eV$. The medium peak seems to have the longest lifetime, but they are all in the same order of magnitude. The low sensitivity of the streak tube below $\sim 1.45eV$, could mean losing data for energies below this level. However, by looking at the PL data in figure 4.2, no strong emission is seen at energies below $\sim 1.46eV$.

Figures 4.26a-4.26d shows the exponential decay curves, while table 4.10 shows the lifetimes obtained.

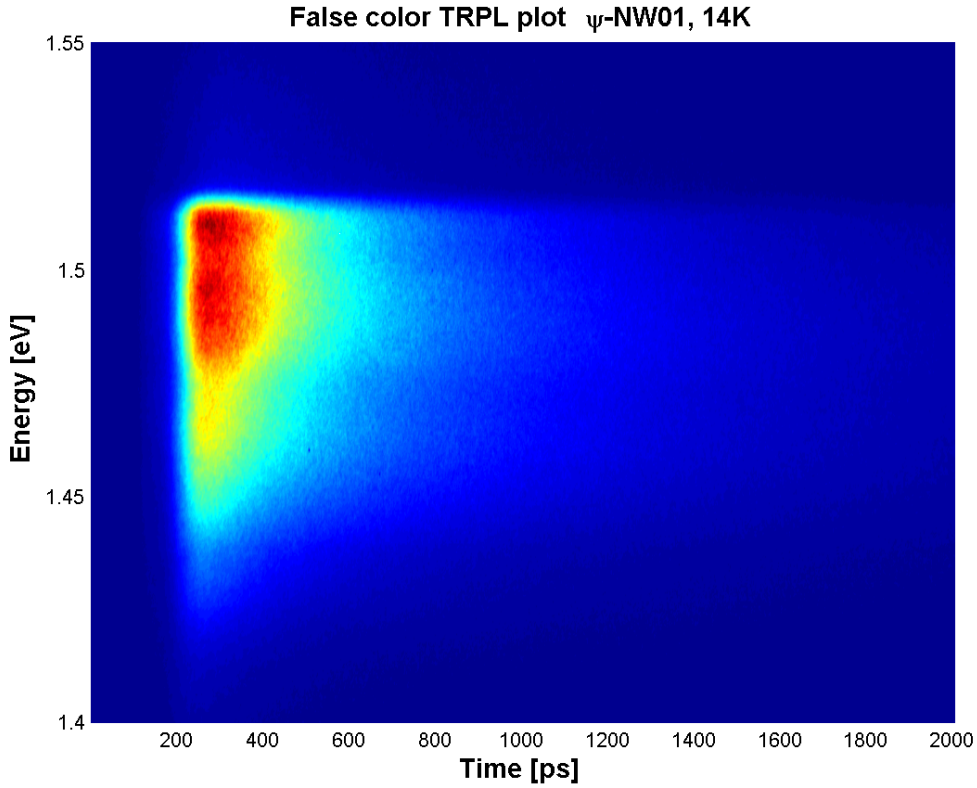

Figure 4.25: False color TRPL plot showing the emission intensity of ψ-NW01 as a function of energy and time. The measurement is done at $14K$, with $770nm$ excitation light at $5mW$ laser power. The laser pulses had a FWHM of $240fs$.

ψ-NW01	Fit energy $[eV]$	Lifetime, decay 1 $[ps]$	Lifetime, decay 2 $[ps]$
	$1.462 - 1.475$	720	198
	$1.483 - 1.505$	194	633
	$1.505 - 1.517$	546	184
	$1.459 - 1.518$	648	193

Table 4.10: Carrier lifetimes for ψ-NW01, from data plotted in figures 4.26a-4.26d ("decay 1"; red curves, "decay 2"; blue curves). Obtained from curve fitting the signal to exponential decay functions.

The four fits all show similar results. Two decay functions are needed, both starting at similar intensities. One of the signals decays fast, at $\sim 190ps$, while the other decays slower, at $\sim 550 - 720ps$.

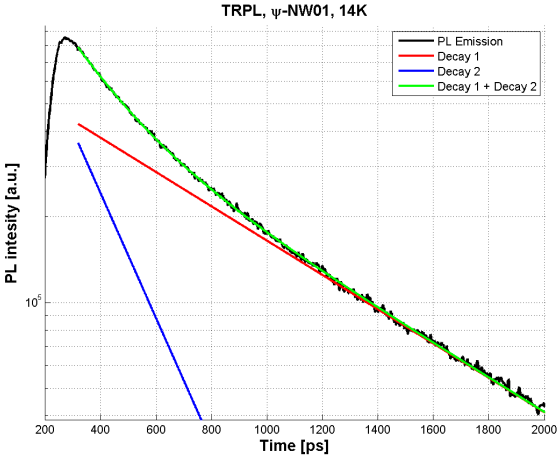

(a) Low energy peak fit, $1.462 - 1.475eV$.

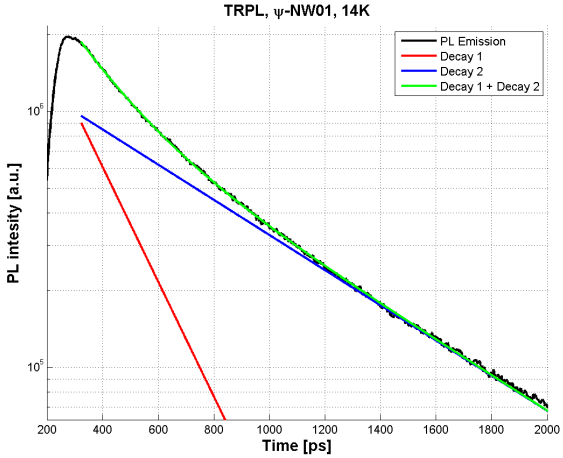

(b) Medium energy peak fit, $1.483 - 1.505eV$.

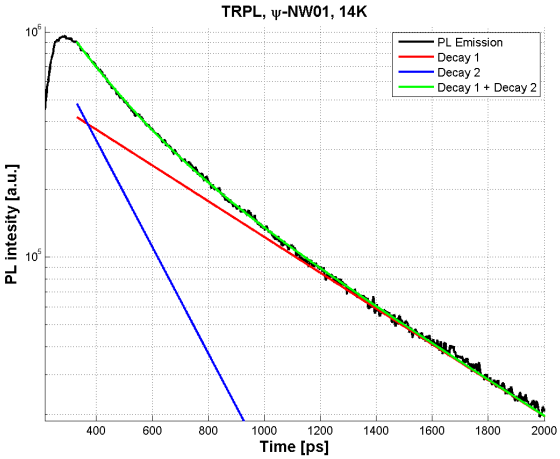

(c) High energy peak fit, $1.505 - 1.517eV$.

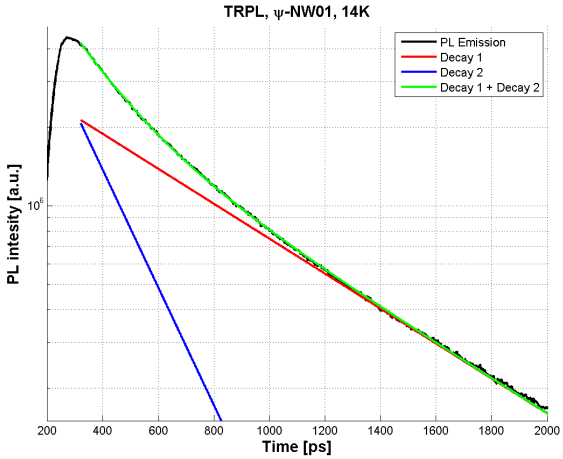

(d) Total signal fit, $1.459 - 1.518eV$.

Figure 4.26: TRPL signal decay plots for ψ-NW01, taken by curve fitting the signal in figure 4.25 to exponential functions. See table 4.10 for numerical results.

5 Discussion

The NWs studied in this work are all SC GaAs/AlGaAs core-shell NWs grown by the MBE VLS method. The growth process yields long, pure segments of ZB GaAs. During the growth termination process the Ga catalyst droplet was consumed. This step can give WZ segments and many ZB-WZ stacking faults, affecting optical properties. The GaAs core was then covered in a AlGaAs shell and a GaAs cap grown over that. See section 2.1 for information on the growth process, and section 3.1 for specific growth parameters used.

Temperature-, laser excitation power-, polarization dependent- as well as time-resolved PL measurements have been done on the three main samples of SC GaAs/AlGaAs core-shell NWs, and one reference sample. The main difference between the three samples was the V/III ratio that was used during growth (Tab. 3.1), and this will be the focus of the discussion.

The hypothesis is that a higher V/III ratio is beneficial for the purity of the NWs, thus improving the optical properties. Since the growth is catalyzed by a Ga droplet, more As is needed to make the GaAs material stoichiometric. A higher V/III ratio is expected to yield fewer Ga antisite defects in the core region. Ga antisite defects in the NW can affect the energy of emission and/or introduce non-radiative transitions, which are detrimental to emitting devices.

The results are presented in section 4. In this section, the results from each sample will first be analyzed separately, before a synthesis and comparison at the end. References will be made to the appendices where necessary in order to enforce conclusions.

5.1 Sample δ

Sample δ was represented by δ-NW14, while results from other NWs can be found in the appendix. This sample had the lowest V/III ratio of the three, 17.4. If the hypothesis is correct, these NWs should show the weakest emission from the core region, and is least likely to have free exciton transitions.

From figure 4.1, it is evident that this sample shows little to no emission at the

ZB GaAs free exciton energy, of $1.515eV$, the main peak emitting at $1.477eV$ for $10\mu W$ LP . At very high laser power ($LP \geq 30\mu W$), some emission can be seen at this energy, this might also be due to broadening of the peak at higher excitation. The temperature dependence of the emission energy, seen in figure 4.8, also shows that the NW emits at energies far below that of pure ZB. This is likely to be predominantly type-II recombination, meaning the sample has a high number of ZB-WZ stacking faults and/or other defects.

Comparison of the emission intensity at $14K$ and $290K$ (Fig. 4.12a), showed a relatively small decrease in intensity as compared to the other samples (Tab. 4.4). Since the sample is likely to have many defects, emission at low temperature might be suppressed, whereas emission at room temperature is not. This can contribute to the low ratio.

The polarization data, found in figure 4.15 and table 4.5, show neither parallel nor perpendicular polarization dependence, a sign of defect-related peaks. It is also noticed from figure 4.14 that the emission has very little polarization dependence. This is also seen for other NWs from sample δ, in Appendix B. If emission comes from the defect-rich tip of the NW, the dielectric effect can be weaker than in the core regions. In the core, the length is much larger than the diameter, causing strong parallel polarization from dielectric mismatch. For short emitting regions in the tip, however, this might not be the case, causing less polarization dependence for this sample.

The TRPL measurements give several peaks were emitting over a wide range of energies (Fig. 4.23). At lower energy, $1.474 - 1.496eV$, two lifetimes are observed, at $300ps$ and $881ps$. At energy $1.497 - 1.530eV$, one lifetime of $560ps$ is observed. Free excitons from SC NWs have life times of $1ns$ or more [51]. The emission measured here, is likely defect related, since no excitonic peaks are seen (Fig. 4.1). Defect related transition lifetimes are often longer than those of free excitons, whereas these are shorter. This data therefore means that there is strong non-radiative recombination in the samples, most likely due to poor quality of the core material.

All the data indicates that sample δ contains many defects and has little to no

emission from the core of the NWs. Since no excitonic transitions are observed, the sample shows poor promise for optoelectronic applications.

5.2 Sample ψ

Sample ψ, represented by ψ-NW01, had a V/III ratio of 23.8, the middle value of the samples. It is therefore expected to have somewhat better optical properties than sample δ.

The PL emission from ψ-NW01 can be seen in figure 4.2. The peak is not as broad as δ-NW14, but the main emission at $1.481eV$ is still far below that of pure ZB GaAs. The temperature dependence (Fig. 4.9) is an indication of type-II transitions, and a high number of defects. The data presented in table 4.4 and figure 4.12b, showing the decrease in emission intensity at $14K$ and $290K$, also show similar results as δ, where defects may contribute to the low value.

The PRPL measurements, however, show close to parallel polarized emission for peaks emitting at $1.486eV$ and $1.501eV$. This is seen in figure 4.17 and table 4.17. Since this is far below the free exciton energy, this is most likely also defect related emission, that coincidentally is parallel polarized.

The time-resolved experiments show at least three peaks emitting at different energies (Fig 4.23). For the low energy peak, emitting at $1.462 - 1.475eV$, the lifetimes are $198ps$ and $720ps$. The medium peak, $1.483 - 1.505eV$ has lifetimes $194ps$ and $633ps$. The high energy peak, $1.505 - 1.517eV$, has lifetimes $193ps$ and $648ps$. It is clear that the faster decay is approximately the same for the three peaks. The higher lifetime, however, decreases as energy increases. As for sample δ, the measurements on this sample indicates defect related emission. The lifetimes measured are below that expected from defect transitions, meaning non-radiative transitions and impurities in the core.

It should be noted that of the fourteen NWs analyzed in this sample, one NW did show what could be excitonic emission. This was ψ-NW12, and data from this NW is presented in Appendix A. The PL spectra in figure A.1a shows emission close to the $1.515eV$ energy, and the temperature dependence of this peak is relatively close to that of bulk ZB (Fig.A.1b). Because this NW was not

representative for sample ψ, it was not presented in this report.

The data shows that sample ψ has similar properties as sample δ, with one exception out of fourteen NWs. For the thirteen remaining NWs; no excitonic emission and indications of many defects and non-radiative transitions, means the sample has unsuitable optical properties.

5.3 Sample σ

σ-NW16 was used to represent NWs from sample σ. The sample had a V/III ratio of 30.1, higher than the other samples. It is therefore expected to be the sample of highest purity and likelihood of showing $\sim 1.515eV$ emission from the core region.

σ-NW16 emitted from three peaks at low temperature, one at $1.500eV$ and one at $1.517eV$ ($5\mu W$ LP), as seen in figure 4.3. Another peak is resolvable at $1.470eV$ for $1\mu W$ LP. Since the low energy $1.470eV$ emission does not grow in intensity for higher excitation power, the number of states emitting at this energy becomes saturated. These states likely come from type-II transitions and/or other defects. The emission near the free exciton emission energy of $1.515eV$ means it can be possible to detect free excitons in this NW.

The high energy peak was curve fitted to Gaussians for increasing laser power, and fitted to a near-linear function (Fig. 4.4). This fit shows a near linear dependence of emission intensity on laser power, in accordance with free exciton emission. The FWHM was found to be $16.3meV$ for this peak at $5\mu W$ LP (Tab. 4.2), an acceptable value for an excitonic peak.

The temperature dependence for the $1.500eV$ and $1.517eV$ peak is plotted in figure 4.10. The high energy emission follows close to that of the ZB GaAs reference curves, further indicating free exciton emission at low temperature. At temperatures $250K - 293K$, however, the energy is slightly larger, meaning that emission is then band-to-band.

Figure 4.12c and table 4.4 show the decrease in emission intensity between $16K$ and $293K$, which is three orders of magnitude. This ratio has to be improved, in order to optimize the material quality for device applications.

The polarization dependence in figure 4.18 clearly shows two transitions of

similar energy, as observed for other experiments on σ-NW16. The polarization dependence found from figure 4.19 is presented in table 4.7. The lower energy peak emits close to parallel polarization, 7.5°, and the higher energy peak emits at $-10°$ polarization, also close to parallel. The lower peak cannot be free exciton emission, since it emits at too low energy, but the higher peak is likely to be excitonic emission. See table C.1 for more polarization data from $\sim 1.515eV$ peaks of σ-NWs.

Sample σ shows the best promise of the three samples analyzed. All measurements indicate free exciton transitions, meaning this sample is the first to show emission that can be attributed to pure ZB GaAs from the core region of the NWs.

5.4 Sample α

Sample α was meant to be a reference sample in this work, since it was previously shown to emit close to the free exciton level. α-NW09 was used to represent NWs from this sample, which had a V/III ratio of 20.0, and a growth rate of $0.3ML/s$, while the other samples had $0.7ML/s$.

Figure 4.5 shows the emission spectrum of α-NW09 at $10K$. Two peaks are predominant, emitting at $1.506eV$ and $1.515eV$ at low temperature and $5\mu W$ LP. The high energy peak is fitted to a Gaussian and near-linear function to find the laser power dependence, as seen in figure 4.6. The fit yields a LP^2 dependence, indicating biexcitons. This might be affected by three measurement values at $LP \leq 1\mu W$, where the $1.515eV$ peak is almost negligible. The peak has a FWHM of $11.6meV$, making it narrower than the high energy peak of σ-NW16.

The temperature dependent plots in figure 4.11 shows that the $1.515eV$ emission follows close to bulk ZB GaAs at temperatures below $250K$, a further sign it might have free exciton emission. The $1.506eV$ transition is slightly below for all energies, meaning it can be affected by defects and stacking faults. The decrease in emission intensity between $10K$ and $293K$ (Fig. 4.12d and Tab. 4.4) is large, but about half of that for sample σ.

The PRPL measurement on sample α, seen in figure 4.20, confirm that there are two strong peaks emitting at similar energies. The sin^2 fits from figure 4.21

show that the peaks are almost perpendicularly polarized with respect to each other (Tab. 4.8). The higher energy transition, emitting at $1.519eV$, is polarized at 121.4°, which is closer to perpendicular than parallel. WZ GaAs is known to emit perpendicularly polarized light, meaning that this transition might come from a WZ segment in the NW. It is, however, $\sim 30°$ degrees away from perfectly perpendicular polarization, so this NW can have several defects as well. Table D.1 contains data from $\sim 1.515eV$ peaks of other α-NWs, with similar results.

Sample α does show good optical properties, and several signs of free exciton emission. The PRPL measurements, indicate that the excitonic emission can be coming from a large WZ segment in the tip of the NW.

5.5 Conclusions and future outlook

The measurements done indicate that samples δ and ψ have relatively similar optical properties. The peaks are both located at around $1.48eV$, and the temperature dependence is indicating type-II transitions. The polarization-resolved measurements show different properties, however, where δ has far from parallel polarized emission, whereas ψ shows almost parallel polarization. Due to the emission energy of the peaks of ψ, this cannot be free exciton emission. Therefore it is believed that the polarization of type-II emission may be depending on the specific configuration of defects in the NW, making it highly irregular between NWs from the same (or similar) samples. The TRPL data for these samples shows lifetimes lower than that of free excitons. For defect-related transitions this is not expected, and can be the result of bad AlGaAs shell properties or poor GaAs core quality. However, shell issues are unlikely, as the thickness and composition is as commonly reported for working NWs of this type [45] [111] [112], even with variations throughout the shell. The lifetimes are therefore attributed to core issues, and strong non-radiative transitions.

Sample σ was the only sample that exhibited free exciton emission, a strong indication of emission from the pure ZB region and relatively few defects and stacking faults in the core. The PL emission energy, the temperature dependence, the FWHM, the laser power dependence and the polarization-resolved measure-

ments all support this claim. NWs from sample σ show that a higher V/III ratio is beneficial to the optical properties of the NWs. The emission intensity decreases drastically from low- to room temperature, a property that requires improvement. Increasing the quality of the GaAs core and improving the structure in the tip region will be important in order to achieve this. One approach is to grow an axial AlGaAs insert before the solidification process of the Ga droplet is initiated. This will create a barrier between the defect-rich tip and the emitting core. Still more configurations to growth parameters are needed before sufficient quality is achieved for use in optoelectronic applications.

Sample α, which was used as a reference sample, also showed free exciton emission behavior around the $1.515eV$ energy, as was also found in another work [42]. The polarization-resolved measurements, which were not conduced earlier on α, show that light emitted at this energy is close to perpendicularly polarized, although shifted. This can mean that the emission comes from free excitons in WZ GaAs segments, possibly located in the tip. HR-TEM should be conducted to explore this.

In summary of the results, sample σ has superior properties to the other two samples, δ and ψ. Thus, the hypothesis that a higher V/III ratio is beneficial to the optical properties of NWs, is seemingly confirmed. Further analysis of σ is recommended, such as TRPL measurements and HR-TEM.

It should be noted, that even though α had a V/III ratio lower than that of ψ, it showed far superior properties. This can mean that the growth rate of $0.3ML/s$, used for α, is preferred to the growth rate of $0.7ML/s$, used for the other samples. It is proposed that more samples are grown at V/III ratios above that of σ, 30.1, and that and that the growth rate is decreased to $0.3ML/s$ for some of these samples. Approaches to passivate the tip, such as axial AlGaAs inserts, should also be explored.

5.6 Sources of error

Here follows a section about the sources of error that could arise from the experiments done.

The optical system is highly sensitive, it is thus necessary to optimize the setup by adjusting mirrors and other optical components at the start of every new experiment. This optimization can change the measured signals by more than one order of magnitude, making a comparison of the emission intensity from different samples futile.

There is some drift in the system, causing the focus of the laser beam to shift over time. This is most noticeable for measurements that take longer time, such as the polarization measurements. This was accounted for by having some overlap in the measurements, where the compensator angle, $C = 0°$ is equivalent to 90° and $C = 10°$ is equivalent to 100°. These measurements were compared, to ensure a minimal change in the signal. NWs with several emitting peaks are particularly sensitive to drift.

All components in the polarization setup (Fig. 3.3) can have an offset of up to ±2°. This value is below that of the resolution of these measurements, ±5°. The polarizer used in the PRPL measurements , was set at 90° to the optical table for all measurements. It was found that a value of 90° on the polarizer wheel, in fact caused the polarizer to be 55° to the optical table. This error was taken into account when analyzing the PRPL data.

The beam splitter cube (Fig 3.1), has polarization dependent transmission for wavelengths below $\sim 700nm$. This affects the excitation dependent measurements, where the polarized laser light reflected through the cube had wavelength $532nm$. The degree of polarization, as given by equation (2.34), was thus affected for polarization between 0° and 90°, and the direction of polarization can shift. At parallel and perpendicular polarization, the degree was not affected. At high excitation and negligible diameter-to-length, parallel absorption is stronger than perpendicular absorption by order of ~ 50, due to the dielectric effect [113]. This dominates over the change in polarization due to the beam splitter cube, and the approximate orientation of the NWs can be found. The use of this type of beam splitter was necessary, as other alternatives show lower transmission of the signal. This would require longer exposure, increasing drift and lowering the signal-to-noise ratio. Note that emission polarization measurements are unaffected. The

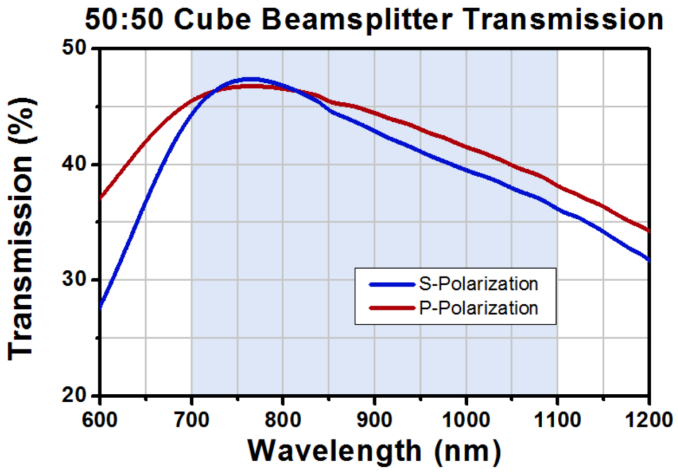

Figure 5.1: The transmission spectrum of Thorlabs BS017 beam splitter cube, for S-polarization and P-polarization [94].

polarized light transmitted through the cube is emitted from the sample, and has wavelength $\sim 820nm$.

References

[1] M.A. Green. *Solar cells: Operating Principles, Technology, and System Applications*. Prentice Hall, 1982.

[2] J.S.E. Lilienfeld. Method and apparatus for controlling electric currents, 1930. US Patent 1,745,175.

[3] M.G. Voronkov. Silicon era. *Russian Journal of Applied Chemistry*, 80:2190–2196, 2007.

[4] M. Quirk and J. Serda. *Semiconductor Manufacturing Technology*. Prentice Hall, 2001.

[5] M.R. Brozel and GE Stillman. *Properties of gallium arsenide*. INSPEC, London, 1996.

[6] Injo Ok, Hyoung-Sub Kim, Manhong Zhang, Chang-Yong Kang, Se Jong Rhee, Changhwan Choi, S.A. Krishnan, Tackhwi Lee, Feng Zhu, G. Thareja, and J.C. Lee. Metal gate-HfO2 MOS structures on GaAs substrate with and without Si interlayer. *IEEE, Electron Device Letters*, 27(3):145–147, 2006.

[7] M. Berroth and R. Bosch. High-frequency equivalent circuit of GaAs FETs for large-signal applications. *IEEE, Transactions on Microwave Theory and Techniques*, 39(2):224–229, 1991.

[8] Sadao Adachi. GaAs, AlAs, and Al(x)Ga(1-x)As material parameters for use in research and device applications. *Journal of Applied Physics*, 58(3):R1–R29, 1985.

[9] Josef A. Czaban, David A. Thompson, and Ray R. LaPierre. GaAs core-shell nanowires for photovoltaic applications. *Nano Letters*, 9(1):148–154, 2009.

[10] R.D. Dupuis. AlGaAs-GaAs lasers grown by metalorganic chemical vapor deposition — A review. *Journal of Crystal Growth*, 55(1):213–222, 1981.

[11] J.M. Woodall and H.J. Hovel. High-efficiency Ga(1-x)Al(x)As-GaAs solar cells. *Applied Physics Letters*, 21(8):379–381, 1972.

[12] Makoto Konagai, Mitsunori Sugimoto, and Kiyoshi Takahashi. High efficiency GaAs thin film solar cells by peeled film technology. *Journal of Crystal Growth*, 45(0):277–280, 1978.

[13] SF Fang, K. Adomi, S. Iyer, H. Morkoc, H. Zabel, C. Choi, and N. Otsuka. Gallium arsenide and other compound semiconductors on silicon. *Journal of Applied Physics*, 68(7):R31–R58, 1990.

[14] Gabor L. Hornyak, John J. Moore, H.F. Tibbals, and Joydeep Dutta. *Fundamentals of Nanotechnology*. Taylor & Francis Group, 2009.

[15] G. Cao. *Nanostructures & nanomaterials: synthesis, properties & applications*. World Scientific Publishing Company, 2004.

[16] Peidong Yang, Ruoxue Yan, and Melissa Fardy. Semiconductor nanowire: What's next? *Nano Letters*, 10(5):1529–1536, 2010.

[17] Yi Cui, Xiangfeng Duan, Jiangtao Hu, and Charles M. Lieber. Doping and electrical transport in silicon nanowires. *The Journal of Physical Chemistry B*, 104(22):5213–5216, 2000.

[18] Erik Garnett and Peidong Yang. Light trapping in silicon nanowire solar cells. *Nano Letters*, 10(3):1082–1087, 2010.

[19] Xiangfeng Duan, Yu Huang, Ritesh Agarwal, and Charles M. Lieber. Single-nanowire electrically driven lasers. *Nature*, 421:241–245, 2003.

[20] Karen L Kavanagh. Misfit dislocations in nanowire heterostructures. *Semiconductor Science and Technology*, 25(2):024006, 2010.

[21] D.L. Dheeraj, H.L. Zhou, A.F. Moses, T.B. Hoang, A.T.J. van Helvoort, B.O. Fimland, and H. Weman. Heterostructured III-V nanowires with mixed crystal phases grown by Au-assisted molecular beam epitaxy. *Nanowires*, 2010-02-01.

[22] D.L. Mathine. The integration of III-V optoelectronics with silicon circuitry. *IEEE, Journal of Selected Topics in Quantum Electronics*, 3(3):952 –959, 1997.

[23] R. S. Wagner and W. C. Ellis. Vapor-liquid-solid mechanism of single crystal growth. *Applied Physics Letters*, 4(5):89–90, 1964.

[24] Y. Xia, P. Yang, Y. Sun, Y. Wu, B. Mayers, B. Gates, Y. Yin, F. Kim, and H. Yan. One-dimensional nanostructures: Synthesis, characterization, and applications. *Advanced Materials*, 15(5):353–389, 2003.

[25] V. G. Dubrovskii, G. E. Cirlin, I. P. Soshnikov, A. A. Tonkikh, N. V. Sibirev, Yu. B. Samsonenko, and V. M. Ustinov. Diffusion-induced growth of GaAs nanowhiskers during molecular beam epitaxy: Theory and experiment. *Phys. Rev. B*, 71:205325, 2005.

[26] Z. H. Wu, X. Y. Mei, D. Kim, M. Blumin, and H. E. Ruda. Growth of Au-catalyzed ordered GaAs nanowire arrays by molecular-beam epitaxy. *Applied Physics Letters*, 81(27):5177–5179, 2002.

[27] Z. Zanolli, F. Fuchs, J. Furthmüller, U. von Barth, and F. Bechstedt. Model GW band structure of InAs and GaAs in the wurtzite phase. *Phys. Rev. B*, 75:245121, 2007.

[28] Dasa L. Dheeraj, Gilles Patriarche, Hailong Zhou, Thang B. Hoang, Anthonysamy F. Moses, Sondre Grønsberg, Antonius T. J. van Helvoort, Bjørn-Ove Fimland, and Helge Weman. Growth and characterization of wurtzite GaAs nanowires with defect-free zinc blende GaAsSb inserts. *Nano Letters*, 8(12):4459–4463, 2008.

[29] Kenji Hiruma, Masamitsu Yazawa, Keiichi Haraguchi, Kensuke Ogawa, Toshio Katsuyama, Masanari Koguchi, and Hiroshi Kakibayashi. GaAs free-standing quantum-size wires. *Journal of Applied Physics*, 74(5):3162–3171, 1993.

[30] A. De and Craig E. Pryor. Predicted band structures of III-V semiconductors in the wurtzite phase. *Phys. Rev. B*, 81:155210, 2010.

[31] Hannah J. Joyce, Jennifer Wong-Leung, Qiang Gao, H. Hoe Tan, and Chennupati Jagadish. Phase perfection in zinc blende and wurtzite III-V nanowires using basic growth parameters. *Nano Letters*, 10(3):908–915, 2010.

[32] Hannah J. Joyce, Qiang Gao, H. Hoe Tan, Chennupati Jagadish, Yong Kim, Melodie A. Fickenscher, Saranga Perera, Thang Ba Hoang, Leigh M. Smith, Howard E. Jackson, Jan M. Yarrison-Rice, Xin Zhang, and Jin Zou. Unexpected benefits of rapid growth rate for III-V nanowires. *Nano Letters*, 9(2):695–701, 2009.

[33] A. Fontcuberta i Morral, C. Colombo, G. Abstreiter, J. Arbiol, and J. R. Morante. Nucleation mechanism of gallium-assisted molecular beam epitaxy growth of gallium arsenide nanowires. *Applied Physics Letters*, 92(6):063112, 2008.

[34] C. Colombo, D. Spirkoska, M. Frimmer, G. Abstreiter, and A.F. i Morral. Ga-assisted catalyst-free growth mechanism of GaAs nanowires by molecular beam epitaxy. *Physical Review B*, 77(15):155326, 2008.

[35] Fauzia Jabeen, Vincenzo Grillo, Silvia Rubini, and Faustino Martelli. Self-catalyzed growth of GaAs nanowires on cleaved Si by molecular beam epitaxy. *Nanotechnology*, 19(27):275711, 2008.

[36] Peter Krogstrup, Ronit Popovitz-Biro, Erik Johnson, Morten Hannibal Madsen, Jesper Nygård, and Hadas Shtrikman. Structural phase control in self-catalyzed growth of GaAs nanowires on silicon (111). *Nano Letters*, 10(11):4475–4482, 2010.

[37] D. Spirkoska, J. Arbiol, A. Gustafsson, S. Conesa-Boj, F. Glas, I. Zardo, M. Heigoldt, M. H. Gass, A. L. Bleloch, S. Estrade, M. Kaniber, J. Rossler,

F. Peiro, J. R. Morante, G. Abstreiter, L. Samuelson, and A. Fontcuberta i Morral. Structural and optical properties of high quality zinc-blende/wurtzite GaAs nanowire heterostructures. *Phys. Rev. B*, 80:245325, 2009.

[38] U. Gösele, F. Morehead, W. Frank, and A. Seeger. Diffusion of gold in silicon: A new model. *Applied Physics Letters*, 38(3):157–159, 1981.

[39] W.M. Bullis. Properties of gold in silicon. *Solid-State Electronics*, 9(2):143 – 168, 1966.

[40] S. Plissard, K. A. Dick, X. Wallart, and P. Caroff. Gold-free GaAs/GaAsSb heterostructure nanowires grown on silicon. *Applied Physics Letters*, 96(12):121901, 2010.

[41] S. Plissard, G. Larrieu, X. Wallart, and P. Caroff. High yield of self-catalyzed GaAs nanowire arrays grown on silicon via gallium droplet positioning. *Nanotechnology*, 22(27):275602, 2011.

[42] Stian Gulla, Helge Weman, and Lyubomir Ahtapodov. Optical properties of self-catalyzed GaAs/AlGaAs core-shell nanowires. *Norwegian University of Science and Technology, Department of Electronics and Telecommunications*, 2012.

[43] Narayana Dheeraj Dasa Lakshmi. Growth and structural characterization of III-V nanowires grown by molecular beam epitaxy. *Phd thesis, Norwegian University of Science and Technology, Department of Electronics and Telecommunications*, 2010.

[44] A. Ichimiya and P.I. Cohen. *Reflection High-Energy Electron Diffraction*. Cambridge University Press, 2004.

[45] Steffen Breuer, Carsten Pfüller, Timur Flissikowski, Oliver Brandt, Holger T. Grahn, Lutz Geelhaar, and Henning Riechert. Suitability of Au- and self-assisted GaAs nanowires for optoelectronic applications. *Nano Letters*, 11(3):1276–1279, 2011.

[46] T. Oka, K. Hirata, K. Ouchi, H. Uchiyama, T. Taniguchi, K. Mochizuki, and T. Nakamura. Advanced performance of small-scaled InGaP/GaAs HBT's with fT over 150 GHz and fmax over 250 GHz. In *Electron Devices Meeting, 1998. IEDM '98. Technical Digest., International*, pages 653 –656, 1998.

[47] James R. Chelikowsky and Marvin L. Cohen. Nonlocal pseudopotential calculations for the electronic structure of eleven diamond and zinc-blende semiconductors. *Phys. Rev. B*, 14:556–582, 1976.

[48] J.L. Freeouf, D. A. Buchanan, S.L. Wright, T.N. Jackson, J. Batey, B. Robinson, A. Callegari, A. Paccagnella, and J.M. Woodall. Studies of GaAs - oxide interfaces with and without Si interlayer. *Journal of Vacuum Science Technology B: Microelectronics and Nanometer Structures*, 8(4):860–866, 1990.

[49] B.G. Streetman and S.K. Banerjee. *Solid State Electronic Devices: International Edition*. Prentice Hall Series in Solid State Physical Electronics. Prentice Hall, 2009.

[50] Abdul Mazid Munshi, Dasa L. Dheeraj, Jelena Todorovic, Antonius T.J. van Helvoort, Helge Weman, and Bjørn-Ove Fimland. Crystal phase engineering in self-catalyzed GaAs and GaAs/GaAsSb nanowires grown on Si(111). *Journal of Crystal Growth*, 372(0):163–169, 2013.

[51] G.D. Gilliland. Photoluminescence spectroscopy of crystalline semiconductors. *Materials Science and Engineering: R: Reports*, 18(3–6):99 – 399, 1997.

[52] A.M Munshi et al. Unpublished.

[53] M.C. Plante and R.R. LaPierre. Au-assisted growth of GaAs nanowires by gas source molecular beam epitaxy: Tapering, sidewall faceting and crystal structure. *Journal of Crystal Growth*, 310(2):356–363, 2008.

[54] David J Fisher. *Diffusion in GaAs and other III-V semiconductors: 10 years of research*. Scitec Publ., 1998.

[55] C. Kittel. *Introduction to Solid State Physics*. John Wiley & Sons, 2004.

[56] P.C. Hemmer. *Faste Stoffers Fysikk*. Tapir Forlag, 1987.

[57] Wikipedia, the free encyclopedia. `http://en.wikipedia.org/wiki/Zincblende_(crystal_structure)` and `http://en.wikipedia.org/wiki/Wurtzite_(crystal_structure)`. Accessed: 01/07/2013.

[58] M. I. McMahon and R. J. Nelmes. Observation of a wurtzite form of Gallium Arsenide. *Phys. Rev. Lett.*, 95:215505, 2005.

[59] A. Mazid Munshi, Dasa L. Dheeraj, Vidar T. Fauske, Dong-Chul Kim, Antonius T. J. van Helvoort, Bjørn-Ove Fimland, and Helge Weman. Vertically aligned GaAs nanowires on graphite and few-layer graphene: Generic model and epitaxial growth. *Nano Letters*, 12(9):4570–4576, 2012.

[60] P. Caroff, K. A. Dick, J. Johansson, M. E. Messing, K Deppert, and L. Samuelson. Controlled polytypic and twin-plane superlattices in III-V nanowires. *Nature Nanotechnology*, 4:50–55, 2009.

[61] Lyubomir Ahtapodov, Jelena Todorovic, Phillip Olk, Terje Mjåland, Patrick Slåttnes, Dasa L. Dheeraj, Antonius T. J. van Helvoort, Bjørn-Ove Fimland, and Helge Weman. A story told by a single nanowire: Optical properties of wurtzite GaAs. *Nano Letters*, 12(12):6090–6095, 2012.

[62] K. Misra Prasanta. *Physics of Condensed Matter*. Academic Press, 2011.

[63] Thomas Elsaesser, Jagdeep Shah, Lucio Rota, and Paolo Lugli. Initial thermalization of photoexcited carriers in GaAs studied by femtosecond luminescence spectroscopy. *Phys. Rev. Lett.*, 66:1757–1760, 1991.

[64] Martin Heiss, Sonia Conesa-Boj, Jun Ren, Hsiang-Han Tseng, Adam Gali, Andreas Rudolph, Emanuele Uccelli, Francesca Peiró, Joan Ramon Morante, Dieter Schuh, Elisabeth Reiger, Efthimios Kaxiras, Jordi Arbiol, and Anna Fontcuberta i Morral. Direct correlation of crystal structure and optical properties in wurtzite/zinc-blende GaAs nanowire heterostructures. *Phys. Rev. B*, 83:045303, 2011.

[65] W Y Liang. Excitons. *Physics Education*, 5(4):226, 1970.

[66] J. Frenkel. On the transformation of light into heat in solids, I. *Phys. Rev.*, 37:17–44, 1931.

[67] Gregory H. Wannier. The structure of electronic excitation levels in insulating crystals. *Phys. Rev.*, 52:191–197, 1937.

[68] Gregory D. Scholes and Garry Rumbles. Excitons in nanoscale systems. *Nature Materials*, 5:683 –697, 2006.

[69] E. Hal Bogardus and H. Barry Bebb. Bound-exciton, free-exciton, band-acceptor, donor-acceptor, and Auger recombination in GaAs. *Phys. Rev.*, 176:993–1002, 1968.

[70] G. Vektaris. A new approach to the molecular biexciton theory. *The Journal of Chemical Physics*, 101(4):3031–3040, 1994.

[71] H. Y. Fan. Temperature dependence of the energy gap in semiconductors. *Phys. Rev.*, 82:900–905, 1951.

[72] Y.P. Varshni. Temperature dependence of the energy gap in semiconductors. *Physica*, 34(1):149 – 154, 1967.

[73] P. Debye. Zur Theorie der spezifischen Waerme. *Annalen der Physik (Leipzig)*, 39(4):789, 1912.

[74] T. K. Tran, W. Park, W. Tong, M. M. Kyi, B. K. Wagner, and C. J. Summers. Photoluminescence properties of ZnS epilayers. *Journal of Applied Physics*, 81(6):2803 –2809, 1997.

[75] P. Lautenschlager, M. Garriga, S. Logothetidis, and M. Cardona. Interband critical points of GaAs and their temperature dependence. *Phys. Rev. B*, 35:9174–9189, 1987.

[76] Léon Van Hove. The occurrence of singularities in the elastic frequency distribution of a crystal. *Phys. Rev.*, 89:1189–1193, 1953.

[77] Michael Mansfield and Colm O'Sullivan. *Understanding physics*. Wiley, 2012.

[78] Jing Liqiang, Qu Yichun, Wang Baiqi, Li Shudan, Jiang Baojiang, Yang Libin, Fu Wei, Fu Honggang, and Sun Jiazhong. Review of photoluminescence performance of nano-sized semiconductor materials and its relationships with photocatalytic activity. *Solar Energy Materials and Solar Cells*, 90(12):1773–1787, 2006.

[79] P. T. Landsberg. Non-radiative transitions in semiconductors. *Physica Status Solidi (b)*, 41(2):457–489, 1970.

[80] D. V. Lang and C. H. Henry. Nonradiative recombination at deep levels in GaAs and GaP by lattice-relaxation multiphonon emission. *Phys. Rev. Lett.*, 35:1525–1528, 1975.

[81] Albert Einstein. Zur Quantentheorie der Strahlung. *Physikalische Zeitschrift*, 18(1):121–128, 1917.

[82] Larry A. Coldren, Scott W. Corzine, and Milan L. Mashanovich. *Diode Lasers and Photonic Integrated Circuits*. John Wiley & Sons, 2012.

[83] H. M. Lai, P. T. Leung, and K. Young. Electromagnetic decay into a narrow resonance in an optical cavity. *Phys. Rev. A*, 37:1597–1606, 1988.

[84] E. M. Purcell, H. C. Torrey, and R. V. Pound. Resonance absorption by nuclear magnetic moments in a solid. *Phys. Rev.*, 69:37–38, 1946.

[85] Bernt Ketterer, Martin Heiss, Emanuele Uccelli, Jordi Arbiol, and Anna Fontcuberta i Morral. Untangling the electronic band structure of wurtzite GaAs nanowires by resonant raman spectroscopy. *ACS Nano*, 5(9):7585–7592, 2011.

[86] Franz Urbach. The long-wavelength edge of photographic sensitivity and of the electronic absorption of solids. *Phys. Rev.*, 92:1324–1324, 1953.

[87] Sajeev John, Costas Soukoulis, Morrel H. Cohen, and E. N. Economou. Theory of electron band tails and the Urbach optical-absorption edge. *Phys. Rev. Lett.*, 57:1777–1780, 1986.

[88] Microstructured Materials Group, E.O. Lawrence Berkeley National Laboratory. `http://energy.lbl.gov/ecs/aerogels/sa-optical.html`. Accessed: 01/07/2013.

[89] D. Chemla, D. Miller, P. Smith, A. Gossard, and W. Wiegmann. Room temperature excitonic nonlinear absorption and refraction in GaAs/AlGaAs multiple quantum well structures. *IEEE, Journal of Quantum Electronics*, 20(3):265 – 275, 1984.

[90] F. Binet, J. Y. Duboz, J. Off, and F. Scholz. High-excitation photoluminescence in GaN: Hot-carrier effects and the Mott transition. *Phys. Rev. B*, 60:4715–4722, 1999.

[91] B.E.A. Saleh and M.C. Teich. *Fundamentals of Photonics*. John Wiley & Sons, 2007.

[92] P.C. Hemmer. *Kvante Mekanikk*. Tapir Forlag, 2000.

[93] J. F. Ryan, R. A. Taylor, A. J. Turberfield, Angela Maciel, J. M. Worlock, A. C. Gossard, and W. Wiegmann. Time-resolved photoluminescence of two-dimensional hot carriers in GaAs-AlGaAs heterostructures. *Phys. Rev. Lett.*, 53:1841–1844, 1984.

[94] Thorlabs - Non-Polarizing Cube Beamsplitters, BS017. `http://www.thorlabs.de/NewGroupPage9.cfm?ObjectGroup_ID=6207`. Accessed: 01/07/2013.

[95] Thorlabs - Pellicle Beamsplitters, $400nm - 2.4\mu m$. `http://www.thorlabs.com/newgrouppage9.cfm?objectgroup_id=898`. Accessed: 01/07/2013.

[96] Janis Research. ST-500 Microscopy Cryostat. `http://www.janis.com/Micro-Raman_Applications_KeySupplier.aspx`. Accessed: 01/07/2013.

[97] Pfeiffer Vacuum Technology AG. HiCube 80 Eco. http://www.pfeiffer-vacuum.com/productPdfs/PMS03550.en.pdf. Accessed: 01/07/2013.

[98] Spectra-Physics. Milennia Pro s-series. http://www.newport.com/spforensic/A__Millennia_Pro_s_Datasheet.pdf. Accessed: 01/07/2013.

[99] Horiba. Jobin Yvon iHR550 Imaging Spectrometer. http://www.horiba.com/scientific/products/optical-spectroscopy/spectrometers-monochromators/ihr/ihr550-imaging-spectrometer-200/. Accessed: 01/07/2013.

[100] Andor Technology PLC. iDus InGaAs detector array for spectroscopy. http://www.andor.com/pdfs/specifications/Andor_iDus-InGaAs_1.7_Specifications.pdf. Accessed: 01/07/2013.

[101] National Instruments, LabVIEW. http://sine.ni.com/np/app/main/p/docid/nav-104/lang/no/. Accessed: 01/07/2013.

[102] Spectra-Physics. Tsunami Series Ti:Sapphire Ultrafast Oscillators. http://assets.newport.com/webDocuments-EN/images/Tsunami_Ultrafast_Laser_SP.pdf. Accessed: 01/07/2013.

[103] Princeton Instruments, Acton Series Monochromators and Spectrographs. http://www.princetoninstruments.com/Uploads/Princeton/Documents/Datasheets/Princeton_Instruments_Acton_Series_N2_4_10_13.pdf. Accessed: 01/07/2013.

[104] Optronics, Optoscope-SC, Streak Camera Family. http://www.optronis.de/fileadmin/Upload/Product/Streak/SC-Family.pdf. Accessed: 01/07/2013.

[105] Optronis, OptoAnalyse. http://www.optronis.de/fileadmin/Upload/Download/3991-SU-01-I_v3.50.pdf. Accessed: 01/07/2013.

[106] Thang Ba Hoang, Lyubov V. Titova, Jan M. Yarrison-Rice, Howard E. Jackson, Alexander O. Govorov, Yong Kim, Hannah J. Joyce, H. Hoe Tan, Chennupati Jagadish, and Leigh M. Smith. Resonant excitation and imaging of nonequilibrium exciton spins in single core-shell GaAs-AlGaAs nanowires. *Nano Letters*, 7(3):588–595, 2007.

[107] MathWorks Inc. `http://www.mathworks.se/products/matlab/index.html`. Accessed: 01/07/2013.

[108] John Aldrich. Doing least squares: Perspectives from Gauss and Yule. *International Statistical Review*, 66(1):61–81, 1998.

[109] Spectra-Physics. 3900S CW Tunable Ti:Sapphire Laser. `http://www.newport.com/3900S-CW-Tunable-Ti-Sapphire-Laser/368139/1033/info.aspx`. Accessed: 01/07/2013.

[110] Avantes. AvaSpec ULS3648. `http://www.avantes.com/Chemistry/AvaSpec-3648-Fiber-Optic-Spectrometer/Detailed-product-flyer.html`. Accessed: 01/07/2013.

[111] Ingrid Snustad and A.T.J. van Helvoort. Selective examination of optically and structurally separable parts within GaAs/AlGaAs core-shell nanowires by micro-photoluminescence and transmission electron microscopy. *Norwegian University of Science and Technology, Department of Electronics and Telecommunications*, 2013.

[112] J. Heinrich, A. Huggenberger, T. Heindel, S. Reitzenstein, S. Höfling, L. Worschech, and A. Forchel. Single photon emission from positioned GaAs/AlGaAs photonic nanowires. *Applied Physics Letters*, 96(21):211117, 2010.

[113] H. E. Ruda and A. Shik. Polarization-sensitive optical phenomena in semiconducting and metallic nanowires. *Phys. Rev. B*, 72:115308, 2005.

Appendices

A Sample ψ-NW12

ψ-NW12 was one in fourteen NWs from sample ψ that showed an emission peak near the exciton energy, $\sim 1.515eV$.

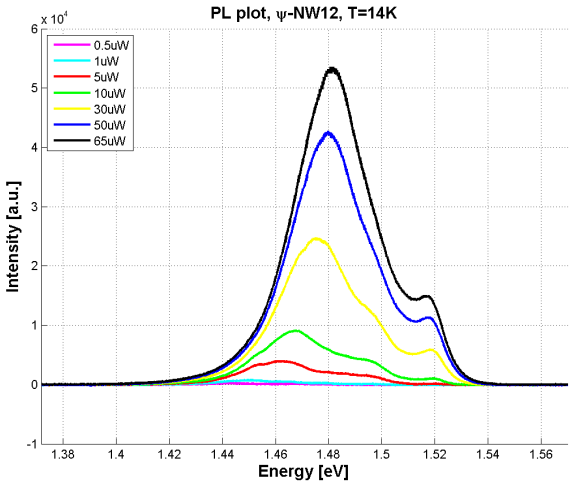

(a) PL emission spectrum and emission energy for ψ-NW12 at $14K$. High energy peak emitting at $1.518eV$.

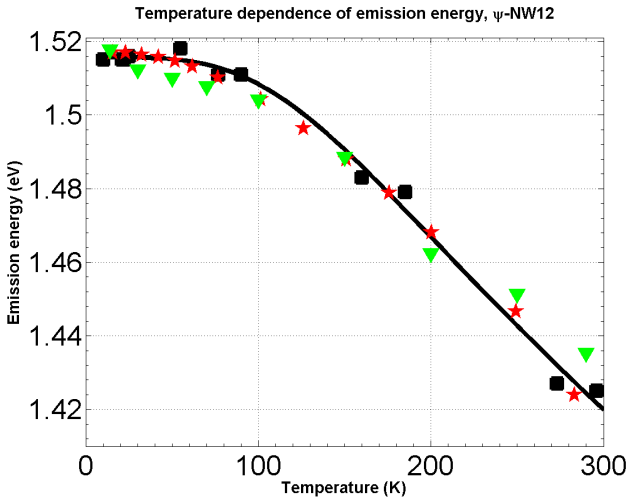

(b) Temperature dependence of emission energy for ψ-NW12. Also included in the plot is data for a **ZB GaAs epilayer** and a Varshni fitted curve for **bulk ZB GaAs**.

Figure A.1: PL spectrum and temperature dependence of ψ-NW12.

B Sample δ, Polarization

Polarization dependence of NWs from sample δ.

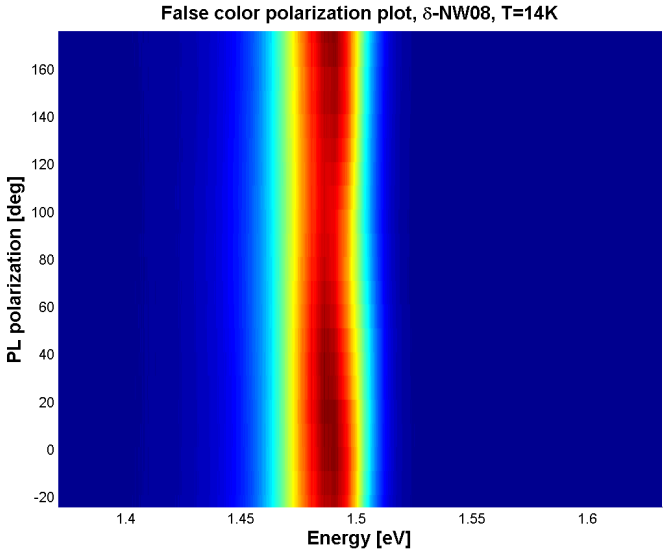

(a) δ-NW08

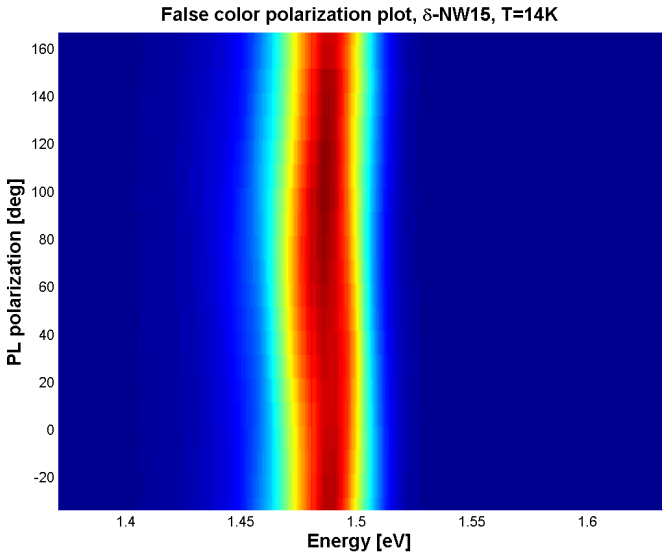

(b) δ-NW15

Figure B.1: False color polarization plots of NWs from sample δ, measured at $14K$.

C Sample σ, Polarization

Polarization dependence values of $\sim 1.515eV$ peaks obtained from sin^2 fits, for sample σ.

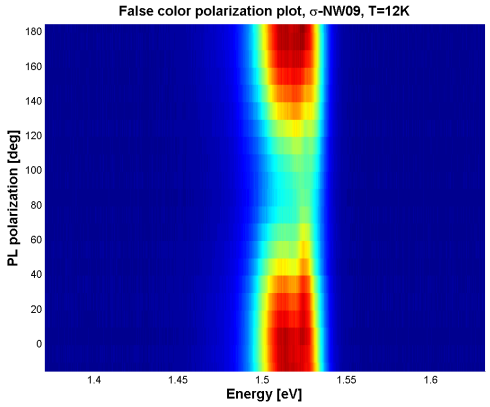

(a) False color plot.

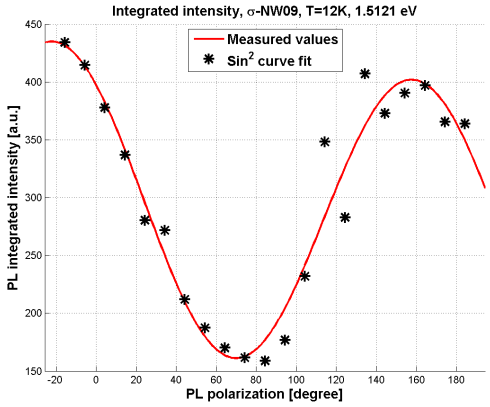

(b) sin^2 fit of $1.512eVpeak$.

Figure C.1: False color polarization plot and sin^2 fit of σ-NW09, obtained at $12K$.

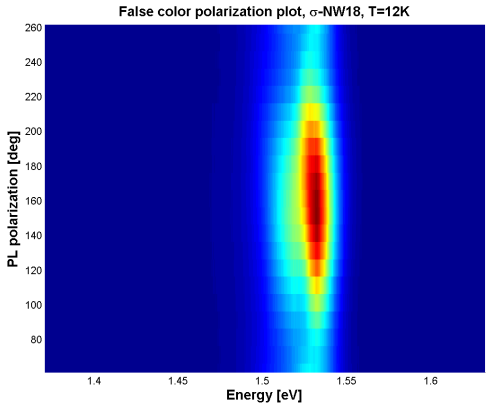

(a) False color plot.

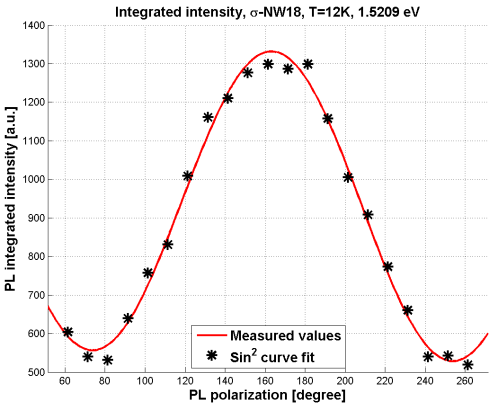

(b) sin^2 fit of $1.520eVpeak$.

Figure C.2: False color polarization plot and sin^2 fit of σ-NW18, obtained at $12K$.

	Peak energy $[eV]$	Angle to NW $[deg]$
σ-NW09	1.512	$-21.1°$
σ-NW18	1.520	$-16.6°$

Table C.1: Polarization data for σ-NW09 and σ-NW18 at $12K$, resulting from curve fitting of peaks to a sin^2 function. Plots C.1b and C.2b were used for curve fitting.

D Sample α, Polarization

Polarization dependence values of $\sim 1.515eV$ peaks obtained from sin^2 fits, for sample α.

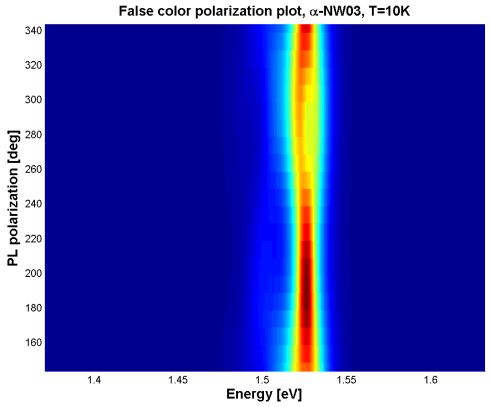

(a) False color plot.

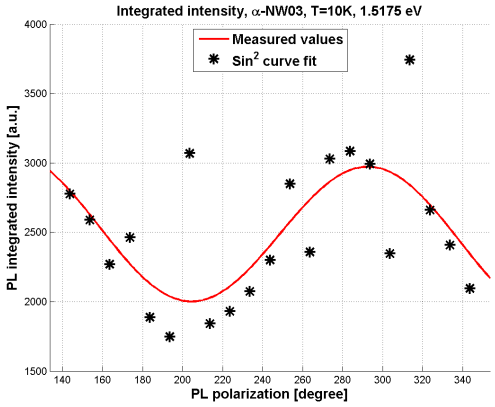

(b) sin^2 fit of $1.518eVpeak$.

Figure D.1: False color polarization plot and sin^2 fit of α-NW03, obtained at $10K$.

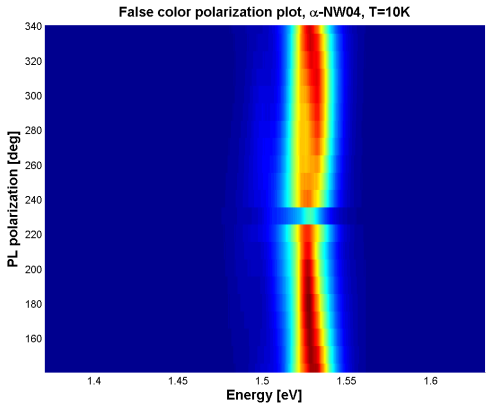

(a) False color plot.

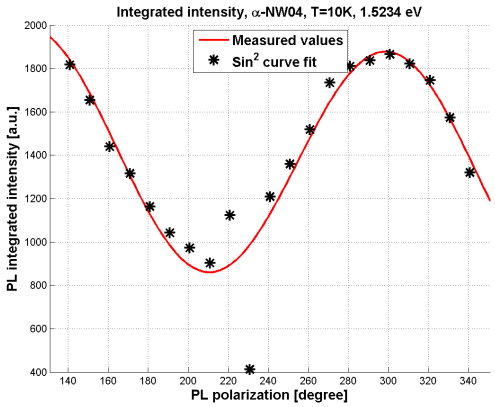

(b) sin^2 fit of $1.523eVpeak$.

Figure D.2: False color polarization plot and sin^2 fit of α-NW04, obtained at $10K$.

	Peak energy $[eV]$	Angle to NW $[deg]$
α-NW03	1.518	113.5°
α-NW04	1.523	119.6°

Table D.1: Polarization data for α-NW03 and α-NW04 at $10K$, resulting from curve fitting of peaks to a sin^2 function. Plots D.1b and D.2b were used for curve fitting.